Finite-element modelling of the response of the newborn middle ear to sound

Royan Jafari

Biological and Biomedical Engineering Program

McGill University, Montréal

2023 March

A thesis submitted to McGill University

in partial fulfillment of the requirements of the degree of

Master of Engineering

Acknowledgments

I would like to take this opportunity to send my gratitude to those without whose support this thesis would not have been possible.

First of all, I would like to offer my sincerest gratitude to my supervisor, Dr. W. Robert J. Funnell at McGill University in the Auditory Mechanics Lab. I learned new methods of thinking, like how to think scientifically, from him, which I consider to be a valuable life skill. In addition, he has significantly helped me in improving my writing and editing proficiency, as well as my problem-solving skills. Furthermore, he taught me the way to conduct scientific research through his valuable experience, remarkable patience, professional insight, logical perspective and knowledge. I deeply appreciate his effort, punctuality and promptness in reviewing and applying multiple comments to my works and thesis.

I would like to take this opportunity to greatly acknowledge my co-supervisor, Dr. Hamid Motallebzadeh, who provided me with his steadfast support, valuable knowledge, academic insight, and experience.

I would like to thank the Auditory Mechanics Lab present and past members for the great consultations and generous cooperation. They have made a significant contribution to both my personal and professional life at McGill.

I would like to thank all the stuff and academics at McGill University. Specifically, I would like to express my gratitude to Pina Sorrini, Sabrina Teoli and Trang Q. Tran for their prompt guidance, assistance, kindness and support for every student in the Biological and Biomedical Engineering Program. It would not have been possible for me and many others to study at the same pace and with the same level of satisfaction without their assistance and support. I would also like to thank Dr. Ross Wagner for his technical support.

Last but not least, I am very grateful to my beloved parents, Mehrnoosh and Ali. It would not have been possible for me to begin this chapter in my life without their support, love, passion, dedication, and kindness. I am also very thankful for the unconditional support and love from my sister, Nahal.

Thanks also to all those who shared their knowledge, views, and experiences with me. Additionally, I am grateful to all of our friends who supported and encouraged me as I prepared this dissertation. Furthermore, I would like to thank Shiva, one of my relatives, for her kindness and advice.

This work was supported by the Canadian Institutes of Health Research, the Natural Sciences and Engineering Research Council of Canada, the BioMedical Engineering Department, and the Faculty of Medicine and Health Sciences.

To my mother and father, Mehrnoosh and Ali,

the sunshine of my life

&

In memory of my grandmother

whose smile I will never forget

Abstract

Finite-element modelling of the response of the newborn middle ear to sound

Unidentified hearing loss in newborns affects speech and language development, academic achievement and social-emotional development. Unfortunately, currently available screening tools for hearing produce large numbers of false positives, largely because of middle-ear conditions. Tympanometry is a promising clinical tool for evaluating the condition of the middle ear by using sounds and quasi-static pressure together as inputs. However, tympanometry is poorly understood in newborns. Our overall objective is to use mathematical modelling to improve our understanding of how the newborn middle ear responds to different stimuli.

To simulate the effects of the large static pressures of tympanometry, a non-linear static model of a 22-day-old newborn ear canal and middle-ear was developed for the first time in our lab, without taking into account the dynamic behaviour of the ear. Later a linear version of the 22-day-old model was developed to simulate a broad range of frequencies but without the large static pressures. Most recently, a linear 1-day-old model was developed and its responses to static and low-frequency inputs (without inertial and damping effects) were simulated.

The specific objective of this study is finite-element simulation of the 1-day-old newborn middle-ear response to a broad range of frequencies.

Our existing model of the 1-day-old middle ear was revised and refined, and inertial and damping attributes were added. The thickness distribution of the eardrum of the 1-day-old model was calculated and compared with that of our previous 22-day-old model. Static and dynamic simulations were conducted, and results are presented as a low-frequency spatial vibration pattern and as frequency responses from 6.5 Hz to 10 kHz. At low frequencies the maximum displacement is located in the posterior region of the eardrum. A parameter-sensitivity analysis was conducted on different material parameters to determine how these parameter values affect model behaviour. The pars-tensa Young's modulus and bulk modulus, as well as the Prony

coefficients, had the greatest effects. The effects of the individual Prony coefficients are explored.

The model was compared with our previous 22-day-old model, and validated against data from the literature. The resonance frequency of our model is in the range of the frequencies of individual newborns .

This linear viscoelastic model provides insight into the response of the middle ear under different loading conditions. Ultimately this work will help us to better interpret tympanometry measurements and to improve newborn hearing screening.

Résumé

Modélisation par éléments finis de la réponse au son de l'oreille moyenne du nouveau-né

Une perte auditive non identifiée chez les nouveau-nés affecte le développement de la parole et du langage, les résultats scolaires et le développement socio-émotionnel. Malheureusement, les outils de dépistage de l'audition actuellement disponibles produisent un grand nombre de faux positifs, en grande partie à cause de l'état de l'oreille moyenne. La tympanométrie est un outil clinique prometteur pour évaluer l'état de l'oreille moyenne en utilisant les sons et la pression quasi-statique comme entrées. Cependant, la tympanométrie est mal comprise chez les nouveau-nés. Notre objectif global est d'utiliser la modélisation mathématique pour améliorer notre compréhension de la façon dont l'oreille moyenne du nouveau-né répond à différents stimuli.

Pour simuler les effets des grandes pressions statiques de la tympanométrie, un modèle statique non linéaire du conduit auditif et de l'oreille moyenne d'un nouveau-né de 22 jours a été développé pour la première fois dans notre laboratoire, sans tenir compte du comportement dynamique de l'oreille. Plus tard, une version linéaire du modèle de 22 jours a été développée pour simuler une large gamme de fréquences, mais sans les grandes pressions statiques. Plus récemment, un modèle linéaire d'un nouveau-né de 1 jour a été développé et ses réponses aux entrées statiques et de basse fréquence (sans effets d'inertie et d'amortissement) ont été simulées.

L'objectif spécifique de cette étude est la simulation par éléments finis de la réponse de l'oreille moyenne du nouveau-né de 1 jour à une large gamme de fréquences.

Notre modèle existant de l'oreille moyenne d'un jour a été révisé et affiné, et des attributs d'inertie et d'amortissement ont été ajoutés. La distribution de l'épaisseur du tympan du modèle de 1 jour a été calculée et comparée à celle de notre modèle précédent de 22 jours. Des simulations statiques et dynamiques ont été effectuées, et les résultats sont présentés sous la forme d'un modèle de vibrations spatiale à basse fréquence et de réponses en fréquence de 6.5 Hz à 10 kHz. Aux basses fréquences, le déplacement maximal est situé dans la région postérieure du tympan. Une analyse de sensibilité aux paramètres a été menée sur différents

paramètres du matériau pour déterminer comment les valeurs des paramètres affectent le comportement du modèle. Le module d'Young et le module volumique de la pars tensa, ainsi que les coefficients de Prony, ont eu les effets les plus importants. Les effets des coefficients de Prony individuels sont explorés. Le modèle a été comparé à notre modèle précédent de 22 jours, et validé par rapport aux données de la littérature. La fréquence de résonance de notre modèle est dans la gamme de celles des nouveau-nés individuels.

Ce modèle viscoélastique linéaire donne un aperçu de la réponse de l'oreille moyenne dans différentes conditions de charge. Ultimement, ce travail nous aidera à mieux interpréter les mesures de tympanométrie et à améliorer le dépistage auditif des nouveau-nés.

Table of Contents

Acknowledgments....i
Abstract....iv
Résumé....vi
List of Figures....x
List of Tables....xii
List of Symbols....xiii
List of Acronyms and Abbreviations....xv
Chapter 1. Introduction....1
1.1 Motivation....1
1.2 Objectives....3
1.3 Thesis outline....3
Chapter 2. The auditory system....4
2.1 Introduction....4
2.2 Anatomy of the outer and middle-ear....4
2.2.1 Overview of ear anatomy....4
2.2.2 Pinna....5
2.2.3 Ear canal....6
2.2.4 Tympanic membrane....7
2.2.5 Ossicles....7
2.2.6 Ossicular ligaments....9
2.2.7 Middle-ear muscles....10
2.3 Development of the ear....10
Chapter 3. Literature review....12
3.1 Introduction....12
3.2 Tympanometry....12
3.2.1 Introduction....12
3.2.2 Principles of tympanometry....12
3.2.3 Tympanogram interpretation....15
3.2.4 Clinical applications of tympanometry....17
3.2.5 Tympanometry in newborns....19
3.3 Experimental measurements....20
3.3.1 Introduction....20
3.3.2 Non-gerbil tympanic-membrane vibrations....20
3.3.3 Gerbil tympanic-membrane vibrations....22
3.3.4 Material properties of the middle-ear soft tissues....23
3.4 Viscoelastic material models....25
3.5 Finite-element modelling....29
3.5.1 Introduction....29
3.5.2 Finite-element software....31
3.6 Finite-element models of the ear....31
Chapter 4. Materials and methods....37
4.1 Introduction....37
4.2 Methods for creating the middle-ear model....37
4.3 Current model components and modifications....41

4.4 Simulation software and hardware....46
4.5 Tympanic-membrane thickness....46
4.5.1 Tympanic-membrane thickness in 22-day-old model....46
4.5.2 Thickness calculation algorithms....47
4.5.3 Ray-triangle intersection algorithm....48
4.6 Material properties....48
4.6.1 Introduction....48
4.6.2 Young's modulus....49
4.6.2.1 Pars tensa....49
4.6.2.2 Pars flaccida....51
4.6.2.3 Ligaments....51
4.6.2.4 Ossicles....51
4.6.3 Poisson's ratio....52
4.6.4 Density....53
4.6.5 Prony series parameters....53
4.7 Discrete elements....56
4.7.1 Spring....56
4.7.2 Cochlear load....57
4.8 Boundary conditions....59
4.9 Loading conditions and time-step analysis....59
4.10 Sensitivity analysis....61
Chapter 5. Results....62
5.1 Introduction....62
5.2 Geometry and mesh pattern....62
5.3 Thickness....66
5.3.1 1-day-old model thickness distribution....66
5.3.2 Comparison of 1-day-old model and 22-day-old model....66
5.4 Static displacement for distinct nodes....71
5.5 Low-frequency tympanic-membrane vibration pattern....72
5.6 Time-domain and frequency-domain responses....74
5.7 Parameter sensitivity analysis....77
5.8 Sensitivity analysis of individual Prony coefficients....86
5.9 Comparison with 22-day-old model....90
5.9.1 Introduction....90
5.9.2 Effect of ear-canal wall....90
5.9.3 Effect of middle-ear cavity....91
5.9.4 Comparison with 22-day-old model and measured data....92
Chapter 6. Conclusion....95
6.1 Summary....95
6.2 Future work....97
6.3 Significance....99
References....102

List of Figures

Figure 2.1: Schematic overview of ear anatomy, divided into three parts: the outer ear, middle ear, and inner ear.....5
Figure 2.2: Pinna with its different components.....6
Figure 2.3: TM anatomy.....7
Figure 2.4: Ossicles. (A) Malleus. (B) Incus. (C) Stapes.....9
Figure 2.5: Comparison of ear anatomy between newborns and adults.....11
Figure 3.1: Schematic view of tympanometery.....14
Figure 3.2: Qualitative method for analyzing tympanograms, including Type A, Type B, Type C, Type D and Type E.....15
Figure 3.3: Quantitative analysis based on equivalent ear canal volume, peak static acoustic admittance, tympanogram peak pressure and tympanogram width.....16
Figure 3.4:Three main characteristics of viscoelastic material.....27
Figure 3.5: Generalized SLS model, or generalized Maxwell model, with n series dashpot-and-spring branches in a parallel arrangement.....27
Figure 4.1: Fie (http://audilab.bme.mcgill.ca/sw/fie.html) graphical user interface used for segmentation of CT images.....38
Figure 4.2: Example of triangulation between two lines in different slices by employing Tr3 (http://audilab.bme.mcgill.ca/sw/tr3.html) as a step in creating a 3D model.....39
Figure 4.3: 3D visualization of the 1-day-old TM model in Thrup'ny (http://audilab.bme.mcgill.ca/sw/thrupny.html).....40
Figure 4.4: CT scan of the 1-day-old ear.....42
Figure 4.5: Results of convergence study conducted by Shaho for TM models of 1-day-old and 22-day-old, with five different XY-resolutions of the mesh.....44
Figure 4.6: Final geometry of the 1-day-old model used in this study.....45
Figure 4.7: Finite-element mesh of the model.....45
Figure 4.8: Effects of uniform Prony coefficients on frequency response of TM.....55
Figure 4.9: Effects of very low Prony coefficients on frequency response of TM.....56
Figure 4.10: Effect of different time-step sizes on simulated PT response.....61
Figure 5.1: Posterior views of 1-day-old models.....63

Figure 5.2: Three views of 1-day-old models.....64
Figure 5.3: Mesh differences between 1-day-old models.....65
Figure 5.4: Distribution of TM thickness in 1-day-old model.....66
Figure 5.5: Comparison of the TM in 1-day-old model and 22-day-old model in terms of thickness and curvature.....71
Figure 5.6: Comparison of static displacements of the PT posterior point, PT anterior point, umbo, stapes (represented by a point on the incus), and middle of the PF.....72
Figure 5.7: Medial view of displacement patterns of the 1-day-old middle ear model.....73
Figure 5.8: Medial view of the magnitude of displacement for the 22-day-old middle ear model of Motallebzadeh et al. (2017a) in response to sound pressure at 100 Hz.....74
Figure 5.9: Dynamic response in the time domain for five different locations of the 1-day-old model.....75
Figure 5.10: Frequency responses of five different regions of 1-day-old model. Regions include posterior PT, anterior PT, umbo, incus, and centre of PF.....77
Figure 5.11: Changes in the maximum TM displacement magnitude at a low frequency (100 Hz) when the model parameters were changed by ±10%, ±20% and ±40%.....78
Figure 5.12: Changes in the umbo displacement magnitude at a low frequency (100 Hz) when the model parameters were changed by ±10%, ±20% and ±40%.....79
Figure 5.13: Changes in the middle-ear resonance frequency when the parameters of the model were changed ±10%, ±20% and ±40%.....80
Figure 5.14: Changes in the maximum TM displacement magnitude of the resonance peak when the parameters of the model were changed ±10%, ±20% and ±40%.....81
Figure 5.15: Changes in the umbo displacement magnitude at the resonance peak when the parameters of the model were changed ±10%, ±20% and ±40%.....82
Figure 5.16: Changes in the TM displacement magnitude at a low frequency (100 Hz) when selected parameters of the model were changed by ±10%, ±20% and ±40%.....83
Figure 5.17: Changes in the umbo displacement magnitude at a low frequency (100 Hz) when selected parameters of the model were changed by ±10%, ±20% and ±40%.....84
Figure 5.18: Changes in the middle-ear resonance frequency when selected parameters of the model were changed by ±10%, ±20% and ±40%.....85

Figure 5.19: Effects of selected parameters on the resonance magnitude of the TM when selected parameters of the model were changed by ±10%, ±20% and ±40%.....85
*Fi*gure 5.20: Effects of selected parameters on the resonance magnitude of the umbo when selected parameters of the model were changed by ±10%, ±20% and ±40%.....86
Figure 5.21: Effects of individual Prony coefficients on low-frequency magnitude (100 Hz) of the TM when they were changed by ±10%, ±20% and ±40%.....87
Figure 5.22: Effects of individual Prony coefficients on low-frequency magnitude (100 Hz) of the umbo response when they were changed by ±10%, ±20% and ±40%.....87
Figure 5.23: Effects of individual Prony coefficients on middle-ear resonance frequency when they were changed by ±10%, ±20% and ±40%.....88
Figure 5.24: Effects of individual Prony coefficients on resonance magnitude of the TM when they were changed by ±10%, ±20% and ±40%.....89
Figure 5.25: Effects of individual Prony coefficients on the resonance magnitude of the umbo when selected parameters of the model were changed by ±10%, ±20% and ±40%.....89
Figure 5.26: Volume displacement of 22-day-old model with ear-canal wall that is either rigid (blue curve) or compliant (black curve).....91
Figure 5.27: Volume displacement of 22-day-old model with and without middle-ear cavity.....92
Figure 5.28: Comparison of frequency-response shapes between 1-day-old and 22-day-old model responses.....93

List of Tables

Table 4.1: Material properties from the literature and the baseline values used in this study.....64

List of Symbols

B	Bulk modulus
B	Susceptance
C	Damping matrix
E_i	Elastic modulus of the i-th spring
E_∞	Elastic modulus of the free spring
E	Young's modulus
f	Applied nodal force vector
f_i	Frequency corresponding to i-th Prony coefficient
$G(t)$	Normalized relaxation function
G	Conductance
g_i	i-th Prony coefficient
j	$\sqrt{-1}$
K	Element stiffness matrix
M	Mass matrix
P	Acoustic pressure
R	Resistance
S^e	Elastic function
$S(t)$	Total second Piola–Kirchhoff stress tensor
t	Time
U	Volume velocity
u	Vector of nodal displacement
V_{ea}	External acoustic meatus volume

X	Reactance
Y	Admittance
Y_a	Input admittance at probe tip
Y_{ec}	Admittance of the ear-canal volume
Y_{tm}	Admittance at the TM
Z	Impedance
ε	External strain
ε_∞	Strain of the free spring
η_i	Viscous coefficient of the i-th dashpot
ν	Poisson's ratio
σ	Total stress
σ_∞	Stress of the free spring
τ_i	Time constants
φ	Admittance phase angle
ω_i	Angular frequency

List of Acronyms and Abbreviations

ABR	Auditory brainstem response
AML	Anterior mallear ligament
CT	Computed tomography
EAC	External auditory canal
FE	Finite element
FFT	Fast Fourier transform
Fie	Fabrication d’imagerie extraordinaire
FWHM	Full width at half maximum
gw	Gestational weeks
IMJ	Incudomallear joint
ISJ	Incudostapedial joint
LDV	Laser Doppler vibrometry
MicroCT	Microscale computed tomography
MRM	Magnetic resonance microscopy
OAE	Otoacoustic emission
PF	Pars flaccida
PIL	Posterior incudal ligament
PT	Pars tensa
SLS	Standard linear solid
TM	Tympanic membrane
TPP	Tympanogram peak pressure
TW	Tympanometric width

Chapter 1. Introduction

1.1 Motivation

Hearing loss is one of the most common congenital disorders and the incidence of newborns born with hearing loss is 3-4 babies per 1,000 (Deltenre & Van Maldergem, 2013). Early detection of hearing loss at the time of birth along with early intervention is considered crucial to prevent problems related to language and speech development. Language and speech difficulties affect different aspects of human life like daily communication, educational achievement, psychosocial development, and employment opportunities in later life (Joint Committee on Infant Hearing, 1995, 2007). The same applies to mild hearing loss.

There are two main types of hearing loss: sensorineural hearing loss which affects the inner ear, auditory nerve or central auditory pathway; and conductive hearing loss which affects the outer ear and/or middle ear. Hearing loss that is both conductive and sensorineural is known as mixed hearing loss. Sensorineural hearing loss is the most common permanent hearing loss in newborns (e.g., Marazita et al., 1993). However, transient conductive hearing losses may interfere with hearing loss detection and diagnosis (e.g., Chang et al., 1993).

There is widespread agreement that all babies should have their hearing assessed by one month of age and, if necessary, should receive a diagnostic examination by three months, followed by the necessary treatment by six months (e.g., Bagatto & Moodie, 2016). Screening hearing of newborns immediately after birth when newborns are still in hospital provides the advantages of having a concentration of skilled and knowledgeable screeners and of preventing loss to follow-up.

In newborn hearing screening programs, otoacoustic emission (OAE) and/or auditory brainstem response (ABR) tests are currently used as screening tools. The widespread use of neonatal hearing screening raises serious concerns due to the high false positive rates of these tests (Nelson et al., 2008). These high false-positive rates are usually related to the transient remaining vernix, mesenchyme, and amniotic fluid in the outer and middle ear during the first few days of life, which temporarily decreases the transmission of sound between the inner ear and outer ear.

This situation is in opposition to the need for an in-hospital screening program and shorter hospital stays.

Having an easy method to assess the impact of transient fluid and tissue in the outer and middle ear during screening, and to check for conductive hearing loss during follow-up diagnosis, would be very helpful to improve screening and diagnosis.

Admittance measurement is considered a promising tool for assessing the condition of the outer and middle ear in newborns. This method measures acoustic input admittance in the outer and middle ear in response to a single-frequency or wideband acoustic stimulus. Wideband admittance measurement provides considerably more information about the middle ear than single-frequency measurement does (e.g., Merchant & Neely, 2021), but it is still poorly understood and not yet applied in clinical settings.

Tympanometry provides further information by applying a quasi-static air pressure in the ear canal along with the acoustic stimulus. Usually, tympanometry is conducted with a low-frequency probe tone of 226 Hz. This provides easy-to-interpret results for adult ears, but the results in newborns vary greatly from those in adults and are not completely understood. Anatomical and physiological changes occur during maturation which may explain the differences in results. Some studies have found that tympanometry with a 1-kHz tone improves the ability to distinguish between normal and liquid-filled middle ears in newborns, although the degree of the distinction remains debatable and is far from perfect (e.g., Margolis et al., 2003). In addition, Keefe et al. (1993) reported that in newborns and infants the main middle-ear resonance occurs at around 1.8 kHz. This shows that the measurements can be sensitive to what frequency is employed and the location of the resonance that occurs in an ear. Tympanometric results are also influenced by many procedural variables, like the direction and rate of the quasi-static pressurization and what frequency was used. It is not apparent how these factors specifically impact tympanometry.

Acoustics and biomechanics play a large role in the middle ear, and a better understanding of sound transmission through the middle ear will improve screening and diagnosis. In particular, considering the number of variables that affect tympanometry results as mentioned earlier, it is important to study newborn middle-ear mechanics to better understand hearing-test outcomes.

The aim of this study is to use mathematical models to provide a better understanding of the middle ear response and ultimately to improve clinical tools. In such models, we can study the effects of different parameters quantitatively and analyze the complex system to better understand the functions of different middle-ear components. It is also possible to interpret clinical data and predict the effects of abnormal conditions using these models, Several approaches to modelling the middle ear were reviewed by (Funnell et al., 2013). The finite-element method is used here to model the 1-day-old middle ear, allowing us to represent the details of the anatomical and mechanical properties with the model's structure and parameters in order to predict the behaviour of the middle ear.

1.2 Objectives

The overall objective of this study is to improve our understanding of newborn middle ear behaviour and its response to sound stimuli using mathematical modelling. The specific objectives of this study are as follows:

1. Investigate the behaviour of the middle ear under acoustic stimuli by extending our existing 1-day-old model to dynamic conditions.
2. Analyze the effects of different model parameters on the model's behaviour.
3. Make a preliminary comparison with our 22-day-old model in terms of resonance frequency and low-frequency magnitude.

1.3 Thesis outline

A brief overview of the auditory system and its anatomy is presented in Chapter 2, with a focus on the middle ear. A literature review, summary of prior research, background information, and concepts that are relevant to the current work are presented in Chapter 3. The methods are described in Chapter 4, and our results are then presented in Chapter 5. In Chapter 6, a summary of this work, a discussion of possible future work, and the importance of our research are presented.

Chapter 2. The auditory system

2.1 Introduction

As a result of the auditory system, we are able to hear. The auditory system gathers the sound signals and then transforms and amplifies them before they are delivered via a neural channel to the brain for interpretation. In many anatomy textbooks, the anatomy of the ear is described in detail and illustrated (e.g., Standring, 2021). An overview of the outer and middle ear is given in Section 2.2, based largely on Standring (2021). The major parts of the external and middle ear are discussed in more detail, with their functions and roles, concentrating on the middle ear since it is the most pertinent to this study. The development of the major parts of the external ear and middle ear that have significant effects on the ear acoustic response are discussed in Section 2.3.

2.2 Anatomy of the outer and middle-ear

2.2.1 Overview of ear anatomy

The following information is mostly based on Standring (2021) and Casale et al. (2022). The ear is made from small, complex and connected structures that play a role in the balance and hearing senses. Ear anatomy is usually divided into the outer ear, middle ear, and inner ear as shown in Figure 2.1. Sound is transmitted by pressure waves and they are first caught by the pinna, which is the visible portion of the outer ear, and then pass through the ear canal. After that, the sound wave reaches a part of the middle ear called the tympanic membrane (TM), or eardrum. The TM is located at the end of the ear canal and separates the outer ear from the middle ear. The TM transmits vibrations to the oval window of the cochlea through three bones located in the middle ear that form the ossicular chain.

There are three main components of the inner ear: the cochlea, vestibule, and semicircular canals. Unlike the outer and middle ear, the cochlea is filled with liquid. The liquid moves in response to the sound vibrations, and the vibrations are converted to electrical impulses by mechanically stimulating the stereocilia (little hairs on the tops of the hair cells) within a structure known as the organ of Corti. These nerve impulses are transmitted from the cochlea to

the brain by the auditory nerve (eighth cranial nerve). The brain then translates these impulses to meaningful and recognizable sounds.

There are number of structures in the middle-ear cavity that are necessary for normal hearing, including ossicular muscles, tendons and ligaments, and the Eustachian tube. The ossicular ligaments and muscles are discussed in more detail in Sections 2.2.6 and 2.2.7.

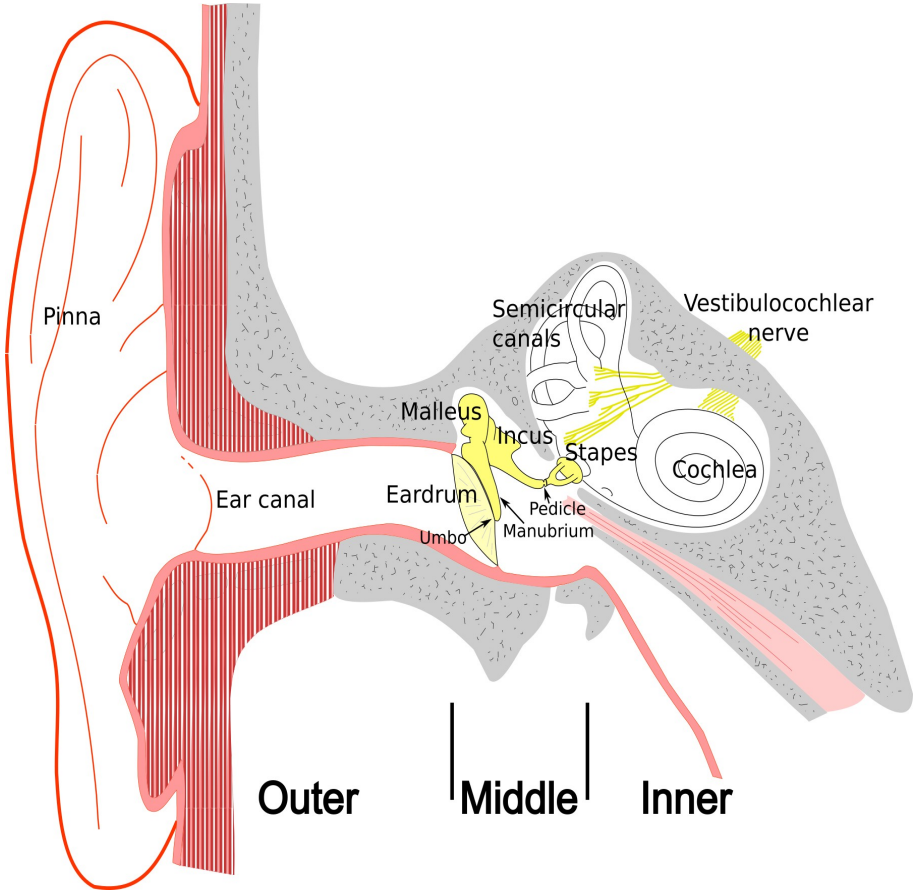

Figure 2.1: Schematic overview of ear anatomy, divided into three parts: the outer ear, middle ear, and inner ear.

2.2.2 Pinna

The pinna or auricle is the visible part of the ear and it protrudes from the side of the skull. Its main material is flexible fibro-cartilage and the thickness is about one to two millimetres. Sound waves are captured by the pinna, which then funnels them toward the ear canal and TM.

The following anatomical information is mostly based on Roosa (1891). Figure 2.2 shows the different parts of the pinna. The edge that forms the outer border of the pinna is named the helix. Just under the helix is the fossa which separates it from a second ridge-like border called the

antihelix. The cartilage becomes thickened in front of the opening to the auditory canal and forms a projection or edge named the tragus. Just opposite to the tragus across the opening of the auditory canal is a similar projection called the anti-tragus. The largest concavity of the pinna is called the concha. Above the concha, there is a triangular depression called the fossa helicis. At the lower extremity of the pinna, a projection can be seen called the lobe.

The pinna first shows as six small mounds, named the six hillocks of His, at 6 gestational weeks (gw) in humans. After the hillocks of His have fused, the pinna continues to increase in size, peeling away from the head at 18 gw, and reaches its adult morphology at 22 gw (Anthwal & Thompson, 2016). It reaches its adult size around the age of six to nine years (Anson, 1981).

Figure 2.2: Pinna with its different components.
(1) Helix; (2) Anti-helix; (3) Fossa helicis; (4) Concha ; (5) Anti-tragus; (6) Tragus; (7) Lobe (Roosa, 1891).

2.2.3 Ear canal

The function of the external auditory canal (EAC) is to direct sound waves towards the TM in the middle ear (Mozaffari et al., 2021). In adults, approximately the outer one third of the EAC wall is cartilaginous and the inner two thirds are bone. The anteroinferior wall of the EAC is about 31 mm long while the posterosuperior wall is only about 25 mm long due to the slope of the TM (Kelly & Mohs, 1996). In adult humans, the EAC is typically about 8 mm in diameter. For the purpose of coating, protecting and lubricating the lining of the ear canal, the outer cartilaginous

section contains many sebaceous and ceruminal glands which produce cerumen (ear wax) (Mozaffari et al., 2021).

2.2.4 Tympanic membrane

The following information is mostly based on Lim (1970) and Standring (2021). The TM, also known as the eardrum, is a thin, semi-transparent membrane. The TM is positioned obliquely from the canal floor and divides the tympanic cavity from the external auditory canal. The TM's shortest diameter is 8 to 9 mm and its longest diameter is 9 to 10 mm. The TM's circumference mostly contains the thickened fibrocartilaginous ring or annulus which contains radially oriented smooth muscle cells that probably act on controlling blood flow or maintaining tension. The annulus is connected to the bony tympanic sulcus located at the medial end of the canal. The TM has a conical shape that points inward while the curved sides of the cone are convex outward. There is a notch in the superior part of the sulcus. This notch is connected to the lateral process of the malleus by two bands, the anterior and posterior mallear folds. Above these folds is located the pars flaccida (PF), a small triangular part of the TM. Most of the TM is composed of the pars tensa (PT). The PT is cone-shaped and its apex, the umbo, points towards the middle-ear cavity. The PF is lax and thicker than the PT. In Figure 2.3, the manubrium is a part of the malleus that is attached to the medial surface of the TM.

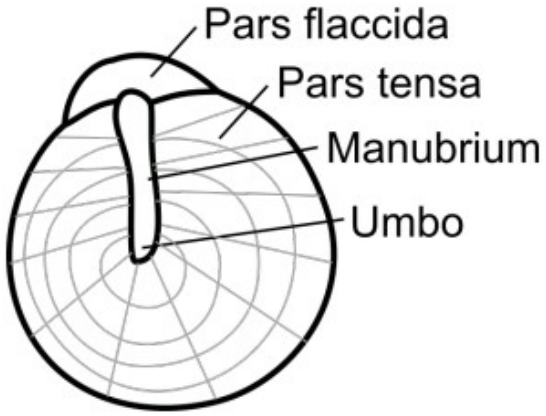

Figure 2.3: TM anatomy.
(Adapted from http://audilab.bme.mcgill.ca/teach/me_saf/)

2.2.5 Ossicles

The information about the ossicles in this section is mostly obtained from (Standring, 2021). The ossicles consist of three small bones called the malleus, incus and stapes. An overview of the

three ossicles in their location in the middle ear is shown in Figure 2.4. Malleus, incus and stapes are the Latin terms for mallet or hammer, anvil, and stirrup, and as shown in Figure 2.4 their names are derived from their shapes. The malleus is the largest ossicle, measuring 8–9 mm long. It includes a head, neck, handle (manubrium), and anterior and lateral processes. It is attached to the TM by the lateral margin of its handle and transmits the auditory oscillations to the incus. The malleus head is attached to the incus by the incudomallear joint (IMJ). The incus includes a body and two processes. The lower end of the long process of the incus bends medially and ends in a circular lenticular process. The lenticular process is connected to the head of the stapes, the third of the ossicles, through the incudostapedial joint (ISJ). The stapes includes a head, neck, two limbs (processes or crura) and a footplate or base. The posterior crus and anterior crus of the stapes reach the footplate, which is in contact with the oval window of the inner ear, transferring mechanical energy to the liquid-filled inner ear.

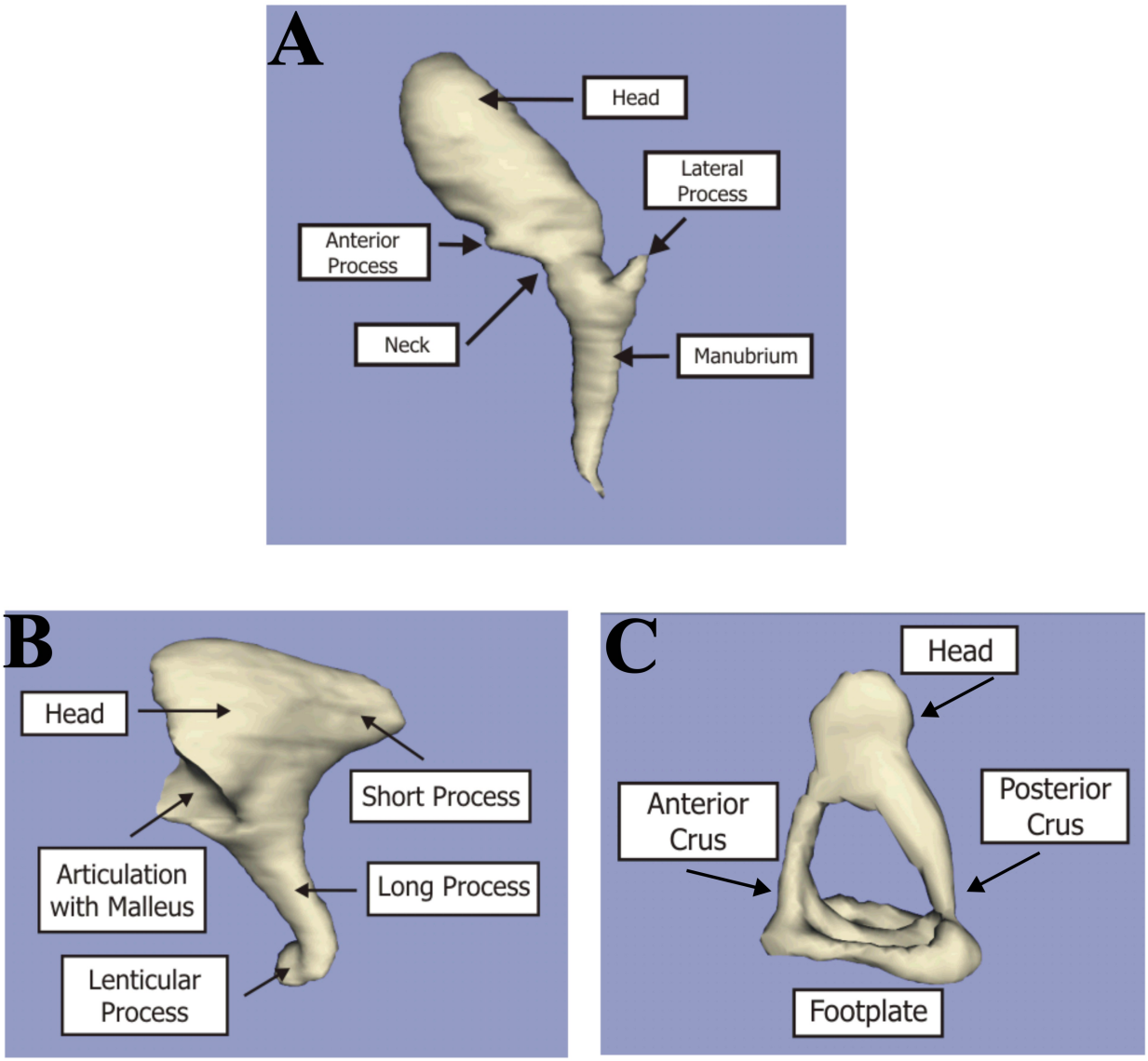

Figure 2.4: Ossicles. (A) Malleus. (B) Incus. (C) Stapes.
(After http://audilab.bme.mcgill.ca/~daren/3Dear/3d_models.html)

2.2.6 Ossicular ligaments

A ligament is a sheet or band of fibrous tissue that connects two or more bones, cartilages or other structures, or provides support for muscles or fasciae (Wolff & Bellucci, 1956). Ligaments connect the ossicles to the walls of the tympanic cavity. Some of them may be just mucosal folds carrying nerves and blood vessels to the ossicles and their articulations, while others can have a central collagen band (Standring, 2021). Authors may disagree over the naming and existence of certain middle-ear ligaments, particularly the mallear ligaments (e.g., Mikhael et al., 2005).

The following information is mostly based on Møller (1974) and Standring (2021).

The anterior mallear ligament (AML) stretches from just above the anterior process of the malleus to the anterior bony wall of the tympanic cavity. It may include muscle fibres, named laxator tympani or musculus externus mallei. The lateral mallear ligament is a triangular band that extends from the tympanic incisure's posterior border to the malleus head. The superior mallear ligament, which is connected to the malleus head, forms a further attachment to the middle-ear cavity wall. The posterior incudal ligament (PIL) is attached to the short (posterior) process and the superior incudal ligament is attached to the incudal body and they both connect the incus to the cavity wall.

The footplate of the stapes is attached to the oval window of the cochlea by the annular ligament.

2.2.7 Middle-ear muscles

The middle-ear muscles can change the mechanical characteristic of the middle ear and modulate how sound vibrations are transmitted to the cochlea. The acoustic reflex is the reflexive contraction of the muscles in the middle ear as a response to sound stimulation and has been used clinically for decades to diagnose middle-ear, cochlear and VIIIth-nerve disorders (Musiek & Chermak, 2015, p. 18). The stapedius and tensor tympani muscles control this reflex. They are connected to the stapes neck and malleus neck, respectively. These muscles attenuate the vibrations of the ossicular chain in response to high sound levels or internal noises such as speech and mastication. The stapedius muscle makes the stapes attachment to the oval window stiffer and the tensor tympani pulls the malleus medially, increasing the TM tension (Schofield & Beebe, 2020).

2.3 Development of the ear

Newborns and adults have many physiological and anatomical differences in their outer and middle ears. Figure 2.5 shows some of the anatomical differences. In infants, the canal cross section is almost oval in shape and the canal is shorter and narrower than in adults. Almost all of the newborn EAC is surrounded by soft tissue, while in adults the inner two thirds are surrounded by bone. The cartilaginous canal becomes visible during embryonic development, while the osseous canal develops after birth. Because of the absence of ossification, the external

ear canal varies in volume significantly in response to high static pressures (e.g., Holte et al., 1990; Qi et al., 2006a). It takes two years after birth for the bony tympanic ring to fully develop. In the first three years of life, the surrounding bony wall of the ear canal develops.

In newborns the TM and ossicles have the same size as in adults, but after birth they continue to mature (e.g., Saunders et al., 1983, p. 10). The TM in newborns is thicker than in adults. The relative orientations of the TM and ear canal change. The size of the air-filled mastoid cavity increases greatly after birth. During the first hours and days after birth the residual vernix, mesenchyme and amniotic fluid in the outer and middle ear are eliminated.

All of these differences modify the sound-conducting properties of the outer and middle-ear and ultimately affect newborn hearing screening results and the interpretation of tympanograms (e.g., Holte et al., 1990; Hunter et al., 2010). (Tympanograms are explained in Chapter 3.) For example, Holte et al. (1990) found that EAC wall mobility and tympanometric characteristics vary in the first four months after birth, and André et al. (2012) found that the middle-ear resonance frequency increases in the first three months.

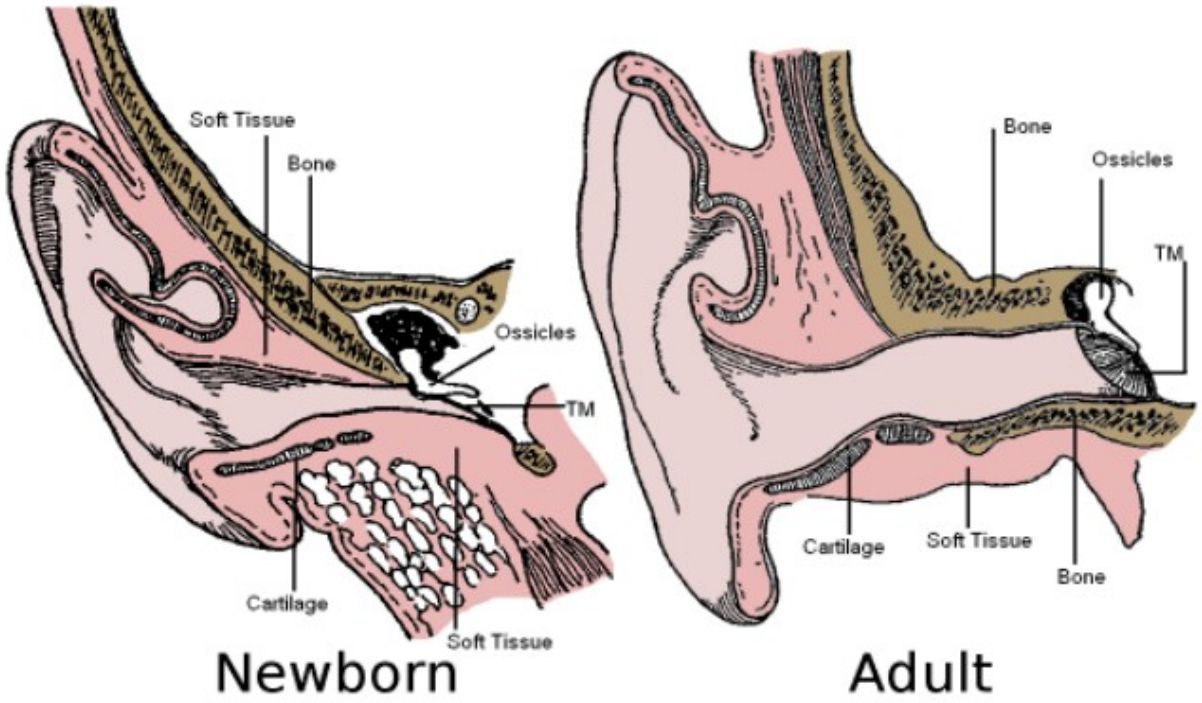

Figure 2.5: Comparison of ear anatomy between newborns and adults.
(After Fowler EP Jr. (1947): Medicine of the ear, 2nd ed., T. Nelson, New York, from http://audilab.bme.mcgill.ca/teach/me_saf/)

Chapter 3. Literature review

3.1 Introduction

A literature review of the concepts and prior studies related to this study is presented in this chapter. In Section 3.2, tympanometry is defined and discussed. In Section 3.3, a review of the finite-element method and its application in the light of auditory research is presented. An overview of the underlying viscoelastic material models, one of the primary focuses of this study, is presented in Section 3.4, followed by a review of the finite-element models of the ear in Section 3.5. Finally, a review of experimental studies on the middle ear, including non-gerbils and gerbils, is presented in Section 3.6.

3.2 Tympanometry

3.2.1 Introduction

Tympanometry is a promising clinical tool for evaluating middle-ear conditions in newborns. In Section 3.2.2, an introduction to the principles of tympanometry is given, then after a discussion of the interpretation of tympanometry results in Section 3.2.3, its clinical application is discussed in Section 3.2.4. Finally, in Section 3.2.5, the application of tympanometry in newborns is summarized.

3.2.2 Principles of tympanometry

The following information is based mainly on Stach & Ramachandran (2017), Dalmont (2001), Rosowski & Wilber (2015), Lidén et al. (1977), and Van Camp et al. (1986).

All mechanical vibration systems have a physical characteristic called immittance. In very general terms, immittance measures how readily the system vibrates in response to a driving force. In the clinical assessment of middle-ear function, two common clinical tests that use immittance are tympanometry and acoustic reflex thresholds.

Immittance refers to both impedance Z and admittance Y. Impedance is a measurement of the resistance to motion that a structure exhibits in the presence of a harmonic force. Admittance is the reciprocal of impedance.

In acoustics, the admittance of a system is defined as

$$Y = 1/Z = U/P \tag{3-1}$$

where U is the volume velocity at the point of measurement, that is, the volume of fluid (e.g., air) that passes through a unit surface area per unit time, and P is the acoustic pressure at the point of measurement. The unit for acoustic admittance is mho (m^3/Pa.s), and the unit for impedance is ohm.

Both admittance and impedance are complex numbers, which can be expressed either as real and imaginary parts or as magnitude and phase. Impedance consists of a real part, resistance (R), and an imaginary part, reactance (X):

$$Z = R + jX. \tag{3-2}$$

Admittance consists of a real part, conductance (G), and an imaginary part, susceptance (B):

$$Y = G + jB, \tag{3-3}$$

where j stands for $\sqrt{-1}$ in both equations.

Immittance measurement is done to investigate the condition of the middle ear, but it is impossible to put the tip of the probe at the TM. Instead, it is placed near the ear canal entrance. At low frequencies where the sound-pressure field is almost uniform within the ear canal, the input admittance at the probe tip (Y_a) equals the sum of the admittance of the ear-canal volume (Y_{ec}) and the admittance at the TM (Y_{tm}). If we know Y_{ec}, then we can calculate Y_{tm} from Y_a. The acoustic stimulus for admittance measurement can be in the form of a wideband signal or a single frequency.

Tympanometry is conducted by applying a range of quasi-static pressures in the ear canal in addition to the acoustic stimulus. Figure 3.1 shows a schematic of a tympanometer. A soft plastic probe is inserted into the ear canal and seals the air in the canal. The probe consists of three components: a sound source, a microphone, and a pump. The sound source transmits a known

volume velocity to the ear canal via a tube (Figure 3.1). The microphone measures the sound pressure level in the ear canal at the tip of the probe. The voltages at the sound source and at the microphone output are converted to an equivalent admittance value. The pump generates a quasi-static pressure between −400 and +400 daPa (−4 and +4 kPa), going from negative to positive pressures or vice versa. (In clinical tympanometry, daPa (= 10 Pa) is usually used as a unit).

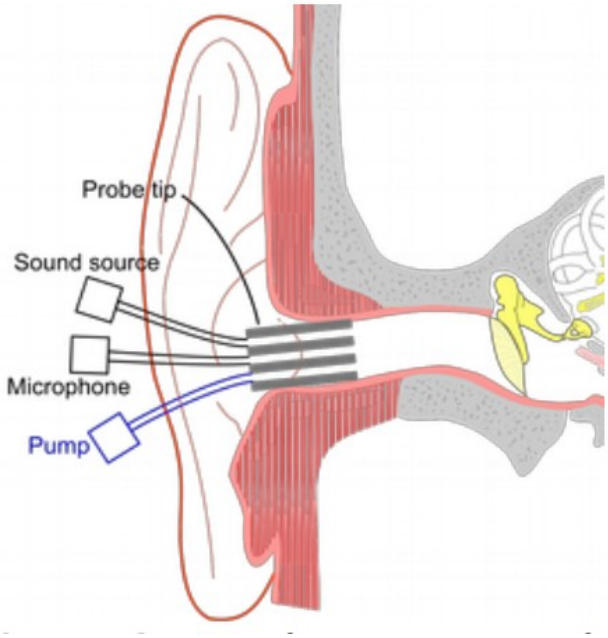

Figure 3.1: Schematic view of tympanometery.
(After Funnell, http://audilab.bme.mcgill.ca/teach/me_obj/)

Terkildsen & Thomsen (1959) introduced tympanometry as a method for assessing the middle ear pressure and status. Since then, tympanometry has become a routine part of audiological and otological evaluations around the world.

According to Terkildsen & Thomsen (1959), we can measure Y_{ec} independently when a large static pressure like 200 daPa is applied. The TM and other structures of the middle ear are pushed almost to their limits at such a high pressure and become almost incapable of vibrating. Therefore, all (or at least most) of the energy sent by the probe tip is reflected at the eardrum surface, making $Y_a \approx Y_{ec}$. Several studies have demonstrated that 200 daPa is actually insufficient to drive the admittance of the TM to zero (e.g., Shanks & Lilly, 1981).

3.2.3 Tympanogram interpretation

Tympanograms are plots of acoustic admittance for a given probe-tone frequency as a function of changing air pressure in the external ear canal.

Tympanograms are asymmetrical, with greater admittance values for positive pressure values than for negative values. Various causes of the asymmetry have been proposed, including the movement of the eardrum, enlargement of the cartilaginous ring of the TM, and viscoelasticity of the soft tissues (Elner et al., 1971).

Several methods for classifying and interpreting tympanograms have been proposed. Analyzing a tympanogram can be done qualitatively or quantitatively. Qualitative methods take into account the overall shape of the tympanogram (e.g., Figure 3.2), while quantitative methods take into account specific measurable characteristics (e.g., Figure 3.3) (Katz, 1978).

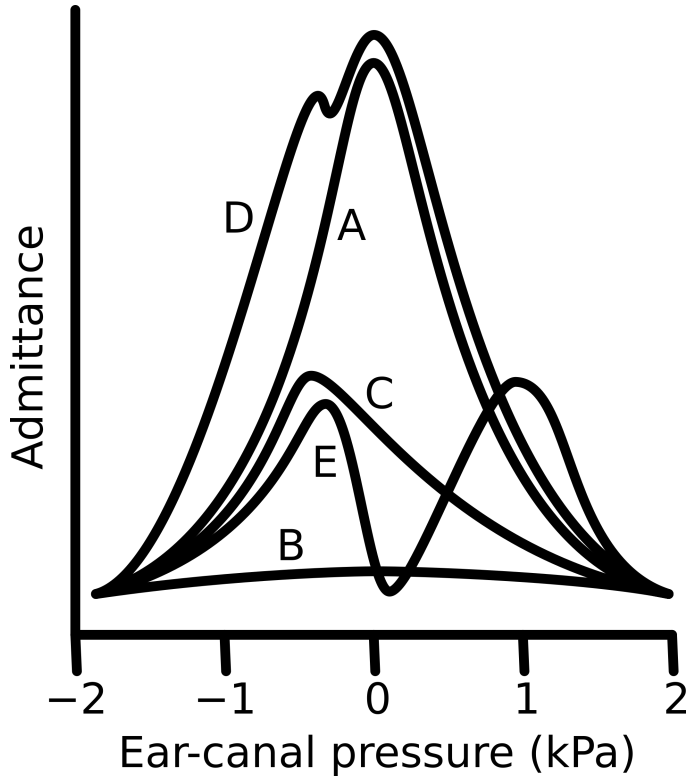

Figure 3.2: Qualitative method for analyzing tympanograms, including Type A, Type B, Type C, Type D and Type E.
(After Qian, 2019)

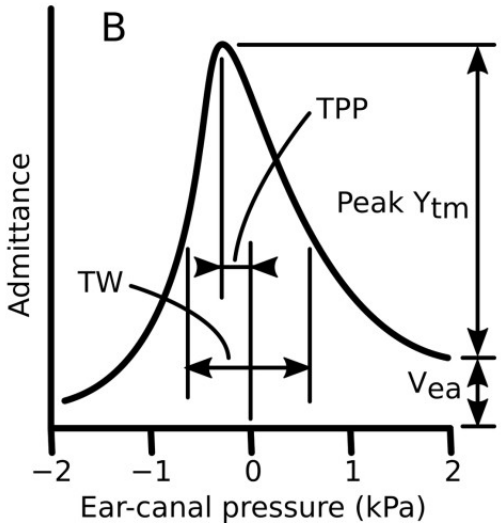

Figure 3.3: Quantitative analysis based on equivalent ear canal volume, peak static acoustic admittance, tympanogram peak pressure and tympanogram width. (Qian, 2019)

A popular qualitative classification system was presented by Lidén (1969) and Jerger (1970). In Figure 3.2, Type A indicates a normal tympanogram with a peak immittance at or near 0 daPa, indicating the normal air-filled middle-ear condition. Type A has subcategory A_S denoting a tympanogram with reduced amplitude, characteristic of some forms of otitis media or ossicular fixation. Type A_D refers to a tympanogram that has an unusually high peak. This type occurs in cases of abnormal TM or ossicles when a low probe frequency is used. Tympanograms of type B are flat and occur in the presence of effusions and other space-occupying lesions of the middle ear. A type B pattern will also be found in cases with TM perforation, impacted cerumen and when an immittance probe is inappropriately placed against the ear canal wall. Type C signifies peaks shifted towards the negative pressure, indicating static pressure in the middle-ear space, which is often caused by sinus congestion, ear infections, or Eustachian tube dysfunction. Type D has been described as showing 'sharp notching, characteristic of scarred eardrums or normal, hypermobile tympanic membranes' (Katz, 1978, p. 445). Type E has broad, smooth peaks and is most often seen in cases of partial or complete ossicular discontinuity. Tympanograms of types D and E are rarely observed with low probe frequencies (Katz, 1978; Shanks & Shohet, 2008, p. 9).

A combination of quantitative and qualitative measurements is used to characterize the tympanogram more precisely. Quantitative features include: peak compensated static acoustic

admittance (Y_{tm}) (mmho), the tympanogram height; equivalent external acoustic meatus volume (V_{ea}) (ml), the estimated air volume of the middle ear; tympanometric width (TW) (daPa), a measure of the shape of the tympanogram close to the peak; and tympanogram peak pressure (TPP) (daPa), the tympanogram peak location along the pressure axis. The diagnostic relevance of these numbers varies (Van Camp et al., 1986; Vanhuyse et al., 1975). Tympanometry can also be examined in terms of admittance quantities which, as mentioned above, include: conductance (G, the real part), susceptance (B, the imaginary part), admittance magnitude (Y) and the admittance phase angle (φ). Admittance tympanograms may exhibit patterns with additional properties that can be used to identify particular middle-ear diseases (e.g., Vanhuyse et al., 1975; Van Camp et al., 1986).

3.2.4 Clinical applications of tympanometry

The following information is mainly based on Van Camp et al. (1986), Lilly (1984) and Iacovou et al. (2013).

Measurements of immittance were first made clinically available in the 1940s and became common in the 1970s. In the early days of tympanometry, measurements of middle-ear impedance were only qualitative or semi-quantitative. Tympanometers lacked control components to generate constant sound pressure levels. Tympanometry became widely used as a routine clinical practice in the audiological assessment of older children and adults once further quantitative measures were introduced to tympanometers.

The earliest generation of acoustic-immittance instruments used a single low-frequency probe tone of 220 Hz and measured only the magnitude of the acoustic immittance. Probe-tone frequencies of 220 or 226 Hz were initially chosen for a number of reasons. Firstly, calibration was easy since a volume of 1 cm^3 has a 1-milliohm impedance value at the frequency of 226 Hz. Secondly, transducers in that era only worked well with low frequencies, becoming non-linear at high frequencies. Thirdly, since the phase angle is nearly constant at low frequencies and does not need to be considered, they could use a single-component admittance method. Fourthly, the level of the probe signal was high enough for the immittance measurement but did not activate the acoustic stapedial reflex. Additionally, 220 Hz was not a harmonic of the 50-Hz European power-line frequency (e.g., Lilly, 1984; Van Camp et al., 1986; Iacovou et al., 2013).

In 1970 the Grason Stadler company presented a new instrument with two probe-tone frequencies, 220 Hz and 660 Hz, as well as two admittance components, conductance and susceptance (e.g., Shanks & Shohet, 2008). This instrument was used by Feldman (1976) to collect 220 and 660-Hz tympanograms from ears with different middle-ear pathologies, and showed the obvious advantages of evaluating mass-related middle-ear pathologies using the high-frequency probe tone (e.g., Shahnaz et al., 2008; Shanks & Shohet, 2008). The frequency range was later extended to around 2 kHz by (1) keeping the frequency of the probe-tone constant while quasi-statically sweeping the pressure inside the ear canal (e.g., Colletti, 1975); or (2) maintaining the pressure inside the ear canal constant while sweeping the frequency (e.g., Funasaka et al., 1984; Wada & Kobayashi, 1990). Current practice involves quasi-statically sweeping ear-canal pressure while applying wideband stimuli (up to 8 kHz) that can be either clicks or chirps (e.g., Keefe & Simmons, 2003; Sanford & Feeney, 2008). During the pressurization cycle the sound stimulus is repeated (e.g., every 40 ms). Since the quasi-static pressure changes are very small during the duration of the acoustic stimulus (e.g., 0.48 daPa for a pressure change of –400 to +200 daPa at a rate of 50 daPa/s as in Therkildsen & Gaihede (2005), it is assumed that the pressure is constant during each of these stimuli. It has been shown that the use of multi-frequency tympanometry improves the test's sensitivity for some outer and middle ear diseases (e.g., Shahnaz et al., 2008). These findings have not yet led to the implementation of routine high-frequency tympanometry.

Wideband measurements provide information on how the components of admittance change with the pressure and with the stimulus frequency. The resonance frequency of the middle ear changes when the effective mass and stiffness of the system change, and can, therefore, serve as one middle-ear status indicator in the tympanogram. The middle ear can be considered as a system consisting of mechanical masses, dampers and springs. At low frequencies it is stiffness-dominated while at high frequencies it is mass-dominated. At mid to high frequencies, damping plays an important role in the middle ear. For instance, otosclerosis, in which ossicular vibration is reduced due to abnormal growth of bone in the middle ear (e.g., Colletti et al., 1993; Van Camp & Vogeleer, 1986), and rheumatoid arthritis, which is an autoimmune and inflammatory disease (e.g., Giannini et al., 1997), increase middle-ear stiffness and consequently increase the resonance frequency of the middle ear. On the other hand, an ossicular-chain disruption results in

a decrease in the stiffness of the middle ear and consequently a decrease in the middle-ear resonance frequency.

At low frequencies, such as below 2 kHz, the distribution of the acoustic pressure is almost uniform along the ear canal and across the TM, and the admittances of the canal and the TM can be added. The interaction between the admittances becomes more complex at higher frequencies and the tympanogram becomes more difficult to interpret. This is why multi-frequency and wideband stimuli are not used as frequently as 226-Hz probe tones in clinical settings.

3.2.5 Tympanometry in newborns

Hearing loss is one of the most prevalent congenital disabilities. Untreated hearing loss can result in impaired language, cognition and social skills. The importance of early detection, along with appropriate early intervention, cannot be overstated. As mentioned above, a newborn's hearing is often screened with an OAE test, which evaluates the cochlear response to sound. The proper operation of the outer hair cells is indicated by the production of very faint sounds in response to the stimulus. Since the middle ear transmits the sound stimuli to the cochlea, OAE test results also reflect the condition of the middle ear. An ABR test is also often used in newborn hearing screening. ABR results reveal information regarding the operation of the middle ear, the cochlea, and the auditory pathways within the brainstem. Tympanometry measurements results are believed to help in the interpretation of ABR and OAE results (e.g., McKinley et al., 1997), and it has been suggested that immittance measurements be included in a battery of screening tests to find any problems in a newborn's hearing (e.g., McKinley et al., 1997; Shahnaz et al., 2008). However, studies have shown that 226-Hz tympanometry tests performed on infants under the age of six months are not as reliable as those performed on adults (Holte et al., 1990; Park, 2017). For adults, low-frequency tympanometry at a single probe tone presents easy-to-interpret results, but for newborns the results are quite different. For example, there is a possibility of obtaining abnormal-looking low-frequency pure-tone tympanograms in normal infant ears (McLellan & Webb, 1957), and infants with confirmed middle ear effusion can have a normal 226-Hz tympanogram (Meyer et al., 1997). These differences may be explained by the differences in the anatomy between adults and infants, as discussed in Section 2.3.

3.3 Experimental measurements

3.3.1 Introduction

Over the years, many experimental techniques have been used to study the mechanics of the middle ear both *in vivo* and *post mortem*. This section provides a review of relevant previous experimental measurements. Measurements of vibration in the presence of quasi-static pressures (e.g., Decraemer et al., 1984; Feldman et al., 1984; Kobayashi et al., 1985; Shanks & Wilson, 1986; Gaihede, 1996; Lee & Rosowski, 2001; J. J. Dirckx & Decraemer, 2001a; Therkildsen & Gaihede, 2005; Kose et al., 2020, 2022) are omitted because this thesis focuses on the modelling of unpressurized vibrations. Measurements of acoustic input admittance (e.g., Ravicz et al., 1992; Ravicz & Rosowski, 1997; Teoh et al., 1997) are also omitted. Even though admittance measurement can be done easily, it does not offer information related to the spatial patterns of TM vibrations, which are very important factors in understanding the mechanics of the middle ear.

Sections 3.3.2 and 3.3.3 review measurements of non-gerbil and gerbil TM vibrations, respectively. Section 3.3.4 reviews measurements of material properties of the middle-ear soft tissues.

3.3.2 Non-gerbil tympanic-membrane vibrations

Funnell and Laszlo (1982) published a review on measurements of TM vibrations. In this section, some of the more notable older studies are included and then more recent studies are mentioned.

TM vibrations were assessed with a magnifying glass, a mirror, and mechanical probes in the early studies. Von Békésy (1941) measured TM vibration with a capacitive probe. At low frequencies (up to 2 kHz), the TM movement was reported as a rotation of a stiff surface around an axis superior to the TM. It was concluded that due to this rotation the maximum magnitude of vibration takes place in a position inferior to the manubrium. The first observations of the vibration pattern of TM by the use of time-averaged laser holography (at frequencies up to 6 kHz) were made by Tonndorf and Khanna (1972) and Khanna and Tonndorf (1972). TM vibration patterns were described by iso-amplitude contours. According to their findings, even at

low frequencies the TM does not move as a stiff surface as described by von Békésy (1941). The maximum displacement was observed in the posterior PT for both cat and cadaveric human ears. They observed simple spatial patterns up to approximately 2 kHz, while for higher frequencies the vibration patterns became more complicated. Wada et al. (2002) studied TM vibrations of the guinea pig up to 4 kHz using interferometry based on time-averaged speckle patterns. A sinusoidal phase modulation method was used to observe the small motion amplitudes as well as their phases. The observed vibration patterns were similar to those observed by Khanna and Tonndorf (1972).

While the above-mentioned methods of time-averaged holographic and speckle-pattern measurements provide full-field observations of the motion of the TM surface under the sound stimuli, point-by-point laser interferometry offers more accurate magnitude and phase measurement of the motion of the TM surface. Tonndorf and Khanna (1968) designed and constructed a laser interferometer for observing the TM vibration of the cat at the umbo. Konrádsson et al. (1987) investigated the vibrational movement of *in vitro* human specimens of the TM using computerized LDV. In their study, three approaches (a three-dimensional scan of the entire vibrating TM, horizontal sweeps, and point measurements) showed the versatility of the method for measuring vibrating TM velocity. Decraemer et al. (1989) measured the amplitude and phase of the TM as well as malleus vibrations using a homodyne interferometer over a wide frequency range of 130 to 20 kHz. The results for malleus vibration measurements at different points along its length suggested that at high frequencies its mode of vibration changes and is no longer mainly rotational. Up to a frequency of 1 kHz, all points on the TM were vibrating in the same phase as the malleus. For frequencies beyond 5 kHz, discrete resonances could be seen and the response changed greatly with the location on the TM.

Rosowski et al. (2009) investigated TM vibrations up to 20 kHz in three mammalian species (human, cat, and chinchilla) using an optoelectronic holography interferometer system. This method enables quick measurements of the TM surface's motion magnitude at frequencies as high as 25 kHz. For frequencies above 0.8 kHz in the chinchilla specimen, and frequencies above 2 kHz in humans and cats, highly complicated vibration patterns were observed. Moreover, they found ring-like patterns at frequencies above 1 kHz for chinchilla TM and saw the same pattern in humans and cats for frequencies above 4 kHz. In line with prior estimates in the literature,

they also calculated TM surface wave speeds that ranged from 20 to 65 m/s depending on frequency and species. In a subsequent study conducted by the same group (J. T. Cheng et al., 2010), stroboscopic holographic interferometry was used to determine the phase and amplitude at each of about 40,000 points on the TM surface. The measurement was conducted with frequencies of 0.5, 1, 4 and 8 kHz. They concluded that the amplitude and phase maps obtained at high frequencies cannot be described by the motion of a single wave, but are consistent with a mixture of small travelling-wave-like components, as well as low and higher order modal motions.

3.3.3 Gerbil tympanic-membrane vibrations

The middle ear of the gerbil has been the subject of numerous experimental studies but only a very limited number of studies have examined how the gerbil TM vibrates in response to sound pressure. De La Rochefoucauld and Olson (2010) evaluated the gerbils' TM vibration pattern at some points near the umbo on the PT and along the manubrium. Apart from those measurements, our group is the only one to have published studies on gerbil TM vibrations. Ellaham et al. (2007) conducted *post mortem* LDV measurements at several points on the gerbil TM over a frequency range of 0.15 to 10 kHz. The results showed that drying of middle-ear structures greatly affected vibration measurements. The *post mortem* studies performed by Nambiar (2010) were similar to those performed by Ellaham et al. (2007) but included much better hydration of middle-ear structures in order to prevent *post mortem* effects from drying. He (2010) reported results with a more widely exposed TM and thus with measurement locations further away from the manubrium. Maftoon et al. (2013) presented the *in vivo* spatial vibration pattern of the gerbil TM with closed middle-ear cavities employing the same method of LDV measurements at multiple points. Motions on the TM were measured in response to audio-frequency chirps (fast frequency sweeps). They reported data for two PF conditions, naturally flat and retracted into the middle-ear cavity. At low frequencies, a flat PF resonance makes a shallow maximum and minimum in the manubrium and PT displacement magnitudes. The displacement magnitude of the retracted PF is much smaller and has no impact on the other points' responses. At low frequencies the posterior side of the PT typically exhibited larger displacements than the anterior side. At higher frequencies the simple vibration pattern of the PT became more complicated, with the breakup happening between 1.8 and 2.8 kHz. They also reported that all points on the

manubrium and PT showed a wide resonance between 1.6 and 2 kHz. The magnitudes of displacement at manubrial points, including the umbo, rolled off with considerable irregularity above this resonance. A gradual increase in the displacement magnitudes of the manubrial points was seen from the lateral process to the umbo. Maftoon et al. (2014) reported results with up to five different extents of opening the middle-ear cavity. Opening the cavity shifted the PT primary middle-ear resonance to lower frequencies and increased the low-frequency magnitude as well as introducing an antiresonance for all of the manubrial, PT and PF responses. Opening the cavity has little or no impact on either the manubrium's mode of vibration or the PT's breakup frequency. The antiresonance frequency shifts to higher frequencies as the opening was gradually widened. An identification technique was proposed for removing the impact of the antiresonance.

3.3.4 Material properties of the middle-ear soft tissues

The TM is a complex structure with a non-uniform thickness and comprises many layers of tissue. This section discusses *in vitro* measurements of the TM's mechanical properties. Békésy (1960) used a bending test on a rectangular strip of human TM and reported a Young's modulus of 20 MPa. Based on longitudinal dynamic tests on strips of fresh human TM, Kirikae (1960) measured the Young's modulus to be 40 MPa. Later, Decraemer et al. (1980) conducted a uniaxial tension test on human TM strips and obtained a Young's modulus of 23 MPa.

Fay et al. (2005) assessed the TM Young's modulus of cat and human through composite laminate theory in dynamic measurements. They concluded that the presence of collagen fibres accounts for the majority of the stiffness in the TM, and that the stiffness in specific regions of the TM depends on the local fibre density. They reported a range of 0.1 to 0.3 GPa for the Young's modulus of human TM and 0.1 to 0.4 GPa for the cat TM. The values were far higher than those from earlier studies because they utilized a considerably thinner TM thickness that represented only the fibre layers.

As mentioned earlier, the TM structure is anisotropic and inhomogeneous, while the TM modulus was presumed to be uniform over the area and thickness of the samples in the experiments mentioned above. Huang et al. (2008), on the other hand, used a nanoindentation method to assess the local properties and mapped them over the whole surface. They measured the linear in-plane and out-of-plane viscoelastic characteristics of the human TM for very small

strain rates. The shear relaxation modulus was presented in terms of a generalized Maxwell model. In the through-thickness direction three time constants (1 s,10 s and 100 s) were determined; for the in-plane direction, two time constants (10 s and 100 s) were sufficient. The through-thickness Young's modulus was reported to be between 6.2 and 6.8 MPa, while the in-plane Young's modulus was estimated to be between 17.4 and 19 MPa. The in-plane Young's moduli were similar to those measured when tensile and bending tests were used by other groups for assessing the TM mechanical properties and characterizing the TM modulus over a portion of the TM as averaged values. Later the same method was used by Daphalapurker et al. (2009) to measure Young's moduli of the human TM in four quadrants. Young's modulus values of 25.7 to 37.8 and 2 to 15 MPa were obtained for in-plane and out-of-plane directions, respectively. These in-plane values were again close to the values obtained by other groups.

The human ear responds to pressure waves in the auditory frequency range of 20 to 20,000 Hz, so it is essential to measure the characteristics of the TM at high strain rates. Luo et al. (2009a) developed a novel small-scale split Hopkinson tension bar to examine the mechanical behaviour of human TM under a high strain rate of 300 to 2000 s^{-1}. The Young's modulus value for normal human TM was found to be 5.2 to 58.9 MPa in the radial direction and 34.1 to 56.8 MPa in the circumferential direction over the range of strain rates. They concluded that there is a strong dependency of the Young's modulus on strain rate at these elevated strain rates. Luo et al. (2009b) used the same method to measure the Young's moduli of human TM's that were thickened due to disease (or abnormality) as 33.1 to 42.8 MPa in the circumferential direction and 63.4 to 79.2 MPa in the radial direction at the same high strain rates. The dependence on strain rate was less than in normal human TM's. Zhang and Gan (2010) used a laser Doppler vibrometer to perform dynamic tests on human TM up to 8000 Hz and FE models were used to fit the experimental measurements to obtain the complex modulus. In this study, the frequency-domain complex modulus and the time-domain relaxation modulus were computed. In eight TM specimens, the mean storage modulus was 54.34 MPa at 200 Hz and 65.54 MPa at 8,000 Hz, while the mean loss modulus was 1.92 MPa at 200 Hz and 6.12 MPa at 8,000 Hz.

Later Zhang and Gan (2013) developed a new method to measure the dynamic characteristics of human TM using a Dynamic Mechanical Analyzer at three different temperatures, 5, 25 and 37 C. The test was performed over a frequency range of 1 to 40 Hz for 11 specimens and

frequency-temperature superposition was applied to extend the frequency range. The mean loss modulus was reported as 0.28 MPa at 1 Hz and 4.1 MPa at 3800 Hz while the mean storage modulus was reported as 15.1 MPa at 1 Hz and 27.6 MPa at 3800 Hz. Their results show that both the storage and loss moduli increased when the temperature decreased and when the frequency increased. They also found that at the lower frequencies the loss modulus had larger slopes.

Luo et al. (2019) measured the spatial distribution of the out-of-plane Young's modulus of human cadaver TM's with a microindentation method using a viscoelastic contact analysis. Their results showed that the lateral and medial surfaces exhibited different spatial distributions of Young's modulus.

Since Lim (1968) described the human PF as an extension of the ear canal skin, the Young's modulus of skin can be used to estimate the Young's modulus of PF. Agache et al. (1980) measured the mechanical characteristics of the *in vivo* dermis in human by applying a torque on the skin and measured the resultant deformation. By applying torque, they measured both instantaneous and delayed viscoelastic deformations and relaxation. The measured values were adjusted based on the constant thickness of the skin. They reported that human forearm skin has an average Young's modulus of 0.42 MPa for subjects aged less than 30 years and 0.85 MPa for older subjects. Their experimental results showed that elasticity decreased after the age of 30, related to an increase in visco-elastic components.

Using a micro-material testing system, Gan's group reported the mechanical properties of various middle-ear soft tissues (T. Cheng & Gan, 2007, 2008a, 2008b; Gan et al., 2011; Zhang & Gan, 2011). For example, Cheng and Gan (2008b) used uniaxial tensile, stress-relaxation and failure tests to measure the mechanical properties of the AML, and described the non-linear behaviour of the AML using a non-linear hyperelastic model.

3.4 Viscoelastic material models

Some materials can both dissipate and store energy. These materials have both viscous and elastic properties and are referred to as viscoelastic materials. The term "elastic" indicates that when the deforming force is removed, the material will return to its original configuration. "Viscous" implies that when the deforming force is removed, the material will stop deforming

but not return to its original configuration. The deformation is accompanied by a permanent rearrangement of molecules.

The following overview of viscoelastic materials is mostly based on the textbooks by Christensen (1982) and Belytschko et al. (2000).

Viscoelastic materials have three main characteristics: creep, stress relaxation, and hysteresis. Figure 3.4a shows the creep phenomenon, which is the continuation of the deformation of a viscoelastic material after the load has reached a constant value, while stress relaxation (Figure 3.4b) is the continued decrease in stress inside the material under a constant deformation. The differences between loading and unloading curves for a viscoelastic material, and the corresponding energy dissipation, are referred to as hysteresis. A hysteresis loop is shown in Figure 3.4c.

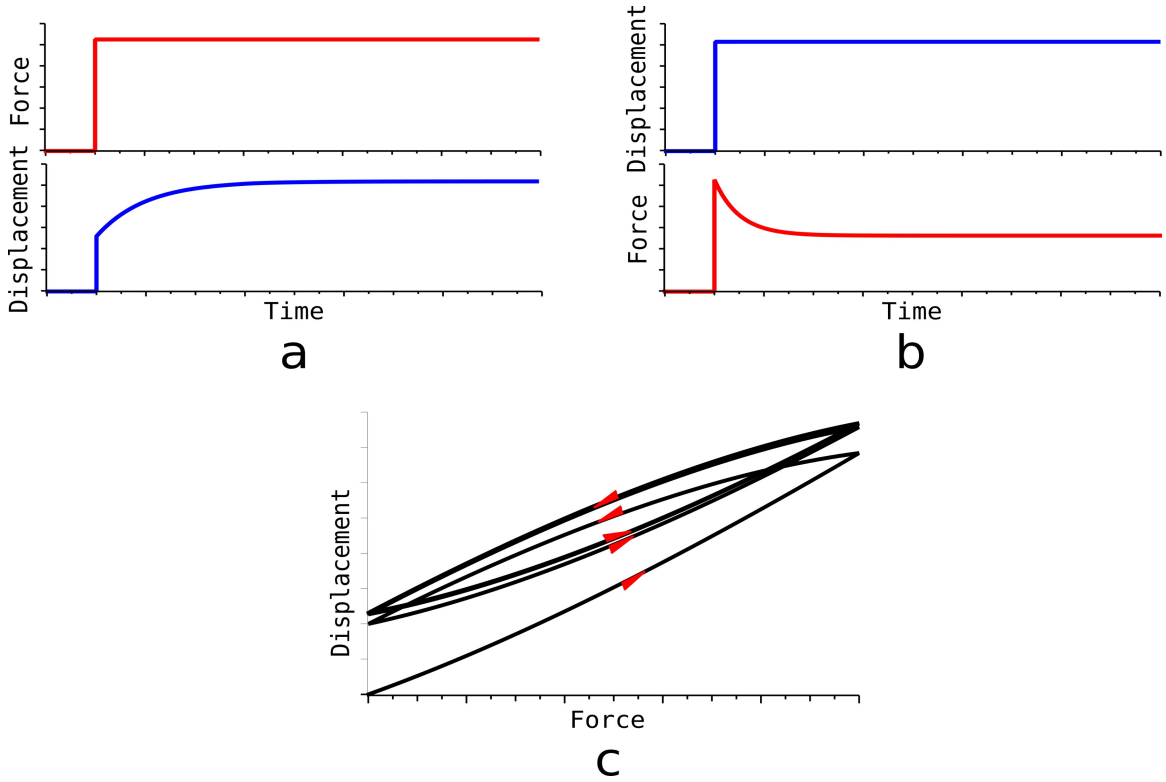

Figure 3.4:Three main characteristics of viscoelastic material. (a) Creep. (b) Stress relaxation. (c) Hysteresis.

All of the behaviours described above can be modelled by a 'standard linear solid' (SLS) model consisting of two springs and a dashpot. The SLS model can be generalized by putting several of them in parallel (Figure 3.5). This generalized SLS model, also known as a generalized Maxwell model, results in a more accurate viscoelastic response. It also increases the number of model parameters and subsequently increases the model complexity.

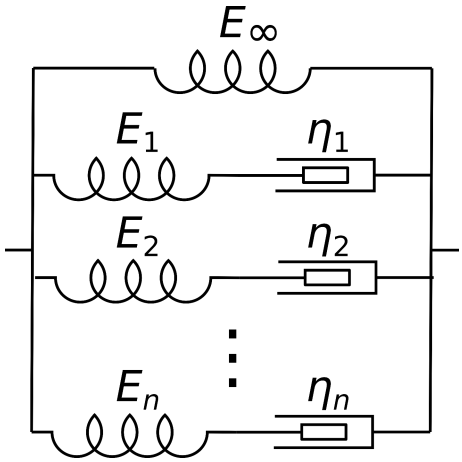

Figure 3.5: Generalized SLS model, or generalized Maxwell model, with n *series dashpot-and-spring branches in a parallel arrangement*

The elastic moduli of the free spring and of the i-th spring element are E_∞ and E_i, respectively, and the viscous coefficient of the i-th dashpot element is given by η_i. The stress and strain in each branch of the generalized Maxwell model can be written as follows:

$$\frac{\partial \varepsilon_i}{\partial t}=\frac{1}{E_i}\frac{\partial \sigma_i}{\partial t}+\frac{\sigma_i}{\eta_i}. \tag{3-4}$$

Considering σ as the total stress and ε as the external strain applied on the whole model, the equations below can be written:

$$\varepsilon=\varepsilon_\infty=\varepsilon_i \tag{3-5}$$

and

$$\sigma=\sigma_\infty+\sum_{i=1}^{n}\sigma_i. \tag{3-6}$$

ε_∞ and σ_∞ stand for the strain and stress of the free spring, respectively.

A viscoelastic material response can be represented as a convolution of an elastic component and a time-dependent component. The total second Piola–Kirchhoff stress tensor $S(t)$ is calculated by convolving a normalized relaxation function $G(t)$ with the derivative of the response of an elastic function S^e as follows:

$$S(t)=\int_0^t G(t-u)\left(\frac{dS^e}{du}\right)du \tag{3-7}$$

where t is time and u is a dummy variable.

The $G(t)$ for the generalized Maxwell model is described by a Prony series which corresponds to the set of N Maxwell elements in parallel. When S^e represents the instantaneous elastic response, $G(t)$ is calculated using equation (3-10), while equation (3-11) is used to calculate $G(t)$ when S^e represents the long-term elastic response:

$$G(t)=1-\sum_{i=1}^{N} g_i\left(1-\exp\left(-t/\tau_i\right)\right) \tag{3-8}$$

$$G(t)=1+\sum_{i=1}^{N} g_i \exp(-t/\tau_i) \tag{3-9}$$

In equations (3-10) and (3-11), the g_i are the relaxation coefficients and the τ_i are the time constants, which are material parameters. N represent the number of exponential terms. FEBio solves the simulations based on equation (3-11).

3.5 Finite-element modelling

3.5.1 Introduction

The brief overview of the finite-element (FE) method in this section is mostly based on Zienkiewicz et al. (2013) and Funnell et al. (2021).

Computational models can summarize what is known about a system and provide a better understanding of its behaviour. They can also be used for prediction and control once they have been validated to some extent. Partial differential equations are used in engineering sciences to describe physical systems. Currently, one of the most often used techniques for solving these equations is the FE method. Nearly all problems encountered in practice, such as steady-state or transient problems in the linear and non-linear region for one, two, and three-dimensional domains, may be solved using the FE method.

The physical system under investigation, which is typically complex and challenging to solve mathematically, is separated into simple and finite components, known as elements, in the FE method. Elements have simple geometrical shapes, including triangles, quadrilaterals, tetrahedra, and hexahedra, whose behaviour can be described by simple equations which can be easily solved. Combining these element responses can yield the complex behaviour of an overall system. In general, the FE method consists of three steps:

- Pre-processing: In this step, the geometry of the system is reconstructed, then by generating the appropriate mesh, the system is discretized into elements. The material properties, boundary conditions and load on each element complete the mathematical formulation for the model.
- Processing: At this stage, mathematical formulations (governing equations) are solved.

- Post-processing: This stage involves assessing and validating the results.

In order to show how the FE method can be applied in different fields, we will consider using it in a continuum mechanical system. To begin with, we need the geometry of the structure. For biomedical modelling, the geometry is usually reconstructed using a set of images like computed tomography (CT). The images are segmented in order to create the geometry, which is discretized into a mesh. Based on the interaction between the components of the system, the governing equations are chosen for each element. Following that, all of these equations for all elements are combined in matrices of coefficients (related to geometry and material properties) and variables (time and spatial coordinates).

In FE modelling of a mechanical system, a force-displacement relationship is described for each element and analyzed based on the responses at discrete nodes. The force-displacement relationship is formulated as follows for a linear static problem:

$$Ku = f \tag{3-10}$$

where K is the stiffness matrix of the element, u is the vector of the nodal displacement and f is the applied nodal force vector. The unknown displacements are obtained by solving this equation.

The equation for a linear dynamic problem is

$$M\ddot{u} + C\dot{u} + Ku = f(t) \tag{3-11}$$

where M and C are the mass and damping matrices, respectively.

To ensure an adequate and accurate representation of reality, a number of factors must be carefully considered.

1. Mesh resolution: The accuracy of a FE simulation relies on the mesh resolution. Mesh convergence analysis is very important in the FE method to investigate how many elements should be used in the model. Fine meshes result in larger equation systems that require more computation, while coarse meshes may not produce accurate results. Therefore, choosing an appropriate mesh resolution and the scheme for integration of the elements for a specific FE

model is a trade-off between (1) the model complexity and the runtime of the simulation, and (2) the accuracy required for the actual application of the model.

2. Constitutive laws: The way a material should be modelled depends on the nature of its deformations, and it is important to select the appropriate material properties. In general, *a priori* knowledge of material properties is preferred over adjusting the parameters of the model in order to fit a set of experimental data.

3. Boundary, loading and constraint conditions: In general, systems have interactions within themselves (i.e., between the system components) and with the environment (i.e., input load and the boundaries of the system). Successful FE models should simplify those conditions while maintaining an accurate depiction of reality.

5. Model verification and validation: The process of model verification involves checking the computer code and the mathematical calculations. Model validation is the process in which the results obtained by different simulations of that model are compared with experimental measurements or other models' results.

3.5.2 Finite-element software

Numerous software packages are available for FE modelling, both commercial and open-source. Three examples of commercial software that are commonly used are ANSYS (www.ansys.com), COMSOL (www.comsol.com) and Abaqus (https://www.3ds.com/products-services/simulia/). Free (libre) and open-source software is also available in this field, such as Salome-Meca (https://www.code-aster.org/V2/spip.php?rubrique2) (Antonutti et al., 2018) and FEBio Studio (https://febio.org/). FE software may include pre-processing, processing and post-processing all in one product.

3.6 Finite-element models of the ear

Zwislock (1957) published the first quantitative lumped circuit models of the middle ear, in which middle-ear components were represented by electrical circuit elements, with capacitance equivalent to compliance, inductance equivalent to inertia, and electrical resistance equivalent to mechanical or acoustic resistance (i.e., damping). Lumped-parameter models do not take spatial extent into account and are not well suited for dealing with spatial patterns of pressures and

displacements (Funnell et al., 2021). To address this issue, an analytical model by Wada & Kobayashi (1990) and a semi-analytical model by Rabbitt & Holmes (1986) were developed. Such models do not accurately portray the complex 3D nature of the middle ear, which is comprised of several interconnected, highly irregular, asymmetrical, and non-uniform components. By contrast, the FE method is capable of modelling such complicated systems and obtaining quantitative insight into how they work. In this method, the dependent variables are a function of both space and time and the model parameters can be linked directly to the physiological properties of the middle-ear components. The following review is limited to a brief overview of previous FE middle-ear models. For a more comprehensive review, refer to Funnell et al. (2021).

Funnell and Laszlo (1978) developed the earliest finite-element model of the middle ear. The model for the cat was valid in the amplitude range of linear vibration and at frequencies below about 1 kHz. In this model, the TM thickness and stiffness played an important role. TM curvature was represented by circular arcs in the absence of quantitative shape data, and a fixed axis of rotation running from the anterior mallear process to the posterior incudal process was assumed. Vibration patterns and amplitudes obtained using this model were similar to those observed experimentally with laser holography. Funnell (1983) extended the previous model to higher frequencies. The undamped natural frequencies and corresponding modal vibrations of the TM were investigated. A damping effect was added to the TM model by Funnell et al. (1987). The damping was represented by both stiffness- and mass-proportional terms using Rayleigh damping. In the presence of light damping the points on the manubrium showed smoother behaviour in the frequency domain than the ones on the TM away from the manubrium, and different points on the TM displayed different amplitudes and phases from one another. As damping increased, frequency responses became smoother. Even when the damping was high enough to smooth out all but the greatest variations, the overall displacement magnitudes were not much reduced. The laser interferometric point measurements of the cat TM by Decraemer et al. (1989) agreed quite well with the results of Funnell et al. (1987).

The first three-dimensional FE model of the human middle ear was presented by Wada et al. (1992). The linear dynamic model included the TM and ossicles and matched well with the experimental results obtained by the time-averaged holography of Khanna & Tonndorf (1972) in

terms of vibration patterns at low frequencies below3 kHz. In this model a fixed axis of rotation was again assumed.

Ladak and Funnell (1996) modelled both a normal cat middle ear and a surgically repaired one. To an existing cat TM model, explicit representations of the footplate and cochlear load were added. The footplate was modelled as a thin plate with a thickened rim. Spring attachments along the footplate's perimeter were used to simulate the cochlear load. After validating the model for physiological levels of sound and frequencies below 1 kHz, the normal model was changed to reproduce the two types of middle-ear surgery employed to repair an ossicular chain that is discontinuous.

Since the TM's mechanical behaviour depends greatly on its shape, having a model with realistic geometry is important. To address this issue, a phase-shift moiré topography technique was used by Funnell and Decraemer (1996) to investigate the shape and deformation of the cat TM. The new measurements of shape were included in four individualized FE models and the effects of the variation between animals were investigated. The existence of hysteresis in the pressure-displacement response was also shown. Later Daniel et al. (2001) employed moiré shape measurements to define the shape of the human TM, and ossicles and ligaments were reconstructed using histological sections and high-resolution magnetic-resonance microscopy (MRM) data. Soon after, histological images were used by Sun et al. (2002) to reconstruct the TM, attached ligaments, ossicles, and muscle tendons. The predicted displacements of the stapes footplate were compared with measurements from fresh temporal bones taken with laser Doppler vibrometry (LDV). It was concluded that the final FE model was 'reasonable in predicting the ossicular mechanics of the human middle ear'.

Decraemer et al. (2003) employed data obtained from X-ray microscale computed tomography (microCT) imaging data to reconstruct the geometry of the TM and ossicles. A comparison was also made between the commercial X-ray CT apparatus and X-ray CT using synchrotron radiation, magnetic resonance microscopy, fluorescence optical sectioning, and physical serial sections (histology). Although the orientation and geometry of the TM can be easily seen using MRM and CT imaging techniques, the TM's exact thickness distribution cannot be measured. Kuypers et al. (2005, 2006) used confocal microscopy and Van der Jeught et al. (2013) used optical coherence tomography to assessed the full-field high-resolution distribution of thickness

of the TM in human and gerbil samples. In a study by Elkhouri et al. (2006), an accurate geometry of the gerbil middle ear was reconstructed using a combination of histological sections, microCT and MRM. Ferreira et al. (2014) reviewed image-segmentation techniques used for 3-D reconstruction of the ear in more detail.

Different constitutive models have been used in FE models of the middle ear. Linear isotropic elasticity is the simplest constitutive model and can only describe the middle ear's response to low pressures like acoustic stimuli within normal hearing ranges. Funnell et al. (1987) used the FE method to model the TM with a single layer of isotropic material. The TM has also been studied using multilayer and orthotropic elastic models (e.g., Gan et al., 2006; Tuck-Lee et al., 2008). Isotropic elastic properties have generally been used for the TM, joints and ossicles (e.g., Wada et al., 1992; Maftoon et al., 2015).

Some non-linear models have been developed for the middle ear. Ladak et al. (2006) developed the first nonlinear model for the TM, for the cat, and investigated the model response under large static pressures in the range of pressures employed in clinical tympanometry. The model response matched well with their previous experimental data obtained with phase-shift shadow moiré topography (Ladak et al., 2004). Qi et al. (2006a, 2008a) presented the first nonlinear FE model of a 22-day-old newborn ear canal and middle ear under high quasi-static pressures, up to ±3 kPa. To model the large deformations, a hyperelastic constitutive law was applied. Wang et al. (2007) developed a combined static and dynamic FE model for the human middle ear under different middle-ear pressures. The geometric nonlinearity and hyperelastic Mooney-Rivlin material model were combined. To calculate the material parameters of the soft tissue components of the middle ear, an empirical formula was developed based on a stress-dependent elastic modulus as a function of middle-ear pressure. The dynamic response of the model under sound pressures in the ear canal was estimated under different positive and negative middle-ear pressures. Homma et al. (2010) also modelled the effects of high static pressures by empirically changing the linear material properties for a range of pressures. Motallebzadeh et al. (2013) developed the first non-linear viscoelastic model for the TM. The material properties of this model were defined by a convolution integral consisting of a non-linear elastic part and an exponential time-dependent part, represented by an Ogden hyperelastic model and a Prony series, respectively. The simulation results were compared with previous experimental data of

Cheng et al. (2007) which included both loading and unloading curves (hysteresis) and relaxation curves.

Gariepy (2010) introduced a preliminary linear dynamic model of the newborn ear, based on the static models of Qi et al. (2006a, 2008a). The response of the model in terms of input immittance was computed for sound pressures at frequencies below 2 Hz. After validating the model with previous experimental data, the relative admittance of the middle ear and ear canal at various frequencies was assessed.

Motallebzadeh et al. (2017a) refined and revised the model of Gariepy (2010). They later simulated fluid-structure interactions in order to investigate the wideband admittance response for frequencies up to 10 kHz (Motallebzadeh et al., 2017b). In this study, sensitivity analyses were performed to determine the effects of measurement location, material parameters, and geometrical variability. The results provide a quantitative understanding of the ear canal and middle-ear resonances around 500 Hz and 1800 Hz respectively, as well as of higher-frequency resonances due to the middle-ear air cavity and the ear canal.

Choukir (2017) introduced the first model of the middle ear in response to an acoustic stimulus in the presence of large quasi-static pressures, for a gerbil middle ear. This was the first time that the conditions of tympanometry had been simulated. A rigid wedge was used to simplify the ossicles and a fixed axis of rotation was assumed. A Mooney-Rivlin hyperelastic model and a six-term Prony series was used. The responses of the gerbil middle ear were simulated for a 226-Hz pure tone and for a wideband chirp. Experimental data obtained by Dirckx et al. (2006) and Salih et al. (2016) from rabbits were compared to the model response.

Qian (2019) refined the model developed by Choukir (2017). A representation of the ISJ and its surrounding structures was added to the model and material properties of the components were obtained from previous studies. The model response was investigated under the combination of high quasi-static pressure and low amplitude sound pressures consisting of pure tones and low-frequency chirps. The model results were compared with data from the literature as well as with new laser vibrometry data for the pressurized middle ear of gerbils by Kose et al. (2016, 2017, 2020, 2022). The model showed many features observed in the experimental and clinical observations, such as hysteresis and asymmetry between positive and negative static pressure in the amplitude of vibration.

In early FE models the cochlear load was not included in the model explicitly. Its effect was incorporated into the properties of the TM and ossicles (Funnell et al., 1987; Ladak & Funnell, 1996). Koike et al. (2002) explicitly modelled the cochlear load in their FE middle-ear model based on various observations that cochlear impedance is mainly damping, representing the effects of the cochlea by a dashpot connected to the stapes footplate. Sun et al. (2002) used 49 spring-dashpot elements to model the effect of the cochlear load. Explicit cochlear fluid models have also been combined with FE middle-ear models (e.g., Gan et al., 2007; Kim et al., 2011; Motallebzadeh & Puria, 2021, 2022).

Shaho (2020) presented a static model of a 1-day-old middle ear and investigated the response of the model to low-amplitude static pressures (10 Pa). The material properties of this model were obtained from previous studies. Comparisons were made between the responses of the 1-day-old model and the existing 22-day-old model of Motallebzadeh (2017a, 2017b) based on displacement magnitudes and spatial patterns. A sensitivity analysis was conducted for mesh resolution and for the geometry of the TM. TM curvature is an important factor in determining the stiffness of the model. By using a range of large pressures, different TM shapes were generated and their results were compared.

In this study, the static model of the 1-day-old ear (Shaho, 2020) is extended to handle frequencies up to 10 kHz.

Chapter 4. Materials and methods

4.1 Introduction

Detailed information about our FE model and the methods we used to develop it are presented in this section. In Section 4.2, methods used for creating and modifying the middle-ear model are explained. In Section 4.3, the data sources, current model geometry, mesh patterns and their modifications as well as additional components are explained. The simulation hardware and software as well as some challenges are explained in Section 4.4. In Section 4.5, an algorithm for calculating the thickness and its use with our model are discussed. In Section 4.6, the rationale behind choosing the material properties of each model component is provided. In Section 4.7, the discrete elements representing the stapedial annular ligament and cochlear load are presented, along with the procedure for incorporating them into the model. The boundary conditions and input sound pressure are described in Section 4.8. In Section 4.9, the loading conditions and time-step analysis are presented. Finally the method for the parameter-sensitivity analysis is presented in Section 4.10.

4.2 Methods for creating the middle-ear model

To create a 3D reconstruction of the middle ear, four locally developed computer programs were used, including Fabrication d'imagerie extraordinaire (Fie), Tr3, Thrup'ny and Fad (Auditory Mechanics Laboratory, Department of BioMedical Engineering, McGill University, http://audilab.bme.mcgill.ca/sw/).

CT images of the middle ear were imported into Fie as the first step in the reconstruction process. To view the desired anatomical structures, each CT slice image was observed separately. Each structure (malleus, TM, etc.) was traced by connected nodes in the 2D plane of each CT image as shown in Figure 4.1. After segmenting the structures using Fie, 'joins' were defined to form complex connections among lines in different slices and 'caps' were defined to close the holes at the first and last slices of segmented structures. Smoothing algorithms were used to produce smooth surfaces. Additionally, there are many attributes associated with each

segmentation line, including mesh resolution and line colour, and attributes related to the simulation such as material type, thickness and boundary conditions.

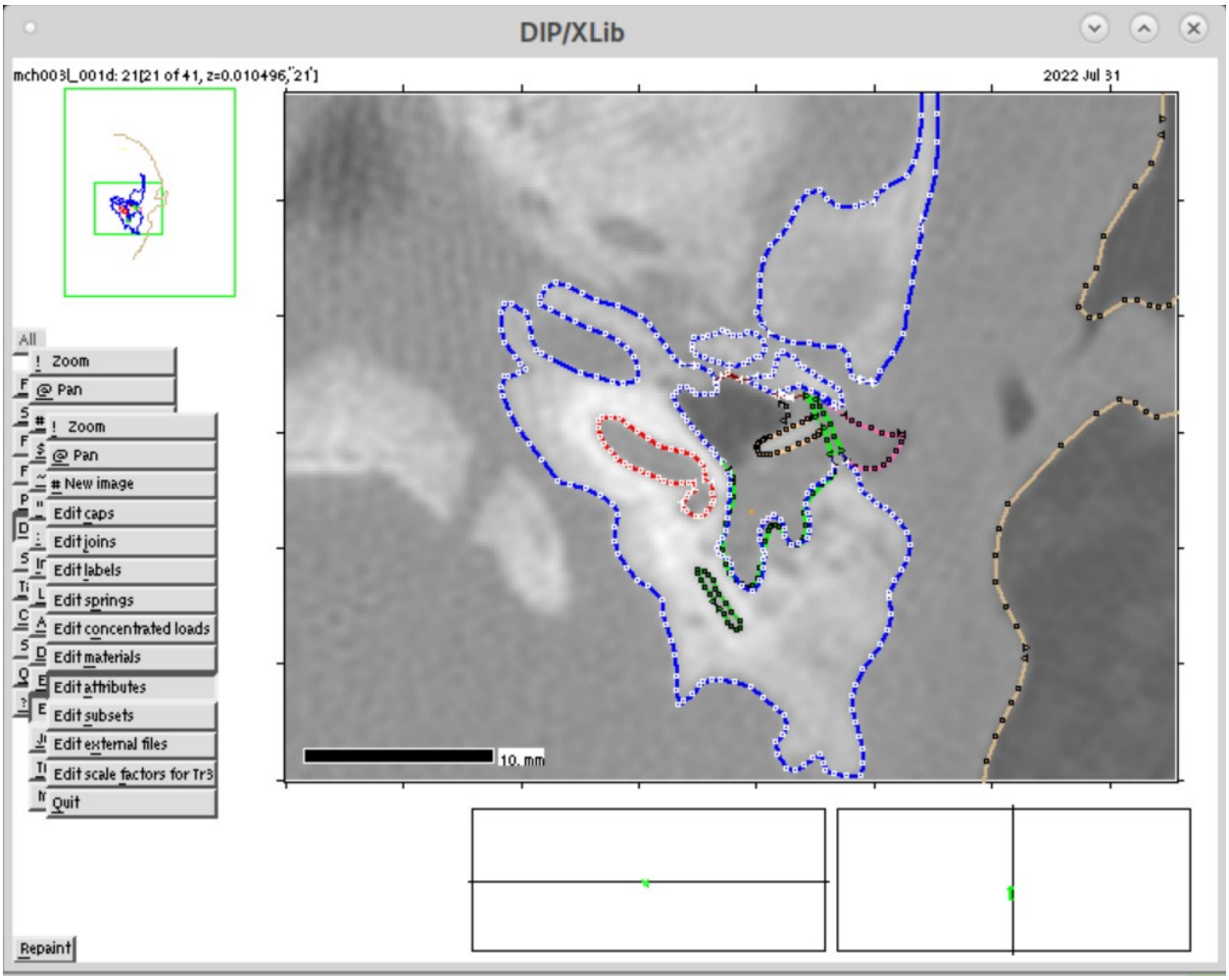

Figure 4.1: Fie (http://audilab.bme.mcgill.ca/sw/fie.html) graphical user interface used for segmentation of CT images.
One slice image of a 1-day-old CT scan is shown here. Each line represent a segmentation for one structure. For example, TM is green, malleus is beige, and ear canal is pink. The scale bar in the bottom left corner of the CT image shows a distance of 10 mm.

'Subsets' were defined to specify which lines should be included for a particular structure (e.g., the malleus or the incus). Many attributes such as material properties, boundary conditions, line colours and x-y resolution could be redefined in the subset definition for a structure.

After the segmentation process, Fie outputs a single '.tr3' file for the model, which is then imported into Tr3. Tr3 is used for connecting the contour lines of different slices with triangles in optimal ways. In other words, this software generates surface meshes from the segmented stack of 2-D images. It does this separately for each subset created in Fie. The Tr3 user interface is

shown in Figure 4.2. The triangulation process can be controlled by using different functions. Two functions were frequently used in this study: (1) toggling the alignment between lines in different slices; and (2) changing the cost function used to optimize the triangulation (Funnell, 1984).

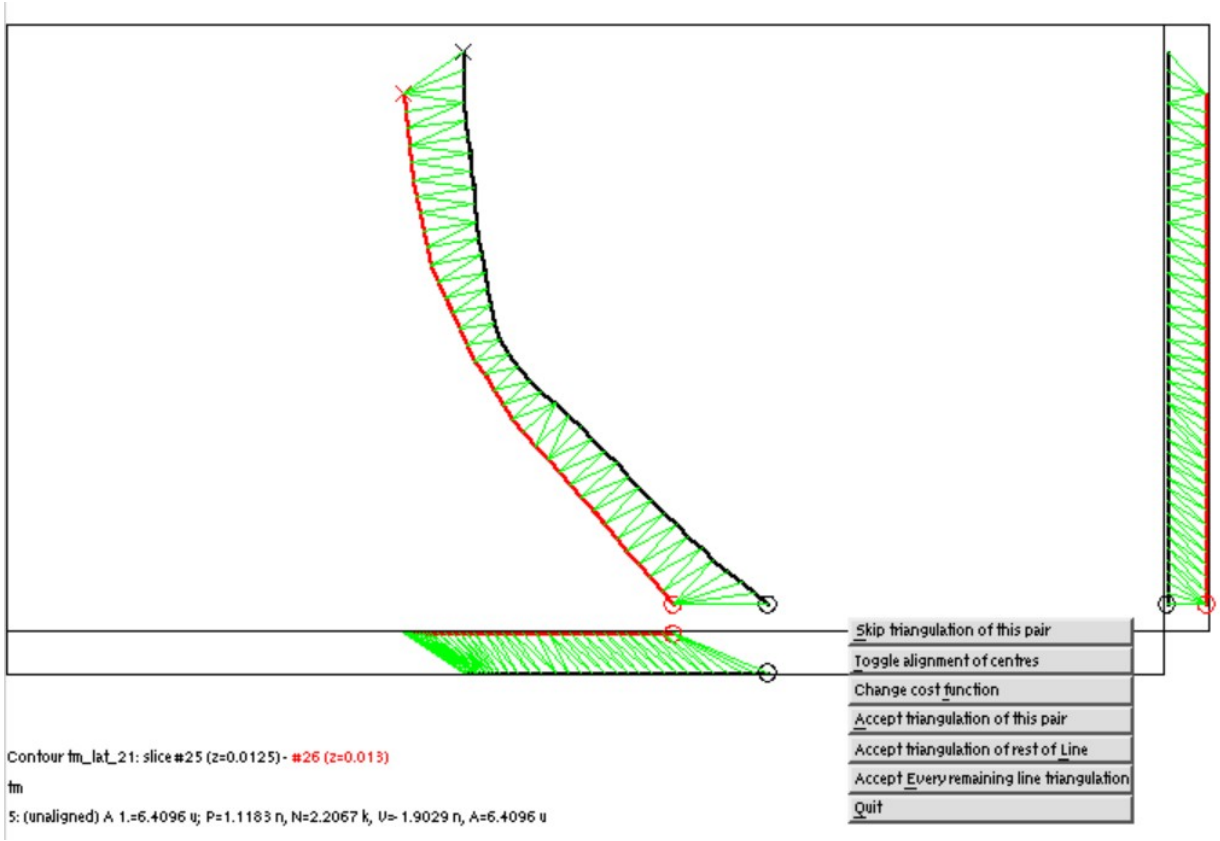

Figure 4.2: Example of triangulation between two lines in different slices by employing Tr3 (http://audilab.bme.mcgill.ca/sw/tr3.html) as a step in creating a 3D model. In this figure, segmented TM lines in two slices (black line in slice 25 and red line in slice 26) and the triangles (green) between them created by Tr3 are illustrated in the upper left panel. The panels below and on the right of the main panel show the side views of the two lines and the triangles. The menu includes the 'Toggle alignment' and 'Change cost function' operations, among others.

The 'Toggle alignment' control establishes whether Tr3 determines the optimal triangulation with or without a preliminary alignment of the two lines followed by a subsequent reversal of the alignment). For the 'Change cost function' control, Tr3 uses an algorithm to determine an optimal triangulation by minimizing one of several available 'cost' functions. Choosing one or another can change the quality of the triangulation. The 'Area' cost function minimizes surface area with no adjustable parameters. The 'Narrowness' cost function minimizes the sum of the

triangle narrowness parameters and has an exponent parameter. The 'Edge length' cost function minimizes the sum of the triangle edges' lengths with no adjustable parameter. The 'Partial volume' cost function, with no adjustable parameter, maximizes the portion of the volume between the lines that is dependent on the particular triangulation and is always positive (Cook et al., 1980). The 'Mixed' cost function balances the narrowness and partial-volume cost functions. Those two cost functions alone sometimes provide a poor quality triangulation, while employing a parameter in order to balance them may produce better results than using just one of them.

After doing the triangulation, Tr3 outputs a 'VRML' file and a 'Sap' file. The 'VRML' file was used for 3D visualization of the model in Thrup'ny, to observe the modifications made in Fie and Tr3 and to guide adjustment of the segmentation. Using Thrup'ny as part of an iterative process helps to improve the geometry. Figure 4.3 shows a visualization of the TM in Thrup'ny. The 'Sap' file is used for FE modelling and it contains the geometry, material properties and other characteristics needed for simulation. The 'SAP' file is imported to Fad for further processing. Fad is used to investigate various kinds of problems with the model as well as export the model in different formats. Among the important things which can be investigated with Fad are the numbers of reversed and superimposed triangles, problematic surfaces (e.g., ones that are supposed to be closed but are open), incorrect material boundaries, triangles having incorrect numbering, and high element aspect ratios within the model (i.e., elements with excessively thin

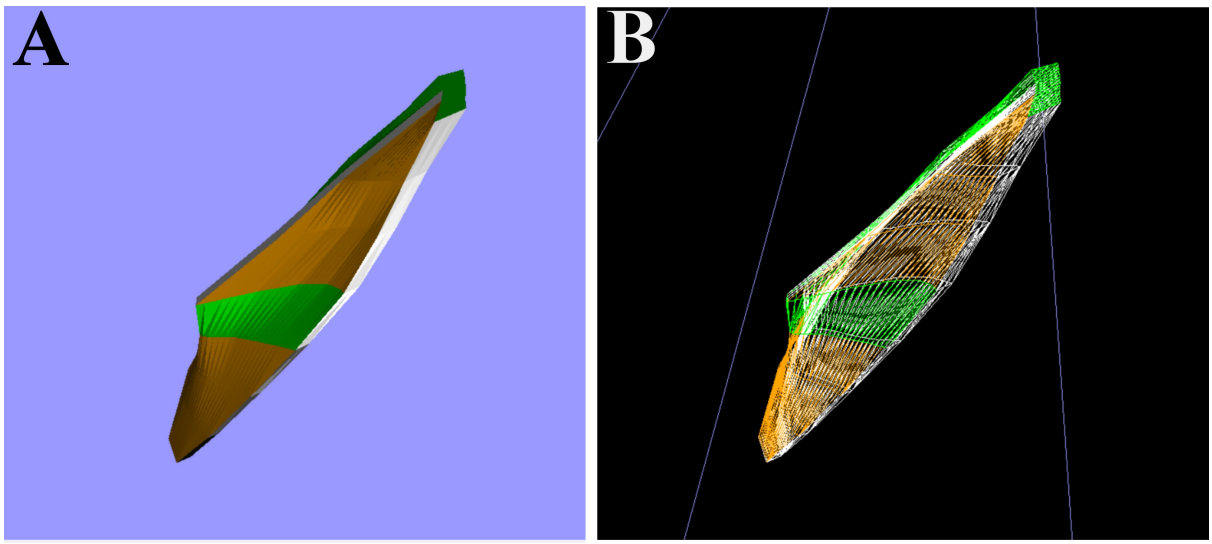

Figure 4.3: 3D visualization of the 1-day-old TM model in Thrup'ny (http://audilab.bme.mcgill.ca/sw/thrupny.html).
(A) TM as a shaded surface. (B) TM in the wireframe view, which is used to show the triangulated mesh structure.

and long shapes). Fad can also show other information related to the FE model, including the location of each node, numbers of elements, number of nodes, number of slices, etc.

The model was exported from Fad as a '.geo' file to be imported into Gmsh (https://gmsh.info/), an open source program that was used individually for each structure of the model to create a tetrahedral volume mesh from the triangulated surface mesh. Each structure was exported from Gmsh as a '.msh' file, which was then imported into Fad. In this process, Fad could retrieve boundary conditions, materials, etc. from the '.sap' surface file that Tr3 created. Each structure was exported from Fad as a'.sap' file, and then Fad was employed to join the individual tetrahedral structures one by one. The joining process was done by merging the recognized interface nodes of a shared surface, that is, a surface that appears in both structures with the same node coordinates and element definitions. (A node-to-node distance threshold value of zero was chosen in the joining process.) After joining the structures to obtain a completed model, the elements were changed from linear (first-order) to quadratic (second-order) using Fad. Higher-order elements are less rigid than first-order elements and provide better displacement predictions and convergence rates. Additionally, the shear-locking issue does not occur in higher-order elements as it does in linear elements (e.g., Dhondt, 2004).

The model was then rotated in the same way that the Shaho model was. The rotation was done so as to place the boundary of the TM approximately parallel to the XY plane. In this manner, the main displacement of the TM happened in the Z direction. In the final step, the model was exported as a '.feb' file for simulation in FEBio.

4.3 Current model components and modifications

The 3D geometry of the 1-day-old middle-ear model for a left ear is a refined and revised version of the geometry that Shaho (2020) presented.

The 3-D reconstruction of the 1-day-old middle ear was based on an X-ray CT scan which was obtained from the Montréal Children's Hospital (with ethics approval from the Institutional Review Board of the Faculty of Medicine & Health Sciences, McGill University). The middle ear was scanned with a pixel size of 0.1875×0.1875 mm. The slice thickness is 0.625 mm and the slice spacing is 0.5 mm. Figure 4.4A shows one slice of the CT scan, while Figure 4.4B schematically depicts the CT slices and their orientation.

The 3D geometry of the Shaho model includes the TM, including the PT and PF, as well as the malleus, incus, AML and PIL. The TM has an asymmetric shape with a nonuniform thickness. In this model the IMJ is assumed to be fused, so no motion exists between the malleus and incus. Some studies have shown that, at least up to 2 kHz, middle-ear sound transmission is relatively insensitive to fixation of the IMJ (Decraemer & Khanna, 2004a; Willi et al., 2002). This kind of simplification was used in the previous models developed in our group by Qi et al. (2008a) and Motallebzadeh et al. (2017a) for the 22-day-old ear as well as in the adult human model developed by Eiber (1999), among others.

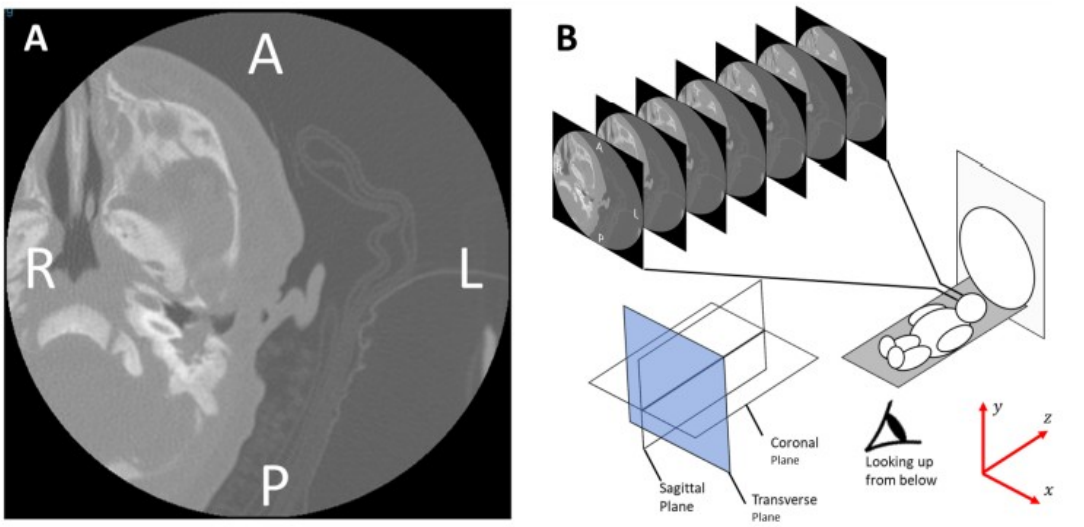

Figure 4.4: CT scan of the 1-day-old ear.
(A) One slice of the CT scan. (B) Illustration of a series of transverse CT images of a subject. A=anterior, P =posterior, R = right and L =left. (Shaho, 2020)

In the 1-day-old CT images, some structures cannot be well visualized due to the resolution of the CT images or the presence of amniotic fluid or mesenchyme. An example of these features is the orientation and thickness of the TM. The malleus could be identified in nine slices, while in two other slices identification of the malleus was challenging.

The low CT image resolution made it difficult to segment the stapes in the CT images for the 22-day-old ear of Motallebzadeh et al. (2017a), so the stapes was not included in their model. It was also difficult to segment the stapes in this study, for the same reason, so it was not included here either. Dirckx and Decraemer (2001b) found in an experimental study that the stapes has a minor effect on the deformation of the TM.

The PIL was sufficiently visible in two slices, but the AML was not distinguishable at all. Shaho (2020) used landmarks from histological images to segment the AML in the CT images. That segmentation was not changed in this study.

In this study, the previous segmentation of the long process of the incus was modified. In many slices, other parts of the segmentation were refined, and the sizes of various components of the model were adjusted based on the CT images. Malformed and problematic joins and caps were redefined. In addition, various parts of the model definitions (lines as well as joins and caps) were adjusted in order to avoid sharp angles in the geometry of the 1-day-old model. The attachment of the body of the incus to the long process of the incus was changed to a narrower configuration which caused the incus to have a more realistic shape. A change was also made in the shape of the head of the incus. Moreover, the shape of the IMJ was changed, and the incus and malleus attachments with their ligaments were altered.

In addition to the previously defined subsets for each structure, new subsets were defined to allow the inclusion or exclusion of lines from shared structures, to be able to examine them more precisely in Thrup'ny and then apply further changes as necessary. Moreover, additional subsets were defined for individual middle ear structures to allow better control over parameters like material properties, resolution, thickness, colour, etc. For some structures, the mesh pattern was modified using Tr3's cost-function and toggle-alignment features.

As discussed in Section 3.3.1, mesh resolution is very important in FE modelling. The mesh resolution can be defined in Fie for each line in two formats: (1) the resolution in the XY plane, which is measured in elements per diameter; and (2) the resolution in the Z direction, measured in slices. The convergence study by Shaho (2020) was conducted with quadratic elements on the TM (PT and PF) for the 1-day-old and 22-day-old models, as shown in Figure 4.5. Five different XY mesh resolutions (200, 300, 400, 500 and 600) were generated for both TM models. The boundary condition of the TM ring was clamped and a load of 10 Pa was applied on the lateral side of the TM in each model. His results showed that increasing the mesh resolution caused the displacement results to increase, as expected. The 1-day-old model displacement results showed a plateau at around 1.4 μm at a mesh resolution of 600, while in the 22-day-old model the displacement results continued increasing, reaching 2 μm at a mesh resolution of 600. Based on

his convergence study, he concluded that using the mesh resolution of 400 was a good trade-off between accuracy of the displacement results and computational costs.

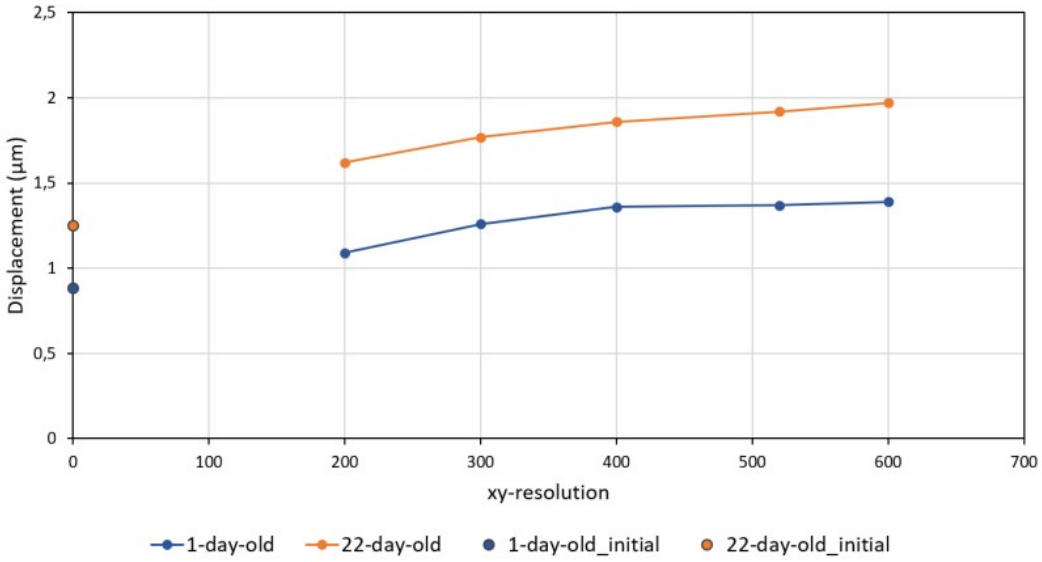

Figure 4.5: Results of convergence study conducted by Shaho for TM models of 1-day-old and 22-day-old, with five different XY-resolutions of the mesh.
For each mesh resolution, the resulting maximum displacement is displayed.

In this study, the geometry of the 1-day-old model was changed and a convergence study was done for the new geometry. When increasing the mesh resolution value to more than 400, no significant changes can be seen in the displacement response. Therefore, considering the convergence study done by Shaho (2020) and these new observations, the mesh resolution of 400 was chosen for all of the structures of the new model.

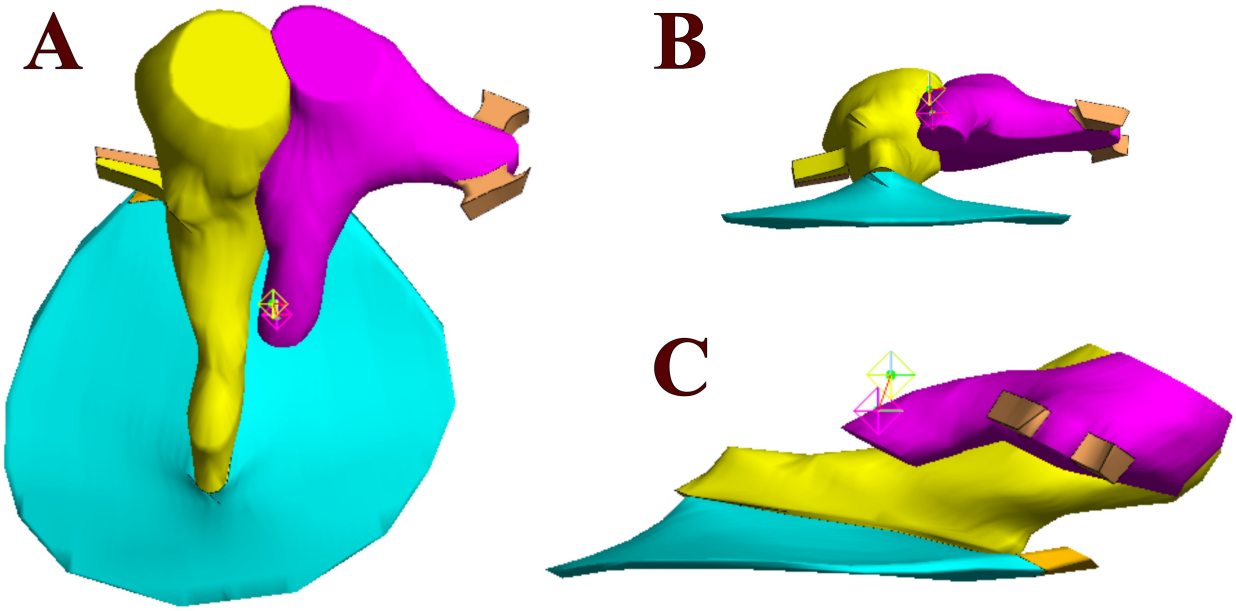

Figure 4.6: Final geometry of the 1-day-old model used in this study. The model consists of the malleus (yellow), incus (purple), pars tensa (cyan), pars flaccida (orange), anterior mallear ligament and posterior incudal ligament (brown). (A) Medial view. (B) Superior view, which provides a good indication of the degree of TM curvature. (C) Posterior view, with the spring and damper starting from the upper side of the incus and finishing at a fixed node in space.

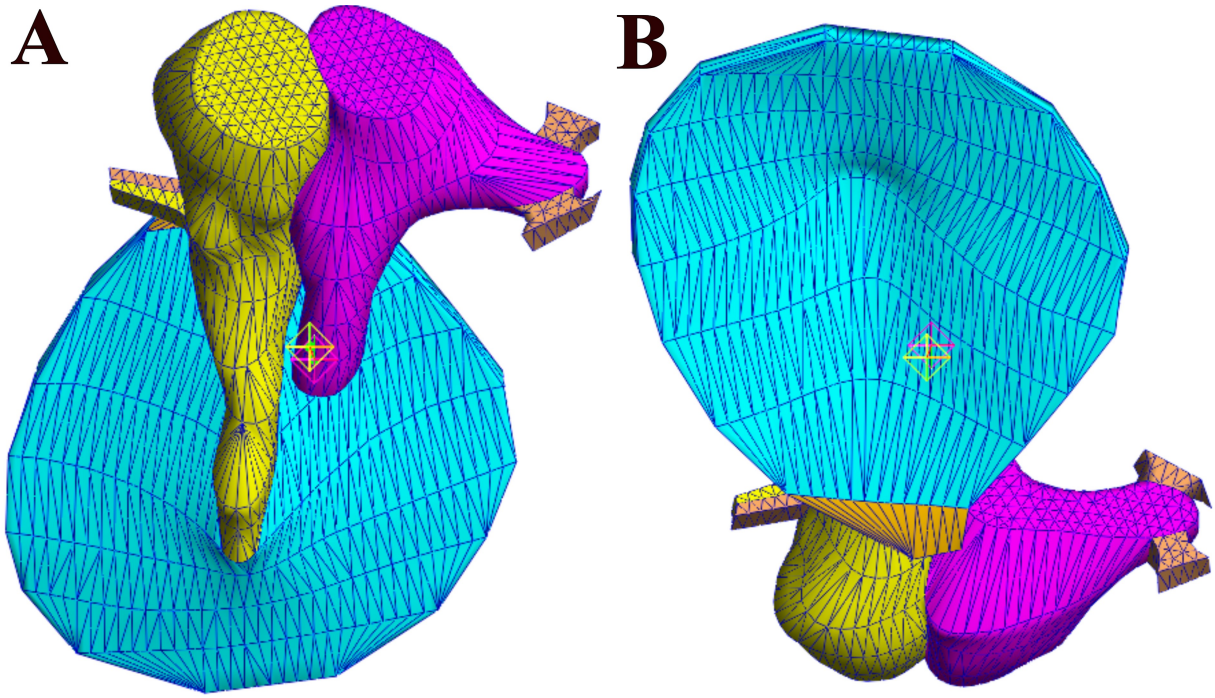

Figure 4.7: Finite-element mesh of the model. (A) Medial view. (B) Lateral view.

The geometry of the FE middle-ear model for the 1-day-old infant used in this study is shown in Figure 4.6. Additionally, the mesh of the model is shown in Figure 4.7. The total number of nodes used for the 3D reconstruction of the geometry is 11571. The numbers of quadratic elements used for the ligaments, malleus, incus, PT, and PF are 250, 2019, 1778, 2216 and 225, respectively.

4.4 Simulation software and hardware

As mentioned in Section 4.2 FEBio (https://febio.org/) (Maas et al., 2012) was used as the FE solver in the static and dynamic simulations in this study.

The dynamic simulations were usually run until 1 s of simulated time in the time domain and they were computationally expensive, so we used the Béluga cluster and later the Narval cluster of the Digital Research Alliance of Canada, previously Compute Canada. Narval contains a mix of AMD EPYC Rome and Milan processors connected by a Mellanox HDR InfiniBand network (www.docs.alliancecan.ca/wiki/Narval/en).

The baseline model ran for about 25 h on Narval, including about 16.5 h in the linear solver. For running our simulations we used 5 CPUs per task to benefit from FEBio's OpenMP-based parallel solver, and 4 GB of memory per CPU was used. (When the number of processors exceeded six, the software wasted time on transferring data, which resulted in decreased performance.) Some jobs required more than 25 hours of run time. (Simulations with a requested time of more than 40 hours were observed to have shorter queue times than those with shorter requested times.)

4.5 Tympanic-membrane thickness

4.5.1 Tympanic-membrane thickness in 22-day-old model

The thickness of the TM has important effects on the response of the middle ear. For developing a realistic mathematical model of dynamic TM behaviour, an investigation of this parameter is indispensable. As part of comparing our model to the 22-day-old model of Motallebzadeh et al. (2017a), we need to examine and compare the thicknesses of the TM's in the two models.

Motallebzadeh et al. (2017a) estimated the TM thickness for the CT-based 22-day-old model by using a 3D TM model reconstructed from histological images. They measured the apparent thickness 'at several points in each histological image using the Measure Tool in GIMP' (http://www.gimp.org). After that, in order to calculate the thickness distribution across the TM's cross section in each histological slice, they used a piecewise cubic Hermite interpolation algorithm in MATLAB.

They found that in the posterior superior quadrant the thickness was between 0.15 and 0.6 mm, while in the other three quadrants it varied between 0.07 and 0.4 mm (with the upper value corresponding to the TM annulus in each quadrant). They also found that the thickness of the PF (0.5-2 mm) was considerably higher than that of the PT (Motallebzadeh et al., 2017a). Their TM thickness results were consistent with those reported by (Ruah et al., 1991). To build the 3-D geometry of the TM, thicknesses were manually applied in the segmentation software (Fie).

4.5.2 Thickness calculation algorithms

In order to compare the TM thicknesses of the 22-day-old and 1-day-old models, we wanted to be able to calculate the spatial distributions of the thicknesses between the lateral and medial surfaces of the TM's in the two models. Algorithms for this purpose are described in this section.

Different methods for calculating the local thickness between two surfaces have been proposed in different articles for various application areas. Two important methods are used in many articles. The first one is an optimization problem that involves determining the diameter of the largest sphere that can fit inside the surface and be tangent to the surface at the point where the thickness is to be calculated. While this method has a very simple description, the calculation is extremely difficult. It involves calculating the diameter of the sphere in parametric form based on the tangent point and then comparing that diameter to other diameters to determine whether any other sphere point intersects other points on that surface. Some geometries cannot be handled properly with this method, resulting in two points near each other having very different thicknesses. In the second method, a ray-triangle intersection algorithm is employed, which is simpler and can be applied to triangulated mesh surfaces (Lambourne et al., 2005; Lanterne et al., 2016). This is the method used here.

4.5.3 Ray-triangle intersection algorithm

The ray-triangle intersection algorithm can be used to determine the local thickness at each point in a triangulated mesh. In this method, the normal vector of a node is calculated as the average of the normal vectors of the triangles which are attached to that point. A normal vector (**n**) can be determined by taking the cross-product of the vectors **a** and **b** between two pairs of points if you are given three points in the plane. The cross-product $\mathbf{n} = \mathbf{a} \times \mathbf{b}$ is perpendicular to both the **a** and **b** vectors. There are two types of normals for closed surfaces: the normal pointing inward (toward the surface's interior) and the normal pointing outward.

To use the ray-triangle intersection algorithm for calculating the thickness, for the candidate point where we want to measure the thickness we first calculate the normal vector of that point. Then, we consider the ray parallel to the normal vector that points into our volume. Using the well-known ray-triangle intersection algorithm we find that that ray intersects a triangle on the opposite surface of this volume. The length of that ray is taken to be the thickness (Badouel, 1990; Möller & Trumbore, 1997). In this study, the local thickness for our 1-day-old model was calculated using an implemtation of the ray-triangle intersection algorithm in MATLAB (Kabiri, 2023).

4.6 Material properties

4.6.1 Introduction

A range of plausible material property parameters of the components of the FE model were estimated since there is a lack of information in the literature about the material properties of the 1-day-old human middle ear. Most of our initial baseline parameters were adopted from the models of Motallebzadeh et al. (2017a). Adjusted parameters were then determined by evaluating the dynamic response of the model to an applied unit-step pressure, computing frequency responses, and comparing the results with the linear 22-day-old model of Motallebzadeh et al. (2017a).

A normal middle ear demonstrates linear behaviour at low to moderate sound pressures. Linear isotropic viscoelastic models were used for the PT, PF and ligaments in this study. The ossicles,

on the other hand, were considered to be linear isotropic elastic since they are very stiff and do not easily deform, so energy loss can be neglected.

Detailed material properties of the different components of the FE model are given in Table 4.1 and described in the following sections.

Table 4.1: Material properties from the literature and the baseline values used in this study. See text for background information.

Structure parameters	***Literature ranges***	***This study***
Young's modulus of pars tensa (MPa)	0.6 (Qi et al., 2008a) to 10 (Motallebzadeh et al., 2017a)	1.5
Young's modulus of pars flaccida (MPa)	0.4 (Agache et al., 1980) to 2 (Geerligs et al., 2011)	2
Young's modulus of ligaments (MPa)	0.65 (Koike et al., 2002) to 21 (Gan et al., 2004)	8
Young's modulus of ossicles (GPa)	17.6 to 18.9 (Fung, 1993, p. 511)	13
Poisson's ratio of soft tissues	0.5 (Decraemer & Funnell, 2008)	0.485
Poisson's ratio of ossicles	0.3 (Cowin, 2001; Koike et al., 2002)	0.3
Density of soft tissues (kg/m^3)	1000 to 1200 (Funnell & Laszlo, 1978)	1200
Density of ossicles (kg/m^3)	1600 to 1950 (Fung, 1993)	2000
Prony coefficients of soft tissues	Varies in different studies	0.5
Spring (N/m)	68 (Kwacz et al., 2015) to 1050 (Lauxmann et al., 2014)	600
Dashpot (N.s/m)	0.2 (Motallebzadeh et al., 2017a) to 0.89 (Koike et al., 2002)	0.45

4.6.2 Young's modulus

4.6.2.1 Pars tensa

According to Lim (1970), the TM consists of three layers. The outer layer or epidermis of the TM has an ultrastructure similar to that of the skin epidermis. The middle layer or lamina propria is composed of two densely packed layers of collagen fibres which are arranged in circular and radial patterns respectively, and two layers of loose connective tissue. The thin inner layer, or

lamina mucosa, is composed of a large number of columnar cells. The lamina propria, which is distinguished by the presence of type II collagen fibres, is primarily responsible for the overall mechanical properties of the TM. Both experimental and modelling studies have been used to investigate the Young's modulus of the human adult TM as mentioned in Section 3.3.4, but so far the Young's modulus of the newborn TM has not been examined.

Agache et al. (1980) conducted a histological examination of skin and reported that collagen density increases as the skin ages and collagen fibers become less extensible. Rosenwasser et al. (1964) reported that the TM becomes stiffer with age. Ruah et al. (1991) observed similarities between the changes in TM ultra structure that occur with age and the changes in human skin. They studied the human TM morphological changes with age using electron microscopy or light microscopy on ears from patients aged from 33 gw to 91 years, and concluded that with age the TM becomes 'less vascular, less cellular, more rigid, and less elastic. Anthwal and Thompson (2016) found that the TM lateral layer has the same maturation process and happened with the same time course as skin. Several studies have investigated the changes in mechanical properties of collagenous tissues such as human skin with age and identified several factors responsible for this phenomenon, including collagen fibre orientation and density, and skin water content. Studies have also been conducted on the Young's modulus in relation to aging human skin. Rollhäuser (1950) examined the skin's age-related Young's modulus in newborns as young as three months old to adults. He reported that adult skin has a Young's modulus approximately seven to eight times higher than infant skin does. Yamada (1970) reported that the Young's modulus of adult skin is about six times greater than that of infant skin, which is in accordance with the results reported by Rollhäuser (1950).

Luo et al. (2009a, 2009b) reported that in dynamic situations, the normal TM's Young's modulus is more than twice its value in static condition. Qi et al (2008a) developed a static model for a 22-day-old middle ear and used the Young's moduli of 0.6, 1.2 and 2.4 MPa. Motallebzadeh et al. (2017a) chose Young's modulus values of 2, 6 and 10 MPa for their linear 22-day-old model for their low-impedance, baseline and high-impedance models, respectively. They used 2.4 MPa for the Young's modulus of the PT in their final adjusted model. Shaho (2020) used the value of 10 MPa for his 1-day-old static model, equal to the upper value used by Motallebzadeh et al. (2017a). The value chosen by Shaho (2020) is half the size of those reported for adults. In this

study, after comparing our baseline model with the 22-day-old model of Motallebzadeh et al. (2017a), we decided to use a Young's modulus of 1.5 MPa for the PT.

4.6.2.2 Pars flaccida

According to Lim (1970) the PF is an extension of the external ear canal's skin. Agache et al. (1980) measured a Young's modulus of about 0.4 MPa for in vivo dermis (skin) by applying a torque. Geerligs et al. (2011) measured a range of 1 to 2 MPa for Young's modulus for the human epidermis and stratum corneum using micro-indentation measurements and a numerical model. Considering these findings, Maftoon et al. (2015) employed a Young's modulus of 2 MPa for the PF of the gerbil middle ear.

Motallebzadeh et al. (2017a) used 0.4, 1.2 and 2 MPa for the PF Young's modulus in their low-impedance, baseline and high-impedance models, respectively. They concluded that their high impedance middle-ear model was more consistent with clinical findings. Therefore, the Young's modulus chosen by Motallebzadeh et al. (2017a) for their adjusted model was 2 Mpa. Shaho (2020) also used a Young's modulus of 2 MPa for the PF in his linear static model.

In this study the same Young's modulus of 2 MPa was chosen for the PF in our baseline model.

4.6.2.3 Ligaments

A wide range of Young's modulus values, from 0.65 to 21 MPa, were used for ligaments of the middle ear in adult models in previous studies (Gan et al., 2004; Koike et al., 2002). Qi et al. (2008a), in their newborn model, assigned Young's modulus values of 1, 3 and 5 MPa, which is approximately 2 to 10 times smaller than the values used in adult human middle-ear models by Koike et al. (2002). Based on their structural similarity, Maftoon et al. (2015) used the same Young's moduli for ligaments and PT. Motallebzadeh et al. (2017a) used the three values of 2, 5 and 8 MPa for the ligaments in their low-impedance, baseline and high-impedance models, respectively. They used the value of 8 MPa for their adjusted model. Later Shaho (2020) also used 8 MPa. Here we decided to also use 8 MPa.

4.6.2.4 Ossicles

Several values have been reported in the literature for the Young's modulus of compact bone. According to Fung (1993, p. 511), the mechanical properties of bone change with age, sex,

location in the body, strain rate and the orientation of the load. He reported a range of 17.6–18.9 GPa. Olszewski et al. (1990) showed that after birth the mass and size of the ossicles continue to develop. Yokoyama et al. (1999) studied ossicle development in 32 samples with ages of 1 day to nine years. They reported that the bone marrow inside the malleus and incus in the newborn slowly transforms into bone and they concluded that the ossicles undergo ossification until about 25 months after birth. Therefore, the Young's modulus for the newborn model should be smaller than that for adults. Qi et al. (2008b) used Young's moduli of 1, 3 and 5 GPa in their 22-day-old FE model. Soons et al. (2010) measured Young's moduli of 16 ± 3 GPa for the incus and malleus in rabbits. Motallebzadeh et al. (2017a) used Young's moduli of 4, 10 and 16 GPa for the ossicles in their 22-day-old model. They chose the lower Young's modulus value based on the lower value in the literature review of Funnell et al. (1992), while the upper value was assigned considering the average value in the experiments of Soons et al. (2010). The middle value (10 GPa) was the mean of the upper and lower values.

Shaho (2020) used a Young's modulus of 13 GPa based on the observations and literature references of Motallebzadeh et al. (2017a). In this study, we also chose a Young's modulus of 13 GPa for our baseline model.

4.6.3 Poisson's ratio

The compressibility of a material is measured by the Poisson's ratio, which usually varies between zero (e.g., for cork) and 0.5 (for an incompressible material). Soft tissues are almost incompressible, so values for their Poisson's ratio that are close to 0.5 are reasonable (Decraemer & Funnell, 2008). Qi et al. (2006a), to prevent numerical problems arising from full incompressibility, used a value of 0.49 for the soft tissues of the TM and ligaments. For the ossicles (malleus and incus), a Poisson's ratio of 0.3 was chosen as in many previous studies (e.g., Cowin, 2001; Koike et al., 2002). Motallebzadeh et al. (2017a) used the values of 0.485, 0.49 and 0.495 for the Poisson's ratio of the soft tissues in their low-impedance, baseline and high-impedance models, respectively. Ultimately they used 0.495 for their adjusted model and 0.3 for the for the Poisson's ratio of bone. Shaho (2020) used the value of 0.485 for the Poisson's ratio of the soft tissues, and 0.3 for the bone. In this study the values of Shaho (2020) were used for the soft tissue and bone.

4.6.4 Density

The densities (mass per unit volume) of soft tissues are usually reported as being between those of water (1000 kg/m^3) and that of undehydrated collagen (1200 kg/m^3) (Funnell & Laszlo, 1978). Based on that, Maftoon et al. (2015) used 1100 kg/m^3 as the initial value of the density of the PT. Then, to match the resonance frequency with the results of *in vivo* experimental measurements on PF obtained by Maftoon et al. (2014), the density value for PT was changed to 1300 kg/m^3. They commented that another approach would have been to reduce the Mooney-Rivlin coefficients to reduce the effective Young's modulus. In that case, the response at lower frequencies could have been stiffened by adjusting the ossicular load. Motallebzadeh et al. (2017a) used the densities of 1000, 1100 and 1200 kg/m^3 for the soft-tissue parts of their low-impedance, baseline and high-impedance models, respectively. They then used 1200 kg/m^3 for their adjusted model. Shaho (2020) used a density of 1200 kg/m^3 for the TM and ligaments, the same as the middle value used by Motallebzadeh et al. (2017a). In this study we used 1200 kg/m^3 for the soft tissue densities.

Fung (1993) reported a bone density range from 1600 to 1950 kg/m^3. Maftoon et al. (2015) used the values of 1918, 1855 and 1565 kg/m^3 for the densities of malleus, incus and stapes, respectively, in their model. Motallebzadeh et al. (2017a), based on the statement by Fung (1993), used the values of 1600, 1800 and 2000 kg/m^3 for the density of malleus and incus, which is almost the same as the range used by Maftoon et al. (2015). Shaho (2020) used a density of 2000 kg/m^3 for the ossicles, which was equal to the upper value used by Motallebzadeh et al. (2017a). In this study, we used 2000 kg/m^3 for the ossicle densities.

4.6.5 Prony series parameters

Rayleigh damping is one of the most common ways of modelling damping (e.g., Funnell et al., 1987). Rayleigh damping is a mathematical representation of the damping matrix that consists of a linear combination of the stiffness matrix and the mass matrix. Some of the previous studies from our group that used the FE solver Code_Aster (https://code-aster.org/) employed the Rayleigh damping model (Maftoon et al., 2015; Choukir, 2017; Motallebzadeh et al., 2017a; Qian, 2019). However, there is no option to use Rayleigh damping in FEBio.

As mentioned in Section 3.4, $G(t)$ in equation (3-9) is a normalized relaxation function and the Prony series is a form of $G(t)$ that is used in this study. Each term of a Prony series involves two parameters: g_i (relaxation coefficient) and τ_i (time constant). The level of damping at the frequency corresponding to the time constant τ_i is represented by the relaxation coefficient g_i.

The acoustic stimuli in both wideband tympanometry and LDV measurements are usually in the range of 0.1 to 10 kHz. In our study, we investigate the linear middle-ear response to the same range of frequencies. Below 100 Hz the middle-ear response is stiffness-dominated and there are no significant changes in the response of the middle ear to sound pressure. Above 10 kHz the sound pressure across the TM is not uniform, making it challenging to investigate the middle-ear response in that range.

In order to cover the spectrum from the low frequencies to the high frequencies of the acoustic stimulus for PT and PF structures, five time constants were predefined that cover the range from 10 Hz to 100 kHz. It is common to take one time constant per decade, whether it is in the frequency domain or the time domain (e.g., Knauss & Zhao, 2007; Charlebois et al., 2013; Fung, 2013). An angular frequency can be obtained by inverting each time constant, and at that frequency is the highest damping as represented by the coefficient (g_i):

$$\omega_i = 1/\tau_i = 2\pi f_i \tag{4-1}$$

In this study we use one time constant per decade: τ_1=1.59e-06 s (≈629 krad/s), τ_2=1.59e-05 s, τ_3=1.59e-04, τ_4=0.00159s, τ_5=0.0159s (≈62.9 rad/s).

Employing these parameters in the model, we investigated the dynamic response of the model to sound pressure and compared the model response qualitatively to the results from the linear 22-day-old model of Motallebzadeh et al. (2017a). Figure 4.8 shows a comparison of the TM response using a coefficient from 0.1 to 1 for all time constants. When the Prony coefficients were increased, the resonance peak flattened and the resonance frequency shifted to the higher frequencies. As expected, damping increases at all frequencies as the coefficient increases.

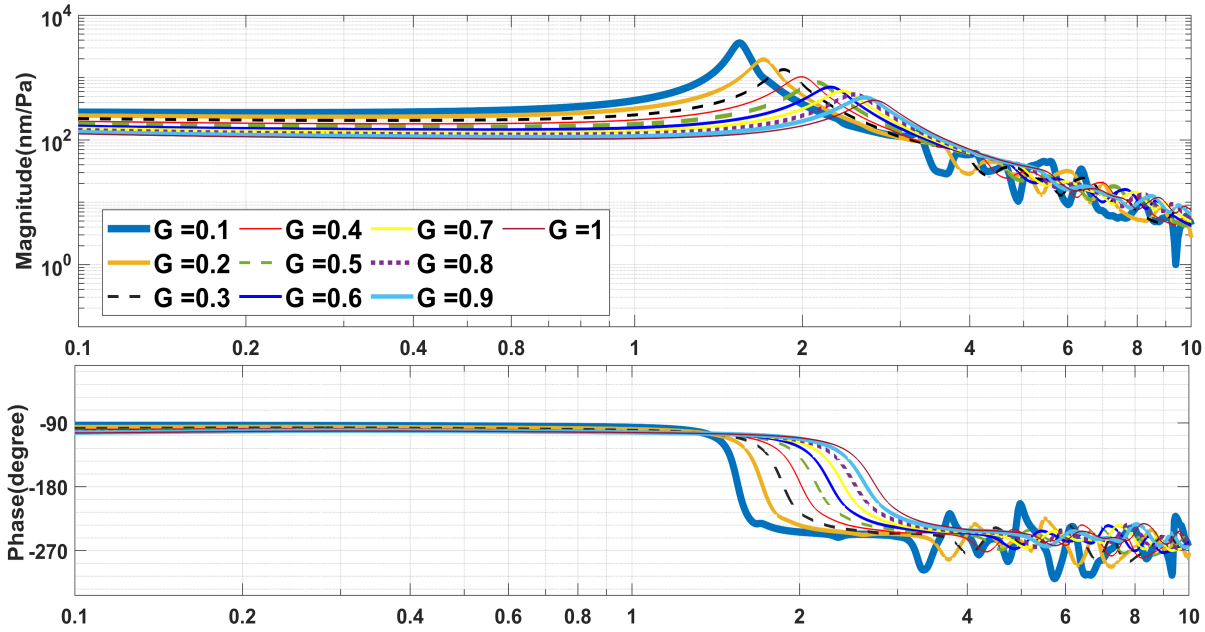

Figure 4.8: *Effects of uniform Prony coefficients on frequency response of TM.*

Figure 4.9 shows the effects on the TM response of a decrease of the Prony coefficients by a factor of 0.1. As expected, this decreases the damping and makes the resonance peak sharper and moves it to the lower frequencies. In our baseline model, we used a value of 0.5 for all the Prony coefficients, which causes the PT to be sufficiently dampened without eradicating the complicated displacement pattern at higher frequencies.

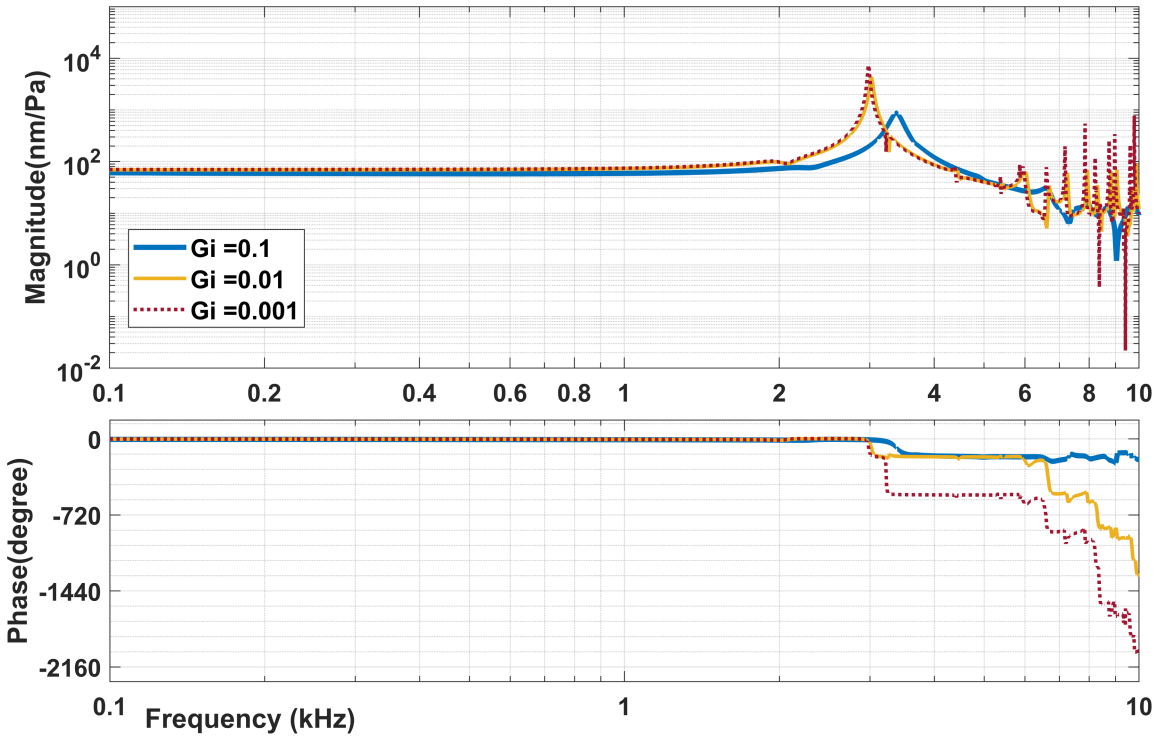

Figure 4.9: Effects of very low Prony coefficients on frequency response of TM.

4.7 Discrete elements

4.7.1 Spring

The stapedial annular ligament constrains the movement of the stapes in all three directions. However, the stapes moves primarily in a translational or piston-like manner at low frequencies such as 1 kHz and the movement is approximately parallel to the direction of the effective load at low frequency (e.g., Decraemer & Khanna, 2004b; Hato et al., 2003). Although we study the response of the model up to 10 kHz, we represent the effect of the stapedial annular ligament with a single translational spring element located at the medial end of the long process of the incus where the incudostapedial joint would be located.

Several attempts were needed to define the spring in Fie. Assigning the spring in Fie requires understanding the stapes' and footplate's orientation and location, but the stapes and footplate were not clearly identifiable due to the low CT resolution. Using slices from the 1-day-old model and the 22-day-old model and comparing the development of structures, we attempted to

determine the location of the stapes and footplate and segment them. Several models were analyzed to determine the location of the stapes using the TM location (e.g., Mikhael et al., 2005; Motallebzadeh et al., 2017a; X. Wang, 2019; Golabbakhsh et al., 2020; Golabbakhsh & Funnell, 2021), but these attempts were not successful in determining the correct spring location.

As an alternative approach to defining the spring, the direction of the incus movement was first determined. Then, a middle node was chosen on the cross-section of the end of the long process of the incus. Following that, the X, Y, and Z coordinates of that node were determined. A pressure of 1 Pa was applied to the TM, and the node displacement from the initial position to the final position of the chosen node was calculated in all three directions. Scaling up the small calculated displacements in the X, Y, and Z directions and adding the result to the initial position indicated the direction of the stapes movement and served to define the coordinates of the node at the clamped end of the spring representing the stapedial annular ligament.

In FEBio, the calculated coordinates were used to specify a rigid body in space, and its coordinates were used as the centre of mass of that artificial rigid body (using the technique that is required for discrete dashpots in FEBio, as described in the next section). The rigid body was fixed in space with all degrees of freedom. Additionally, the starting point of the spring on the incus was also defined as a rigid body with the coordinates as a centre of mass. Then a discrete spring element was assigned between the two rigid bodies.

Cancura (1979) reported 182 N/m for the stiffness of the stapedial annular. Lauxmann et al. (2014) reported the stiffness to be 1050 N/m, which is much higher than the other values reported.

Kwacz et al. (2015) reported that the stiffness ranges from about 68 to 198 N/m with a mean value of 120 N/m. Motallebzadeh et al. (2017a) used the three values of 200, 600 and 1000 N/m for the stiffness of the stapedial annular ligament in their low-impedance, baseline and high-impedance FE models, respectively. In this study, we use their baseline value of 600 N/m.

4.7.2 Cochlear load

The cochlea is reported to damp the response of the human ear, at least in the frequency range taken into account in this study (Aibara et al., 2001; Merchant et al., 1996). Based on some measurements in the gerbil ear, the cochlear load produces pure viscous damping in most of the

frequency range between 0.2 and 20 kHz (de la Rochefoucauld et al., 2008; Decraemer et al., 2007; Ravicz et al., 2008).

To simulate the effect of damping of the cochlear load, a discrete dashpot (a viscous damper) was added to our model. Similar to the spring element in Section 4.7.1, the dashpot element in this model starts at a point on the medial part of the long process of the incus and ends at a fixed point in space.

In FEBio, dashpots must be attached through a rigid-body interface, so the dashpot is connected to the rigid body (a node defined as a rigid body) on the incus long process at one end and it is connected to the rigid body fixed in space at the other end. In order to avoid simulation errors, it is important to set the flag <check_zero_diagonal> to 0 (false) when dealing with rigid connectors, since they are configured not to have bending stiffness.

The viscous damping coefficient can be obtained by dividing the cochlear input impedance by the square of the stapes footplate area. Koike et al. (2002) computed a coefficient of 0.89 N.s/m for the impedance of 50 G in the model of the adult human. Wever and Lawrence (1954) estimated the surface area of the footplate to be in the range of 2.3–3.75 mm^2. Gan et al. (2011) reported almost the same range for the surface area of the stapes footplate. Based on these studies, Motallebzadeh et al. (2017) used the three values of 0.2, 0.45 and 0.7 N.m/s for his dashpot parameter which represented the cochlear load, saying that no measurements had been made to support adjusting these values for potential variations between babies and adults.

De La Rochefoucauld et al. (2008) calculated a viscous damping coefficient of 15.4×10^{-3} N·s/m for their gerbil model by obtaining an average cochlear input impedance of 4×1010 Pa·s/m^3 for frequencies less than 30 kHz and using a footplate area of 0.62 mm^2. Maftoon et al. (2015) uniformly distributed this value to four dashpots perpendicular to the stapes footplate in his gerbil model (Maftoon et al., 2015).

Choukir (2017) used a dashpot with a viscous damping coefficient of 2.04×10^{-3} N.s/m in her Code_Aster gerbil model. Compared to Maftoon et al. (2015), Choukir (2017) used a smaller value since the damper in her model is attached perpendicular to the manubrium near the umbo rather than to the stapes footplate, which results in a stronger influence on TM vibrations patterns. However, Choukir (2017) in her FEBio model used a very high relaxation coefficient of

16 for a Prony time constant of 10 μs for the manubrium and wedge in order to simulate the effect of the cochlea damping.

Later Qian (2019), after comparing the response of her model in the linear low-frequency range at the umbo to the response of the model of Maftoon et al. (2015), used the damping coefficient of 6.3×10^{-3} N.s/m for each dashpot in her Code_Aster model. Qian (2019) adjusted the damping coefficient slightly to 6.0×10^{-3} N.s/m in her FEBio model.

In this study we used the same value as Motallebzadeh et al (2017a), 0.45 N.s/m, for the 1-day-old model damper coefficient which represents the cochlear load.

4.8 Boundary conditions

A fibrocartilaginous ring attaches the TM to the bone. To represent an approximation of the TM's anatomy, the TM in our model was clamped at all nodes around its entire circumference, as in most previous middle-ear models (e.g., Rabbitt & Holmes, 1986; Gea et al., 2010; Aernouts et al., 2012). In addition, boundary conditions were applied to represent the effects of the ligaments that connect the middle-ear structures to the middle-ear cavity walls. The ends of the AML and the two bundles of the PIL were clamped at the place where they attach to the temporal bone. For the other parts of the model, there were no restrictions on the movement. A 1-Pa step function of pressure was applied on the lateral side of the PF and PT.

These boundary conditions and loads are defined in the source code of the model (i.e., in the '.tr3' file) by specifying them for each relevant line in Fie, and then Tr3 applies them to the appropriate nodes.

4.9 Loading conditions and time-step analysis

As outputs, we obtained the displacement and velocity data for five nodes: on the posterior part of the PT, the anterior part of the PT, the umbo, the middle of the PF, and the stapes. After the start of the unit step of pressure, the simulations continued for 1 s. By that time the system had essentially reached steady state for all values of the damping. Fast Fourier transforms (FFT's) were calculated from the velocity outputs to obtain frequency responses. The chosen time span of 1 s gives a frequency resolution of 6.5 Hz.

It is crucial to choose the right simulation time step, which determines the greatest frequency content of the outputs. In FEBio, most simulations were run using varying step sizes, between a minimum of one-third of the specified step size and a maximum of three times the specified step size, to save compute time. To obtain equal time steps for the FFT calculations, an interpolation algorithm was implemented in MATLAB. For the sake of selecting an acceptable time-step size, however, we ran simulations with fixed time steps. At first we encountered errors for some time-step sizes, which turned out to be because of problems with convergence during the almost steady-state portion of the simulations, when numerical round-off errors are larger than the displacement changes from time step to time step. The problem was finally solved by setting the 'min_residual' value to 1e−15, larger than the default value of 1e−20. We confirmed that this did not affect the simulation results.

In Figure 4.11 the effects of the time-step size on the frequency response for the TM are presented for values of 75, 50, 30, 15, 10 and 5 μs. The TM was selected for the time-step analysis since it is a more sensitive indicator than the umbo. For time steps of 5 to 30 μs, an increase of less than 0.004 nm/Pa is seen in the magnitude at 100 Hz. At the resonance frequency of 1.85 kHz, the differences in the magnitude between the two time steps of 5 and 30 μs are 108 nm/Pa. After around 3.8 kHz the differences in magnitude between the results with time steps of 5, 10 and 15 μs and the results with time steps of 30 μs start to increase significantly. The differences in magnitude between the time steps of 5 and 10 μs are very small until the frequency of 6.5 kHz. For example, the differences in magnitude between the time steps of 5 and 10 μs at 2 kHz, 2.5 kHz and 9 kHz are 3.4 nm/Pa, 0.74 nm/Pa and 1.00 nm/Pa, respectively. For our simulations for this loading situation, we chose a time step of 10 μs as a trade-off between precision and computation time.

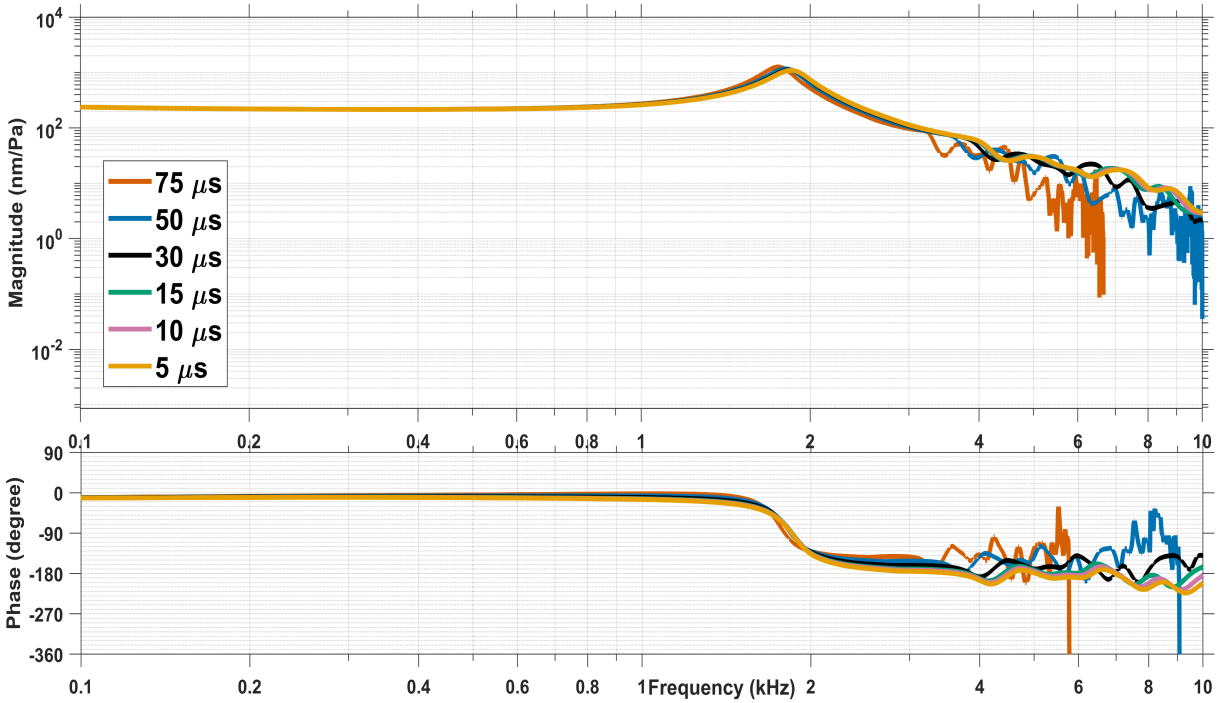

Figure 4.10: Effect of different time-step sizes on simulated PT response.

4.10 Sensitivity analysis

A sensitivity analysis was conducted to determine how parameter values affect model behaviour and to provide suggestions for improving the model by adjusting those parameters. A one-variable-at-a-time sensitivity analysis was conducted after establishing a baseline set of material properties.

In our sensitivity analysis, each parameter was increased or decreased by 10%, 20% and 40% of its baseline value while maintaining the baseline values of all other parameters. The ranges of parameters such as Young's modulus, density and spring coefficient can be considered limitless, but the Poisson's ratio has a finite range for all stable isotropic elastic materials, ranging from zero up to to 0.5 for completely incompressible materials (e.g., Y. C. Wang & Lakes, 2005). In our sensitivity analysis, the material stiffness is defined in terms of Young's modulus (E) and bulk modulus (B) rather than Young's modulus and Poisson's ratio (ν), based on equation (4-2):

$$B=\frac{E}{3(1-2\nu)} \tag{4-2}$$

This was done to avoid problems when Poisson's ratio is changed near its upper limit of 0.5.

Chapter 5. Results

5.1 Introduction

Section 5.2 presents the results of modifications and variations applied to the geometry of the 1-day-old model, as well as modifications applied to the mesh pattern. In Section 5.3, the thickness distribution for the 1-day-old model is presented, and then the thickness distribution is compared with that of the model of Motallebzadeh et al. (2017a) in Section 5.4. In Section 5.5, the static displacements for distinct regions of our middle-ear model are shown. The low-frequency TM vibration pattern is compared with that of the model of Motallebzadeh et al. (2017a) in Section 5.6. The responses of different regions of our 1-day-old model are compared in Section 5.7 in the time domain and frequency domain. In order to show how parameter values affect model behavior, sensitivity analyses are presented in Sections 5.8. and 5.9. In Section 5.10, after considering the effects of the canal wall and the middle-ear cavity, our model is compared with the adjusted model of Motallebzadeh et al. (2017b) and with measured data.

5.2 Geometry and mesh pattern

Figure 5.1 shows a comparison of the geometries and meshes of the current 1-day-old model of the left middle ear with the previous model by Shaho (2020). On the top side of the long process of the incus, the springs and dampers assigned in the current model can be seen in Figure 5.1 A. One of the most significant differences between these two models is the shape of the long process of the incus, as the current model has a shorter long process and smaller size of the incus compared with Shaho's model (Figure 5.1B). The segmentation was adjusted in each slice, using trial and error in some places due to the poor resolution of the CT images. In addition, the diameter of the incus was decreased, and the location of the tip of the long process of the incus was changed according to the CT images. Figure 5.2 shows inferior, superior and posteromedial views of Shaho's 1-day-old and the current 1-day-old model.

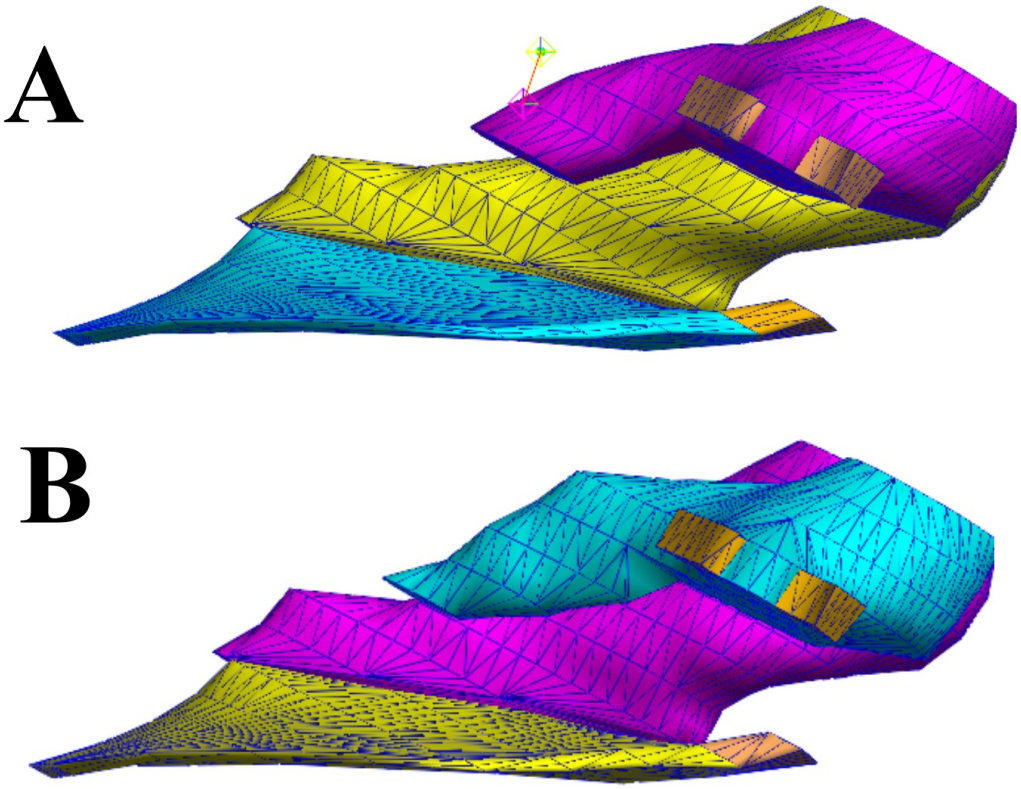

Figure 5.1: Posterior views of 1-day-old models.
(A) Current model. (B) Previous model by Shaho (2020). The current model includes malleus (yellow), incus (purple), ligaments (brown), and tympanic membrane, which comprise the pars tensa (cyan), and pars flaccida (orange). The model generated by Shaho comprises malleus (purple), incus (cyan), ligaments (brown), and tympanic membrane, which comprise the pars tensa (yellow) and pars flaccida (orange). The spring and damper are visible on the upper surface of the long process of the incus in panel A. Panels A and B illustrate the differences of shape and length of the long process of the incus.

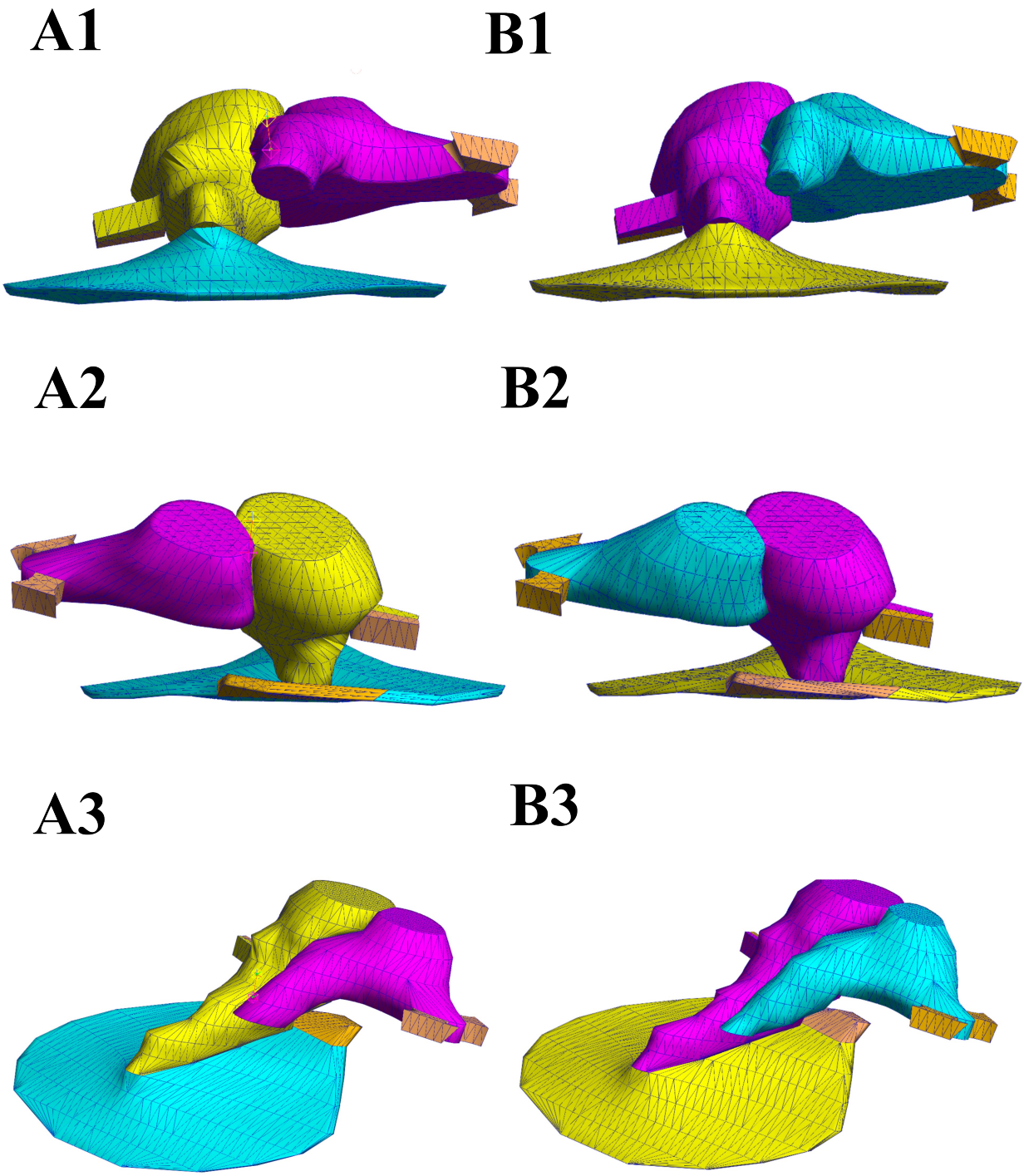

Figure 5.2: Three views of 1-day-old models.
A1, A2, A3: Current model. B1, B2, B3: Previous model by Shaho (2020). Panels 1, 2 and 3 show inferior, superior and posteromedial views.

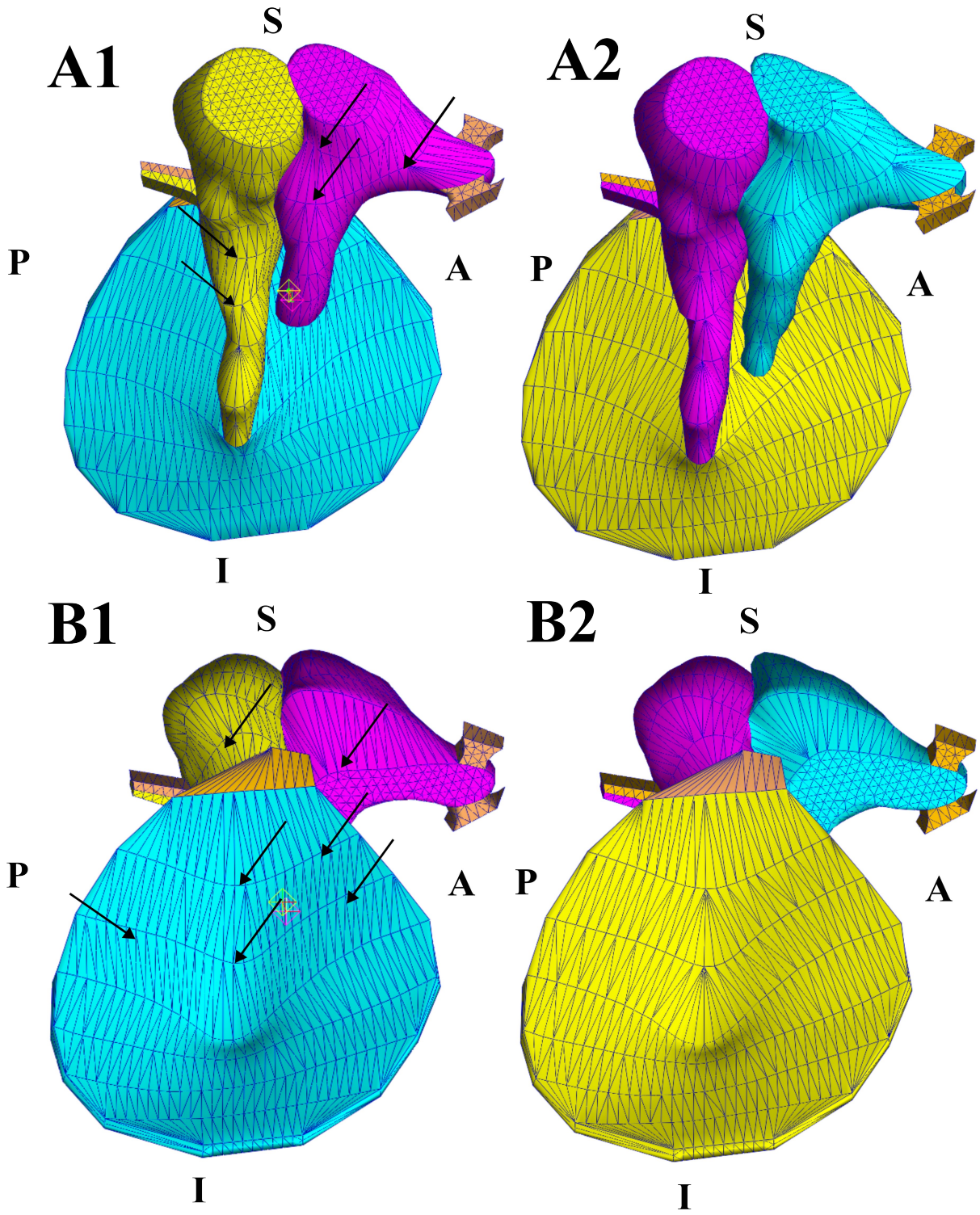

Figure 5.3: Mesh differences between 1-day-old models.
(A1 and B1) Current model. (A2 and B2) Previous model by Shaho (2020). Medial and lateral views in panels A and B, respectively. In panels A1 and A2, differences in the mesh patterns in the incus and malleus are seen, especially on the long process of the incus and on the manubrium of the malleus (arrows). In panels B1 and B2, differences in the mesh patterns on the TM lateral side are seen (arrows). A = anterior, P = posterior, S = superior and I = inferior.

The mesh pattern has been modified in the current model, as shown in Figure 5.3. Differences in mesh pattern can be seen in the incus and malleus, especially on the long process of the incus and the manubrium of the malleus (arrows in panel A1). The modification in the mesh pattern can be visibly distinguished on the lateral side of the TM (arrow in panel B1), corresponding to where the umbo and manubrium are located on the medial side, as well as in the posterior and anterior regions on the lateral side of the TM.

5.3 Thickness

5.3.1 1-day-old model thickness distribution

The thickness distribution of our 1-day-old model is illustrated in Figure 5.4, based on using the ray-triangle intersection algorithm described in Section 4.5. The scale bar on the right shows thickness values based on colour. The maximum thickness is shown in dark red, and the minimum thickness is shown in dark blue. We see that the central part of the PT is thinner than the border and, as we move from the centre of the TM to the border, the thickness increases.

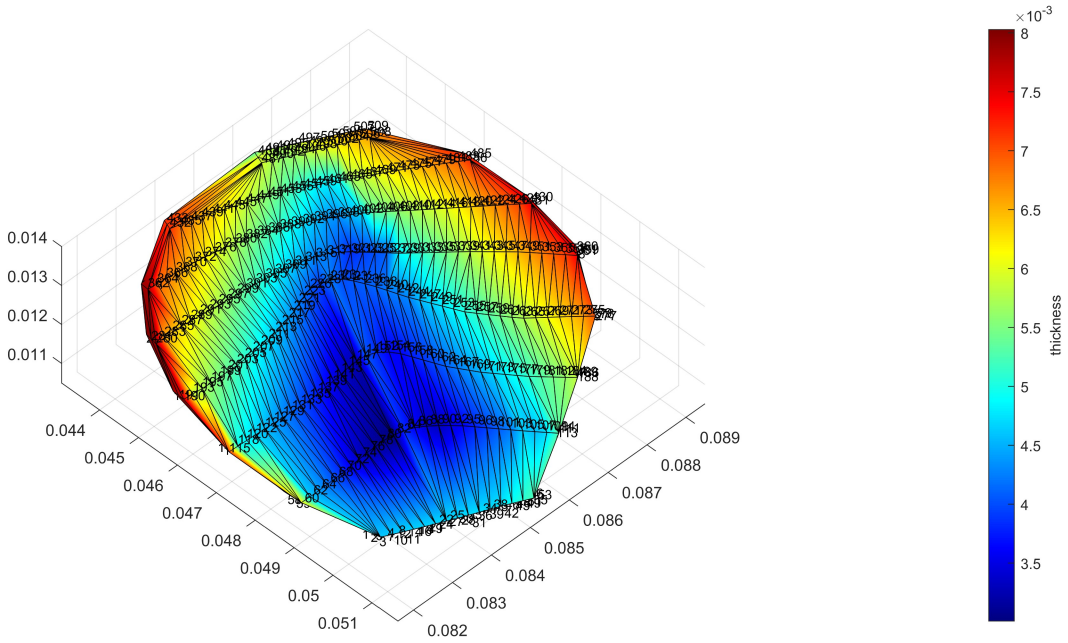

Figure 5.4: Distribution of TM thickness in 1-day-old model.

5.3.2 Comparison of 1-day-old model and 22-day-old model

A montage is shown in Figure 5.5 in order to compare the TM's in the 1-day-old model and the 22-day-old model in terms of thickness and curvature. The montage was made using screenshots captured from Fie. The segmentation related to the TM is shown by the green lines for the 1-day-old model and by yellow lines for the 22-day-old model. The CT scan of the 1-day-old model shows the left ear, while the CT scan of the 22-day-old model shows the right ear. The first number for each slice is related to the number of slices in this figure, and the second number (after '#') gives the number of the slice in Fie. As we can see, in slice 1, the thicknesses of the TM in the 1-day-old model and 22-day-old model are approximately equal. The air-filled space (where the pixels are dark grey) is segmented with the beige line in the 22-day-old model, but in the 1-day-old model this space is not completely air-filled due to the presence of mesenchyme or amniotic fluid. In slice 2, we can see that the lengths of the manubrium in the 1-day-old and 22-day-old models are the same, and the thicknesses of the TM are approximately equal. In slice 3, it is evident that in the 22-day-old model the end of the malleus near the TM became darker grey due to the angle of the manubrium. The thickness of the TM is approximately the same in both the 1-day-old model and the 22-day-old model in slice 3. There are some differences in the curvature of the segmented TM between the 1-day-old model and the 22-day-old model. However, this is an approximate segmentation and there may or may not have actually been different curvatures in the two ears. In slice 4, the thickness is almost the same, while some mesenchyme and fluid were in the ear canal of the 1-day-old ear. In slice 5, the thickness is approximately equal between the two models. The curvature based on the segmentation is almost the same in slices 4 and 5. The TM has practically the same thickness in slices 6, 7, and 8, while the 22-day-old TM segmentation is more curved than in the 1-day-old model. We can see in the 1-day-old model that the air-filled space is closed in slice 9 and TM segmentation finishes in that slice, while in the 22-day-old model this happens in slice 11.

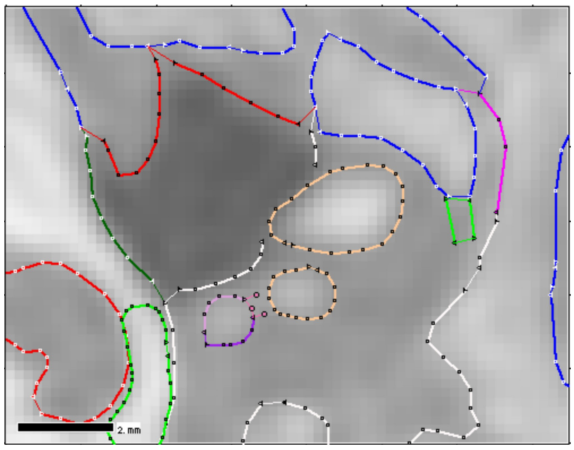

Slice 1 (#20)

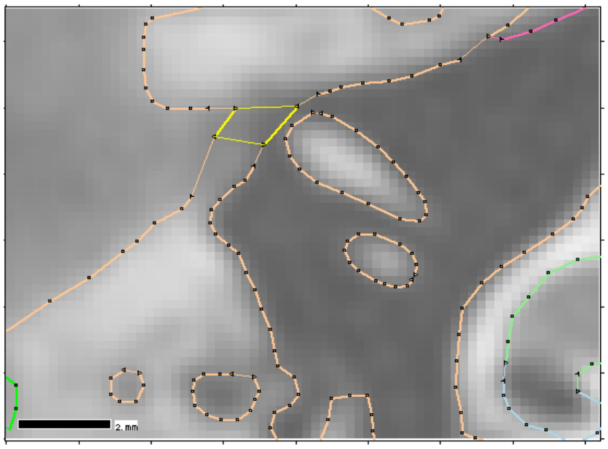

Slice 1 (#34)

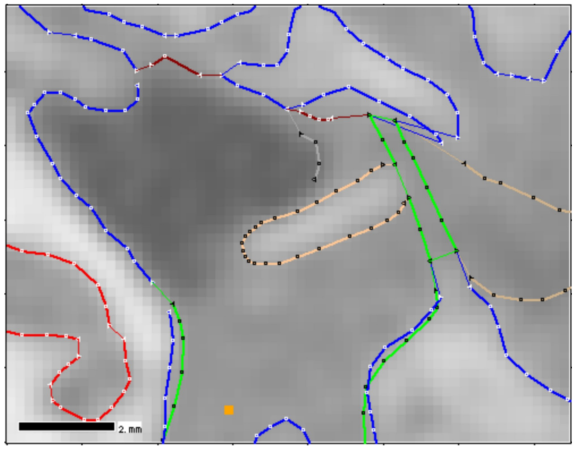

Slice 2 (#21)

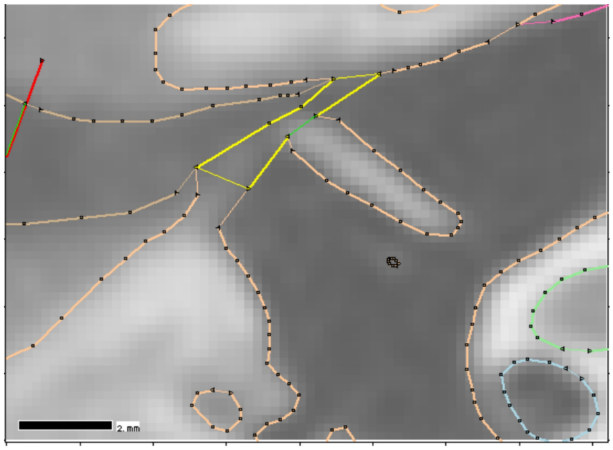

Slice 2 (#35)

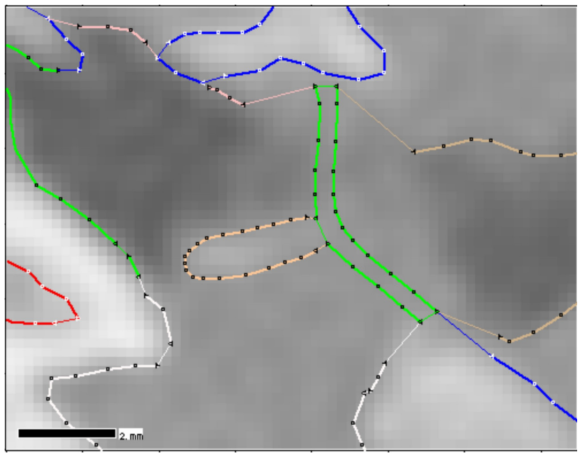

Slice 3 (#22)

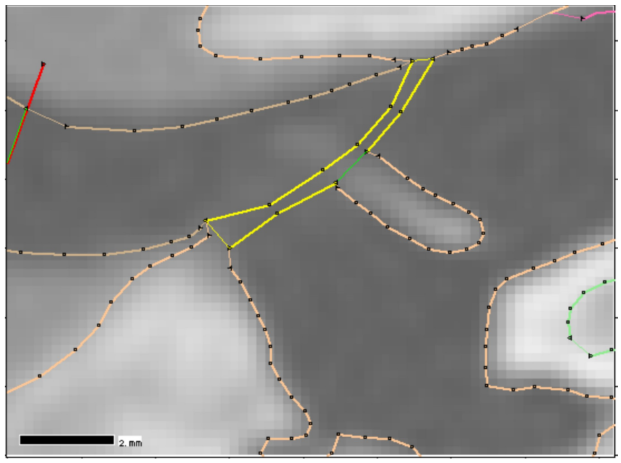

Slice 3 (#36)

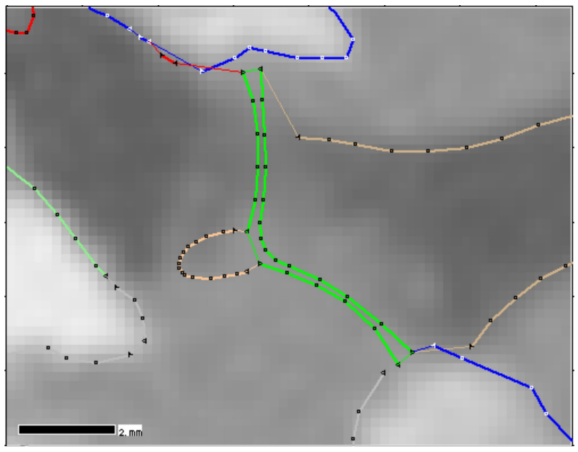

Slice 4 (#23)

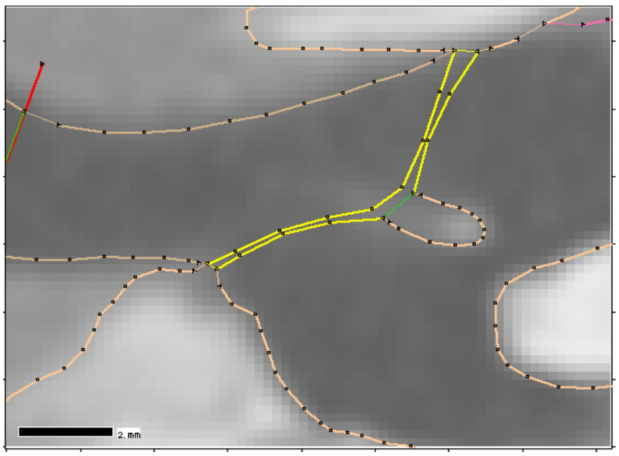

Slice 4 (#37)

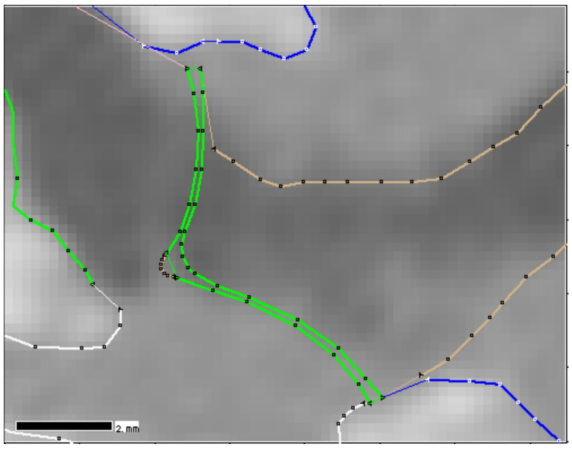

Slice 5 (#24)

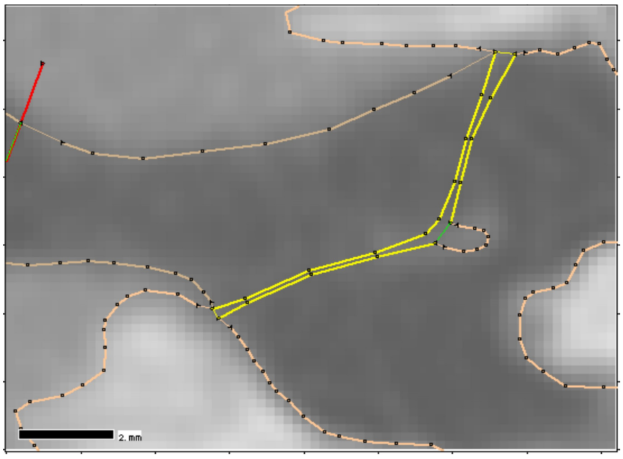

Slice 5 (#38)

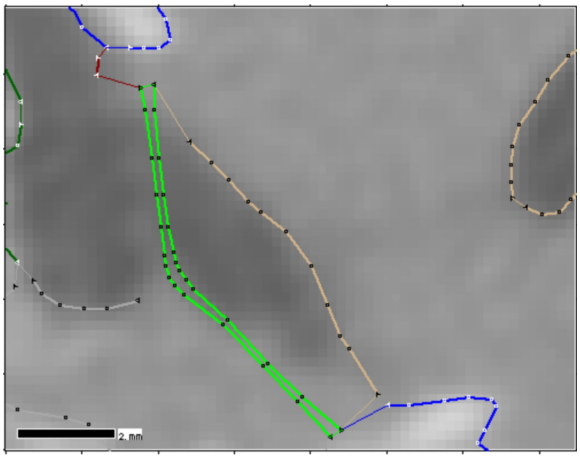

Slice 6 (#25)

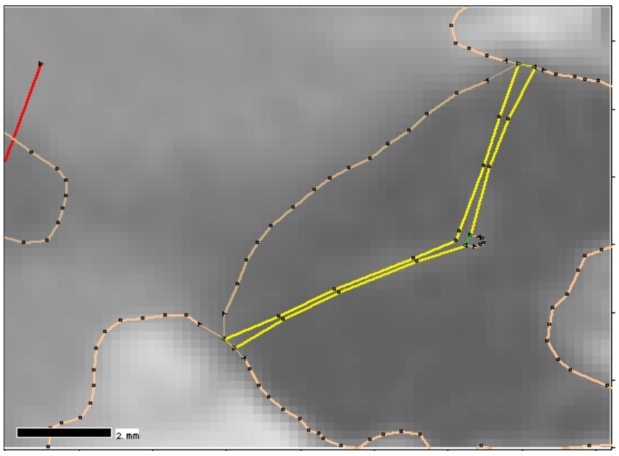

Slice 6 (#39)

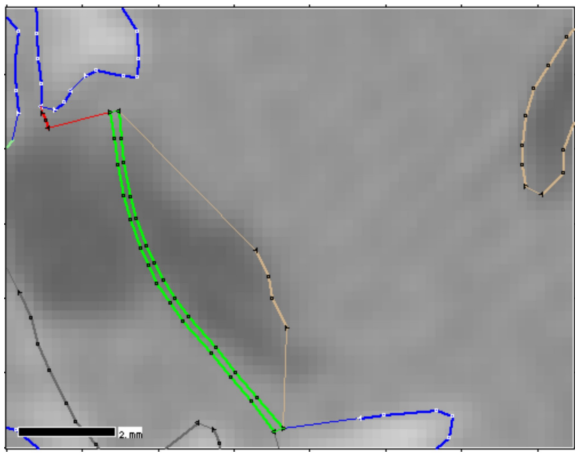

Slice 7 (#26)

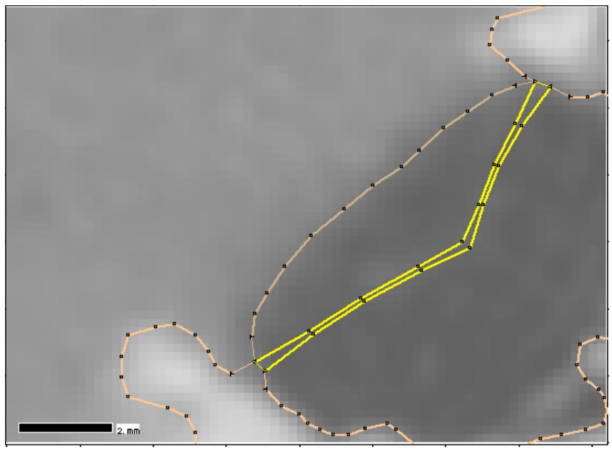

Slice 7 (#40)

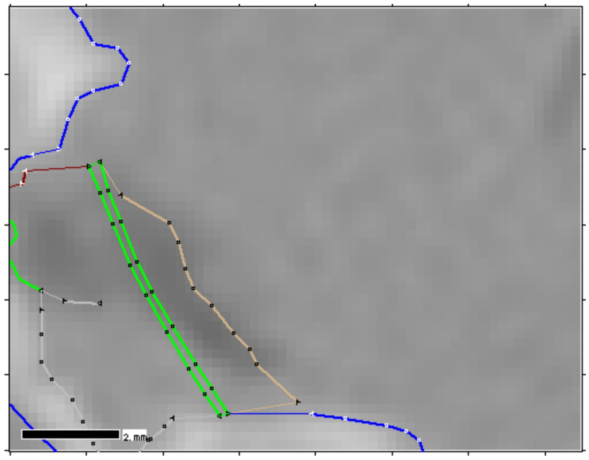

Slice 8 (#27)

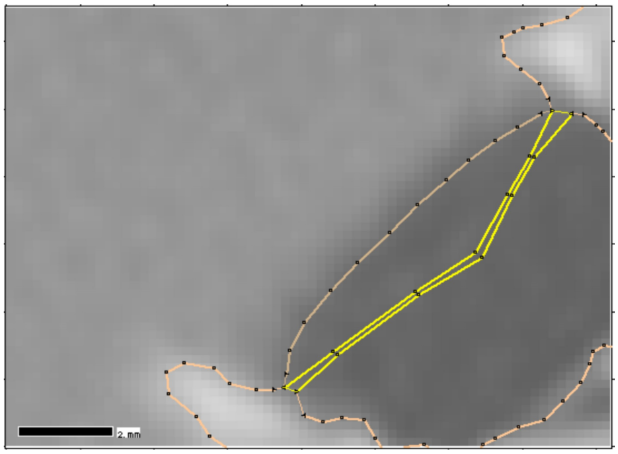

Slice 8 (#41)

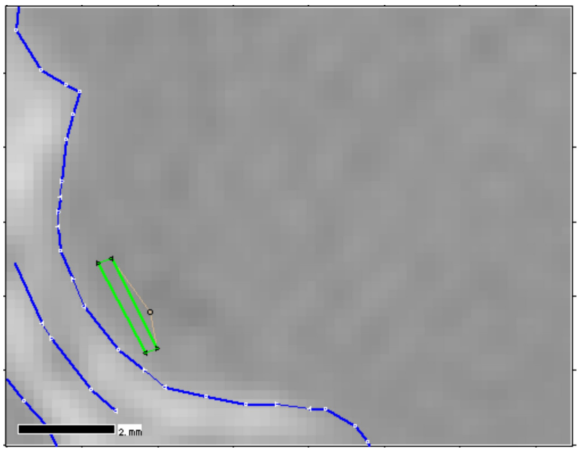

Slice 9 (#28)

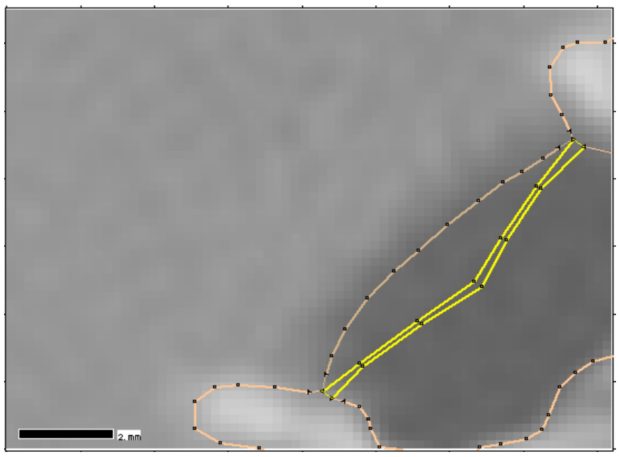

Slice 9 (#42)

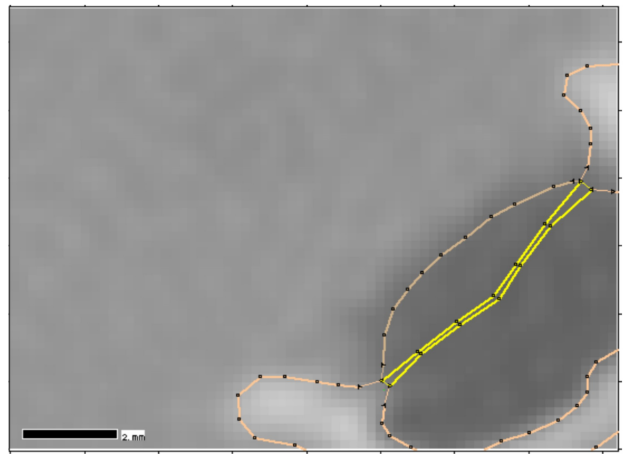

Slice 10 (#43)

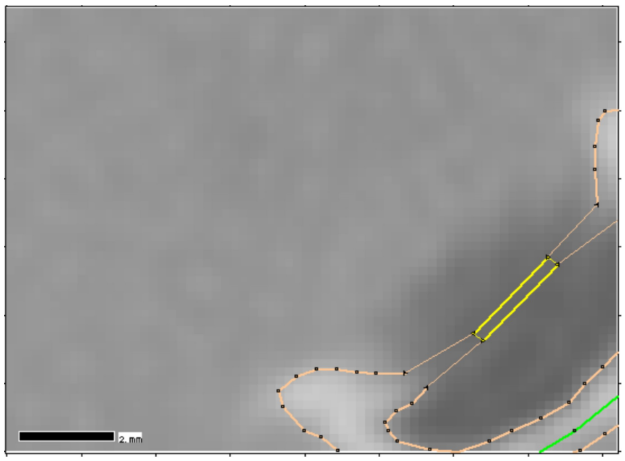

Slice 11 (#44)

Figure 5.5: Comparison of the TM in 1-day-old model and 22-day-old model in terms of thickness and curvature.
The segmentation related to the TM is shown by green lines for the 1-day-old model and by yellow lines for the 22-day-old model. The CT scan of the 1-day-old model shows the left ear, while the CT scan of the 22-day-old model shows the right ear. The first number for each slice is related to the number of slices in this figure, and the second number (after '#') gives the number of the slice in Fie.

5.4 Static displacement for distinct nodes

In this section the static displacements are shown for five different nodes on different components of the 1-day-old model. A node on the posterior part of the TM was chosen where the static displacement was maximum. Another node was chosen on the anterior part of the TM, where a local maximum displacement is located. The TM is attached on its medial side to the manubrium, and experimental measurements are normally done on the lateral surface of the TM

at the umbo region. Therefore, a node was selected on the lateral side of the TM at the umbo. The selected incus node corresponds to the location where the spring is attached to the long process of the incus, in order to represent the displacement of the stapes. The PF node was chosen approximately in the middle of the PF.

The static displacements for the five mentioned nodes are 416, 306, 36.7, 17.2 and 0.118 nm/Pa, respectively (Figure 5.6). The displacements decrease progressively from the PT to the umbo and incus. The displacements on the PF are very small.

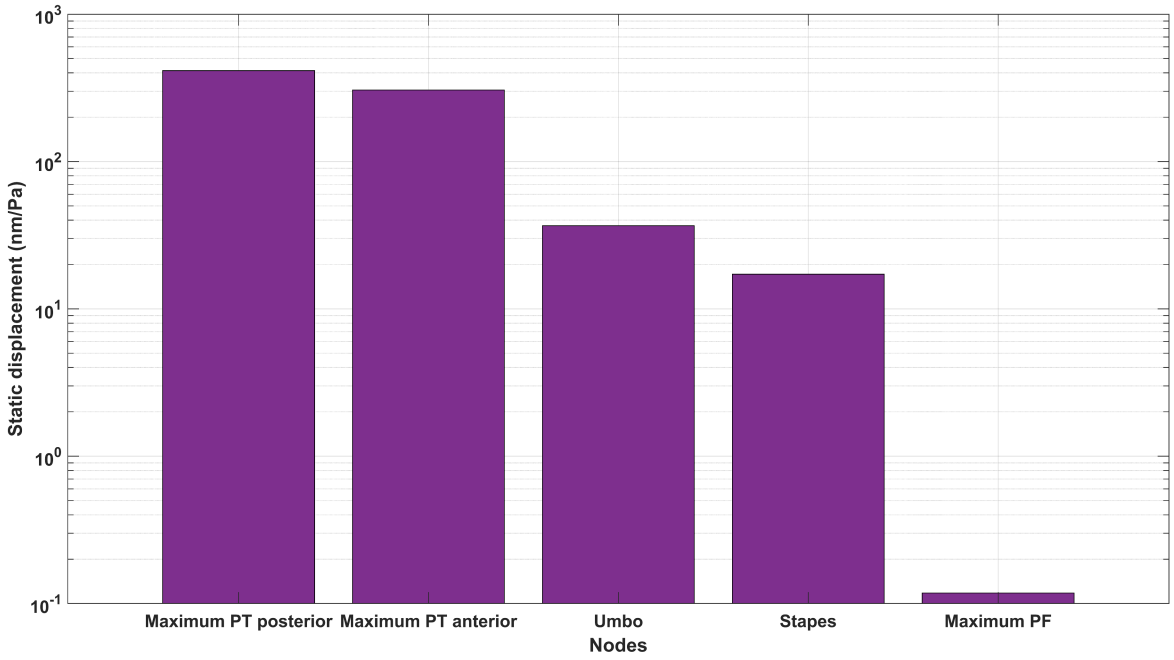

Figure 5.6: Comparison of static displacements of the PT posterior point, PT anterior point, umbo, stapes (represented by a point on the incus), and middle of the PF.

5.5 Low-frequency tympanic-membrane vibration pattern

With the material properties discussed in Chapters 3 and 4, we defined a baseline model for a 1-day-old simulation. When the model is exposed to the step-function load, after passing through a transient response it reaches a long-term condition that corresponds to the low frequencies in the frequency response, meaning the magnitude of the frequency response at the lowest frequencies is equal to the final magnitude of displacement in the time domain. As discussed in Chapter 3, vibration pattern measurements in adults indicate that the largest displacements occur in the posterior region of the PT and a simple vibration pattern is observed at low frequencies.

Figure 5.7 shows displacement magnitude maps for the baseline model of the 1-day-old middle at 1 s, with the magnitude normalized by the applied sound pressure amplitude of 1 Pa, both with and without colour smoothing. The figure shows the medial view. The maximum displacement is seen in the posterior area of the PT, where the manubrium is farther from the TM boundary and the TM is thinner. There is a smaller local maximum in the anterior region of the PT.

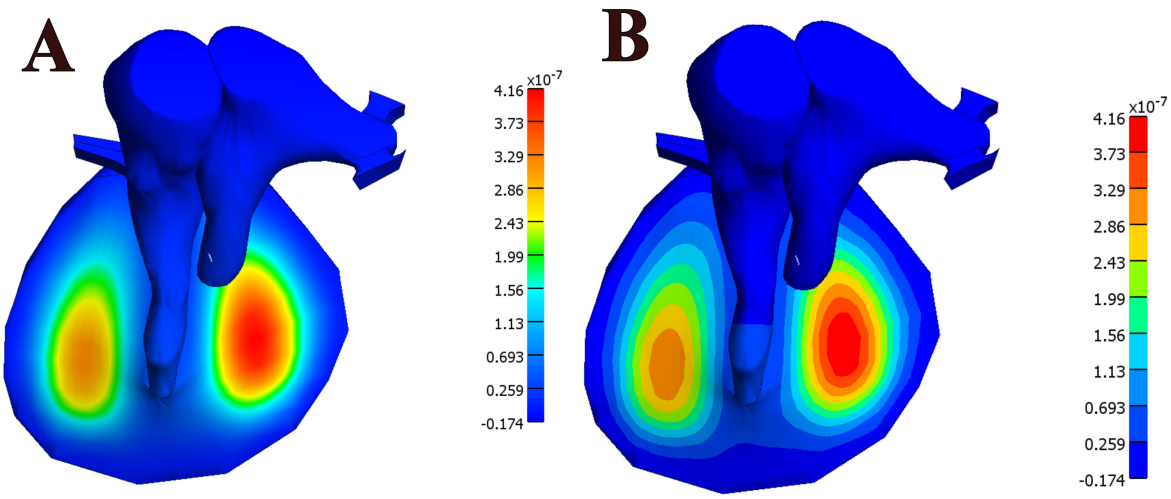

Figure 5.7: Medial view of displacement patterns of the 1-day-old middle ear model. (A) With colour smoothing. (B) Without colour smoothing. The displacement magnitude is normalized by the amplitude of the applied sound pressure. The colour bars indicate the displacement magnitude, with the lowest displacements shown in blue and the highest in red. The largest displacement happened in the posterior portion of the PT. A local displacement maximum can also be seen on the anterior side of the PT.

The posterior part of the 1-day-old model experiences the largest static displacement with a displacement value of 416 nm/Pa. Figure 5.8 shows the displacement-magnitude map at 100 Hz for the 22-day-old model of the middle ear developed by Motallebzadeh et al. (2017a). (Note that the model of Motallebzadeh et al. (2017a) was for a right middle ear, and our model is for a left middle ear.) Figure 5.8 shows that the maximum displacement also occurs in the posterior region of the PT in the 22-day-old model, and a smaller local maximum displacement can again be seen in the anterior region of the PT, as in our 1-day-old model. As shown in Figure 5.8, the maximum displacement of the 22-day-old model of Motallebzadeh et al. (2017a) was 500 nm/Pa at 100 Hz.

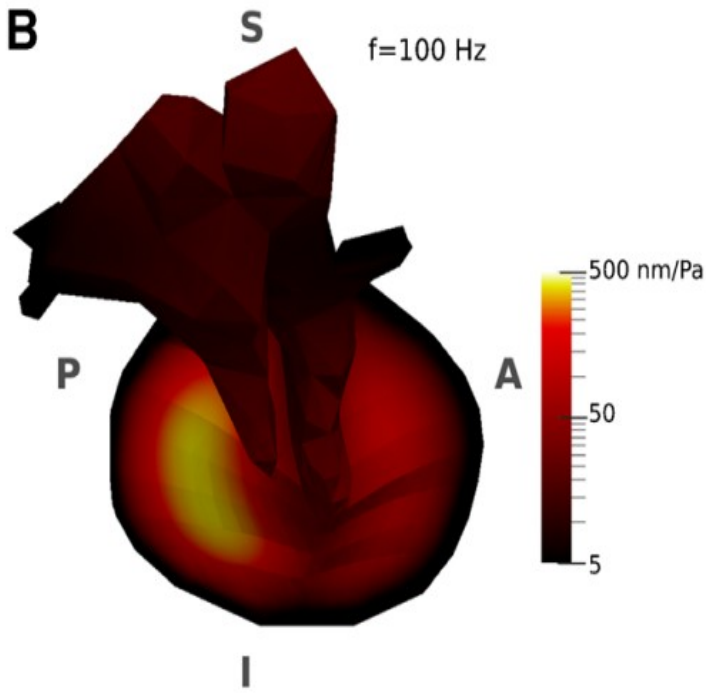

Figure 5.8: Medial view of the magnitude of displacement for the 22-day-old middle ear model of Motallebzadeh et al. (2017a) in response to sound pressure at 100 Hz. Since some components of the model (e.g., ossicles) have small displacements, the displacement maps are presented on a logarithmic scale. The colour scale indicates displacement values with monotonically increasing brightness, where maximum displacement is white and minimum displacement is black. TM displacements are greatest in the posterior portion, and there is a smaller local maximum in the anterior region

5.6 Time-domain and frequency-domain responses

Figure 5.9 shows the time-domain dynamic responses of the five selected nodes in the 1-day-old model. We can see in the figure that the damping of the initial transient response in the posterior and anterior PT is much less than on the umbo, incus (stapes) and PF.

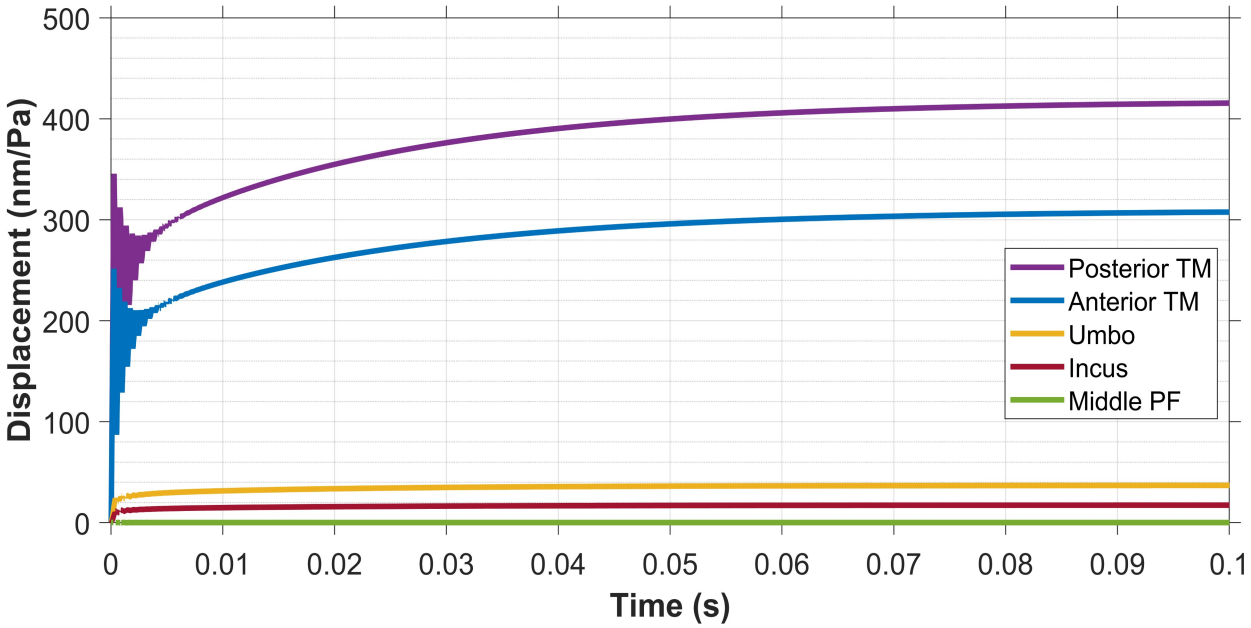

Figure 5.9: Dynamic response in the time domain for five different locations of the 1-day-old model.

The frequency responses from 6.5 Hz to 10 kHz for the same five locations in the baseline model, computed from the time-domain responses of Figure 5.9, are presented in Figure 5.10. The posterior and anterior regions of the PT have peaks at 1.8 and 2.0 kHz, respectively, with magnitudes of 1094 and 864 nm/Pa. The umbo and incus both show a peak and a shoulder, corresponding to the two PT peaks. (Recall that the displacement of the node on the incus represents the displacement of the stapes.) The magnitudes of the umbo peak and shoulder are 28 and 16 nm/Pa, respectively, and the magnitudes of the incus peak and shoulder are 12 and 7 nm/Pa, respectively.

The centre of the PF shows a local minimum at about 500 Hz with a magnitude of 0.024 nm/Pa, and then a resonance frequency of 1.87 kHz with a magnitude of 2.42 nm/Pa.

The posterior PT, anterior PT, umbo, incus and middle PF all have very small phase lags up to about 300 Hz. The PT anterior and posterior movements are almost in phase with each other until about 1.6 kHz, while the umbo and incus movements are almost in phase with each other until about 2.3 kHz. The phase of the PF beyond 300 Hz is mostly much more negative than the phases of the other regions.

The displacement magnitudes decrease slowly for frequencies above the minimum value of 6.5 Hz. The magnitudes at 100 Hz for the posterior PT, anterior PT, umbo, incus and middle PF are 237 nm/Pa, 175 nm/Pa, 25 nm/Pa, 11 nm/Pa and 0.092 nm/Pa, respectively. After their resonance peaks, the magnitudes of the anterior and posterior regions of the PT roll off and are slightly different, with small peaks and troughs occurring at different frequencies. The frequency responses of the umbo and incus are similar in shape until about 2.5 kHz. The displacement magnitude on the incus is higher than that of the middle of the PF up to about 2.5 kHz.

In the range of 100 Hz to 10 kHz the umbo magnitude is larger than that of the incus except from 3 to 3.2 kHz and from 8.2 to 8.6 kHz, where the umbo exhibits the lower magnitude. A minimum at 7.5 kHz with a magnitude of 0.03 nm/Pa occurs on the incus. A local minimum of the umbo response occurs at 6.3 kHz with a magnitude of 0.21 nm/Pa. The lowest magnitude happens at the umbo at 8.4 kHz with a magnitude of 0.006 nm/Pa.

The PF response shows a peak between the resonance frequencies of the anterior and posterior parts of the PT, and closer to the anterior PT resonance frequency, with a value of 1.89 kHz and a magnitude of 2.4 nm/Pa.

The posterior PT and anterior PT in the model show full widths at half maximum (FWHM) of 0.523 kHz and 0.511 kHz, respectively. This value, which is a measure of damping, is equal to 0.537 kHz in the centre of the PF. Resonance peaks are sharper and narrower for lower damping, so the FWHM is smaller, while for heavy damping the resonance peak is low and wide so the FWHM is larger.

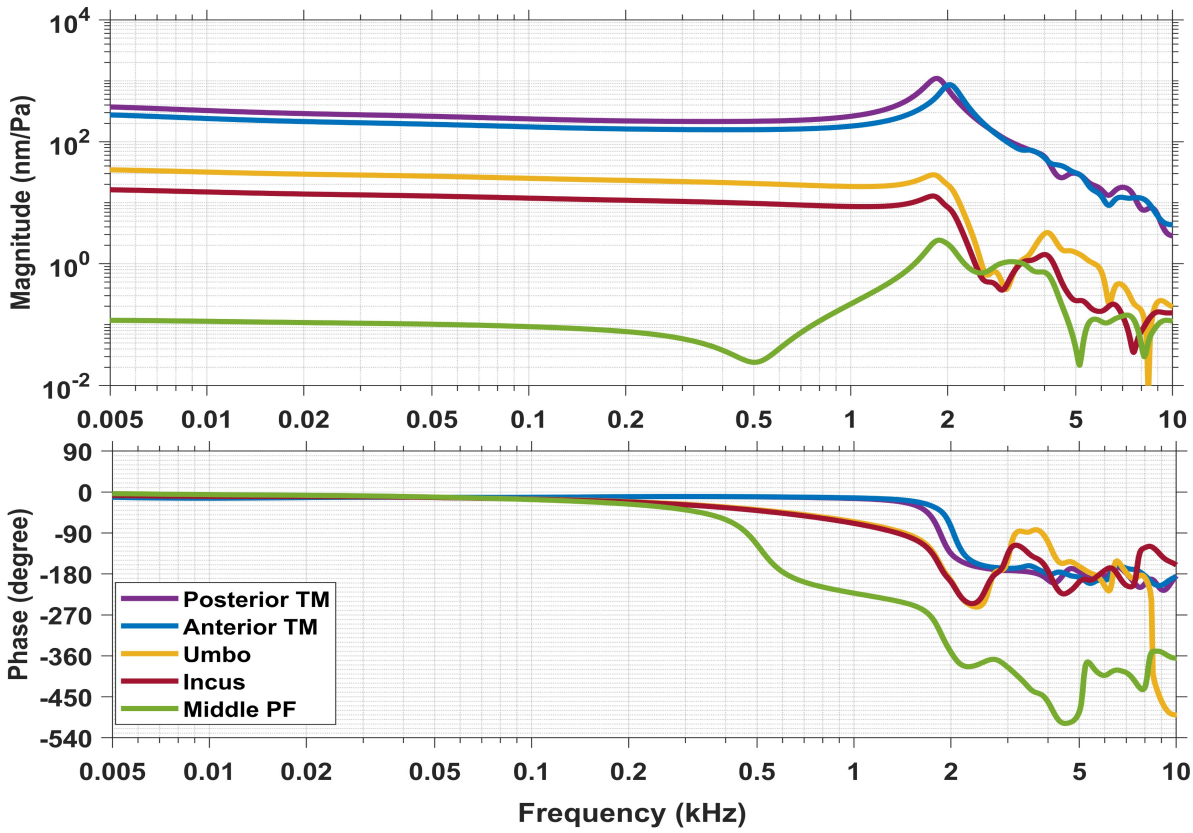

Figure 5.10: Frequency responses of five different regions of 1-day-old model. Regions include posterior PT, anterior PT, umbo, incus, and centre of PF.

5.7 Parameter sensitivity analysis

In order to determine how parameter values impact model behaviour, a sensitivity analysis was performed. The model parameters were changed one at a time by ±10 %, ±20 %, and ±40 % from their baseline values. The figures in this section showing the response changes associated with changes in the parameters of each model structure (PT, PF, ligaments, malleus and incus) are all depicted with the same colour scheme (e.g., red for PT and blue for PF). A unique symbol is used for each type of parameter in all structures (e.g., '△' for Young's modulus). For each of the PT, PF, ligaments (including the AML and the two parts of the PIL), malleus and incus, three parameters are included: Young's modulus, bulk modulus and mass density. (As discussed in Section 4.10, the bulk modulus is used instead of Poisson's ratio to avoid the difficulties that arise from the upper limit of 0.5 for the Poisson's ratio.) For the discrete spring and damper, there is a single parameter each. For the Prony series, we use a single value applied to all five time constants for this sensitivity analysis.

The symbols on the horizontal line across the graphs represent the baseline values for the model. The filled symbols indicate a parameter increase (+10%, +20% and +40%), while the open symbols indicate a parameter decrease (−10%, −20% and −40%). We depict the baseline values with filled symbols. Figure 5.11 shows the variations in the response of the maximum TM displacement magnitude at a low frequency (100 Hz) when the model parameters were changed by ±10 %,±20 %, and ±40 %. In decreasing order of significance, the most influential parameters are the Young's modulus of the PT, the Prony coefficients, and the bulk modulus of the PT. The other parameters have negligible effects of less than 4 nm/Pa.

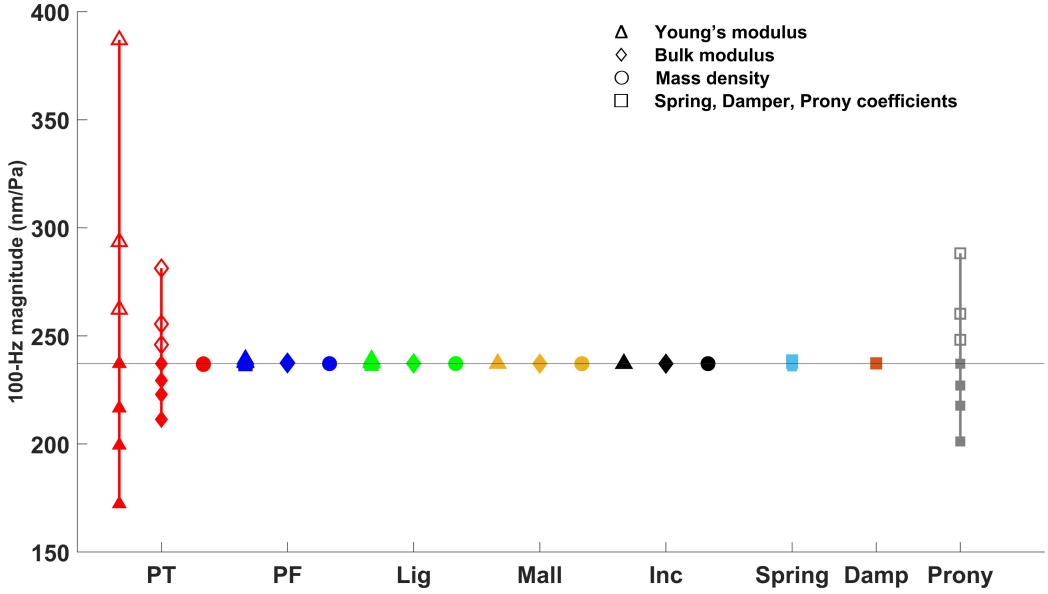

Figure 5.11: Changes in the maximum TM displacement magnitude at a low frequency (100 Hz) when the model parameters were changed by ±10%, ±20% and ±40%. PT = pars tensa, PF = pars flaccida, Lig = ligaments, Mall = Malleus, Inc = Incus, Spring, Damp = damper, Prony = Prony coefficients. Variations in parameters within each of these groups are shown in the same colour. Across all structures, each parameter is represented by a unique symbol as shown in the legend. In the case of parameters being increased by 10%, 20% and 40%, the symbols are filled, and when the parameters are decreased by 10%,20% and 40%, the symbols are open. The baseline values are shown with filled symbols on the horizontal line with a magnitude of 237.16 nm/Pa.

Figure 5.12 shows the variations in the response of the umbo displacement magnitude at a low frequency (100 Hz) when the model parameters were changed by ±10 %,±20 %, and ±40 %. From most significant to least significant, the most influential parameters are the Prony

coefficients, ligament Young's modulus, PT Young's modulus, spring coefficient, PF Young's modulus, and PT bulk modulus. All other parameters have effects of less than 0.4 nm/Pa.

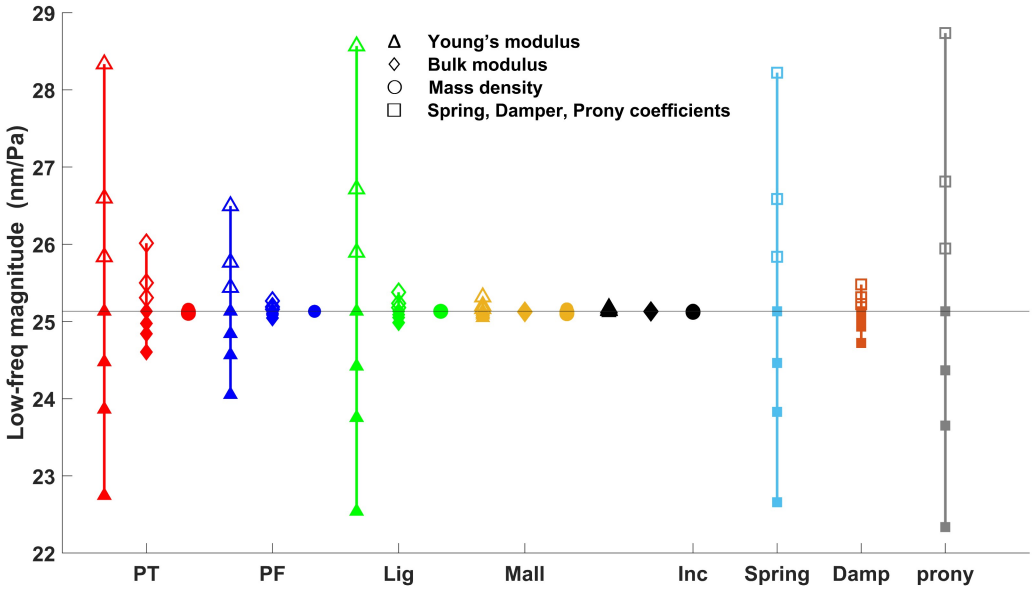

Figure 5.12: Changes in the umbo displacement magnitude at a low frequency (100 Hz) when the model parameters were changed by ±10%, ±20% and ±40%.
Abbreviations, symbols and colours are the same as in Figure 5.11. The baseline values are shown with the filled symbols on the horizontal line with a magnitude of 25 nm/Pa.

Figure 5.13 shows the relationship between the parameter variations and the shifts in the middle-ear resonance frequency. (The resonance frequency is identical for the TM node and the umbo node, so we refer to that as the middle-ear resonance.) In our simulations, the frequency resolution is 6.5 Hz. Therefore, frequency changes that are less than this value are not captured, and the frequency changes which are shown in the plot are multiples of 6.5 Hz. As shown in the figure, from most significant to least significant, the most influential parameters are the mass density of PT, Young's modulus of PT, the Prony coefficients, and the bulk modulus of PT.

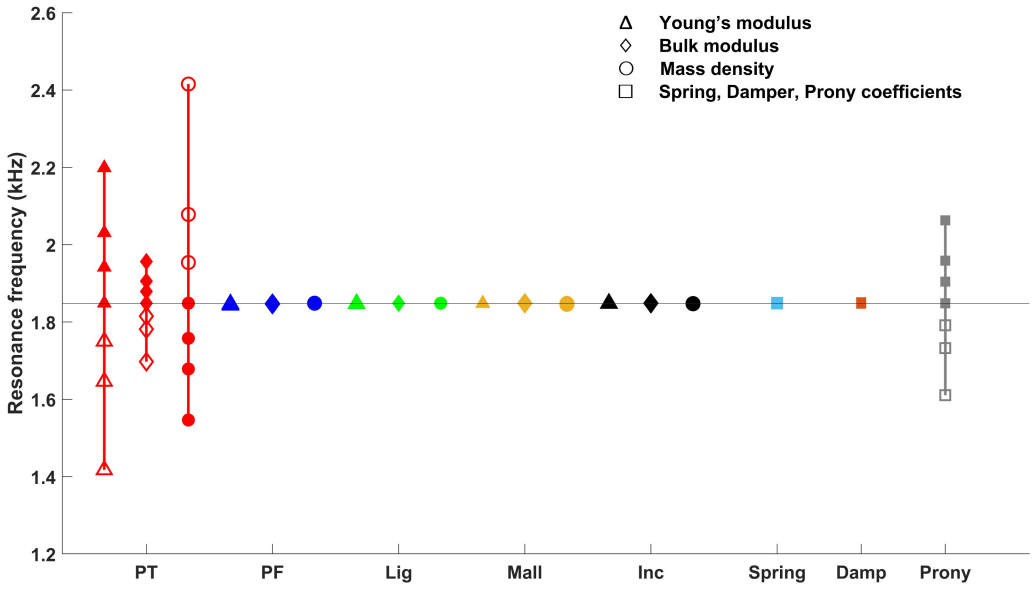

Figure 5.13: Changes in the middle-ear resonance frequency when the parameters of the model were changed ±10%, ±20% and ±40%.
Abbreviations, symbols and colours are the same as in Figure 5.11. The baseline values are shown with the filled symbols on the horizontal line with a magnitude of 1.84 kHz.

Figure 5.14 shows the variations in the magnitude of the maximum TM displacement at the resonance peak when the model parameters were changed by ±10 %,±20 %, and ±40 %. In decreasing order of significance, the most influential parameters are Young's modulus of the PT, the Prony coefficient, and the bulk modulus of the PT. This order of significance is almost the same as in Figure 5.11, which shows the variation in the response of the maximum TM magnitude at 100 Hz.

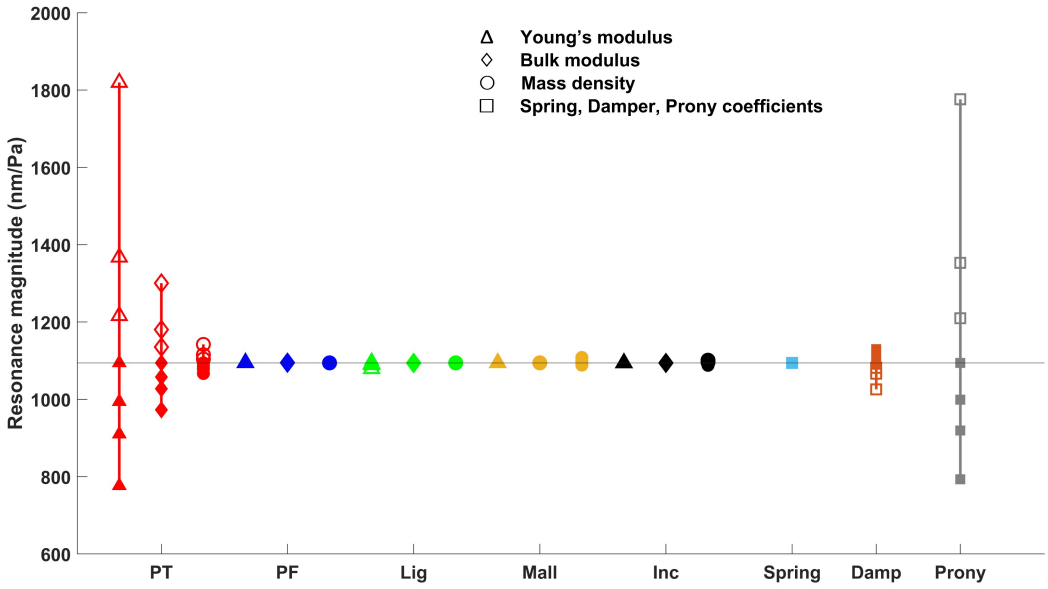

Figure 5.14: Changes in the maximum TM displacement magnitude of the resonance peak when the parameters of the model were changed ±10%, ±20% and ±40%. Abbreviations, symbols and colours are the same as in Figure 5.11. The baseline values are shown with the filled symbols on the horizontal line with a magnitude of 1094.3 nm/Pa.

Figure 5.15 shows the variations in the displacement magnitude of the umbo at the resonance peak when the model parameters were changed by ±10%, ±20% and ±40%. The most influential parameters in decreasing order of importance are the damper coefficient, the Prony coefficients, Young's modulus, the mass density, the bulk modulus of the PT, and Young's modulus of the ligaments.

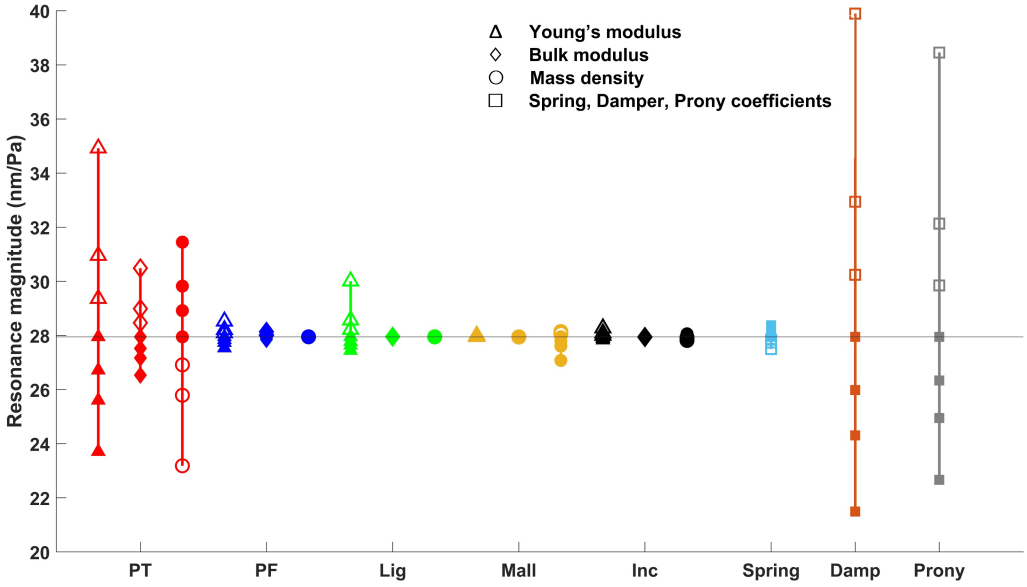

Figure 5.15: Changes in the umbo displacement magnitude at the resonance peak when the parameters of the model were changed ±10%, ±20% and ±40%.
Abbreviations, symbols and colours are the same as in Figure 5.11. The baseline values are shown with the filled symbols on the horizontal line with a magnitude of 27.95 nm/Pa.

The results of figure 5.11 to 5.15 show that the Young's modulus and bulk mosulus of the PT and the Prony coefficients substantially affect all five features of the response.

For the rest of this sensitivity analysis we focus on the ten parameters which showed substantial effects in any of Figures 5.11 to 5.15, and plot the results in a format that takes more space but shows the trends more intuitively. In the following figures, the horizontal positions of the different magnitude or frequency values for each parameter are located at the values −10%, −20%, −40%, baseline, +10%, +20% and +40%, on locally linear scales, where 0 corresponds to the baseline value of the parameter and the other values represent the scaling of the parameter.

Figure 5.16 shows the sensitivity analysis of the ten selected parameters for the maximum low-frequency magnitude for the TM. As mentioned earlier, Young's modulus of PT, the Prony coefficients and the bulk modulus of the PT all contribute significantly to changing the low-frequency magnitude, in decreasing order of importance. The effect of decreasing each of the three parameters by 40% is greater than increasing them by 40%. As can be seen, lowering the PT Young's modulus by 40% has the greatest effect in changing the magnitude at low frequencies. Reducing it by 40% has a 2.3 times larger effect on the low-frequency magnitude

than increasing it by 40%. The ratios of the 40% decrease to the 40% increase for the bulk modulus and the Prony coefficient are 1.7 and 1.4, respectively. Changing the Prony coefficient, which is the second most important factor affecting the low-frequency magnitude of the TM after Young's modulus, has a slightly greater effect on the low-frequency magnitude than do bulk modulus changes. When a parameter is changed by 10% from the baseline model, the magnitude at low frequencies changes by almost as much as when it is changed from 20% to 10%. This happens for all three parameters (Prony coefficient, and Young's modulus and bulk modulus of the PT). When there is a decrease to −40% from −20% in the parameters, the effect on the low-frequency magnitude is not linear anymore. For example, for Young's modulus of the PT, the difference between the low-frequency magnitude values when the parameter is decreased from −20% to −40% is more than three times the difference when decreasing from −10% to −20%. This value equals 2.3 and 2.6 for the Prony coefficient and bulk modulus, respectively.

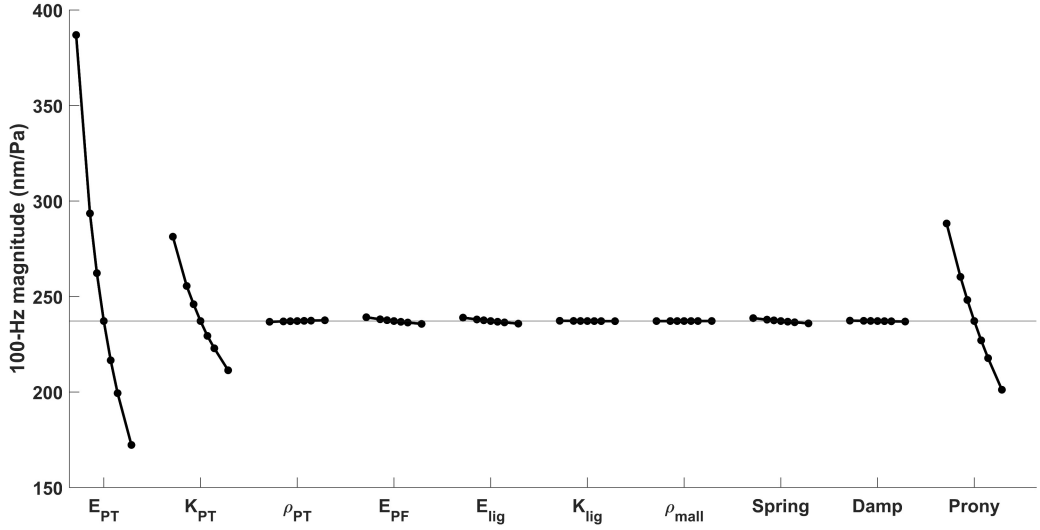

Figure 5.16: Changes in the TM displacement magnitude at a low frequency (100 Hz) when selected parameters of the model were changed by ±10%, ±20% and ±40%.

Figure 5.17 shows the sensitivity analysis of the low-frequency umbo response for the ten selected parameters. As mentioned for Figure 5.12, the most influential parameters are the Prony coefficients, ligament Young's modulus, PT Young's modulus, spring coefficient, PF Young's modulus, and PT bulk modulus, from most significant to least significant. It appears that the curve for PT bulk modulus has more curvature than the other curves. Both the damping

coefficient curve and the ligament bulk modulus curve also have higher curvatures than the other parameters.

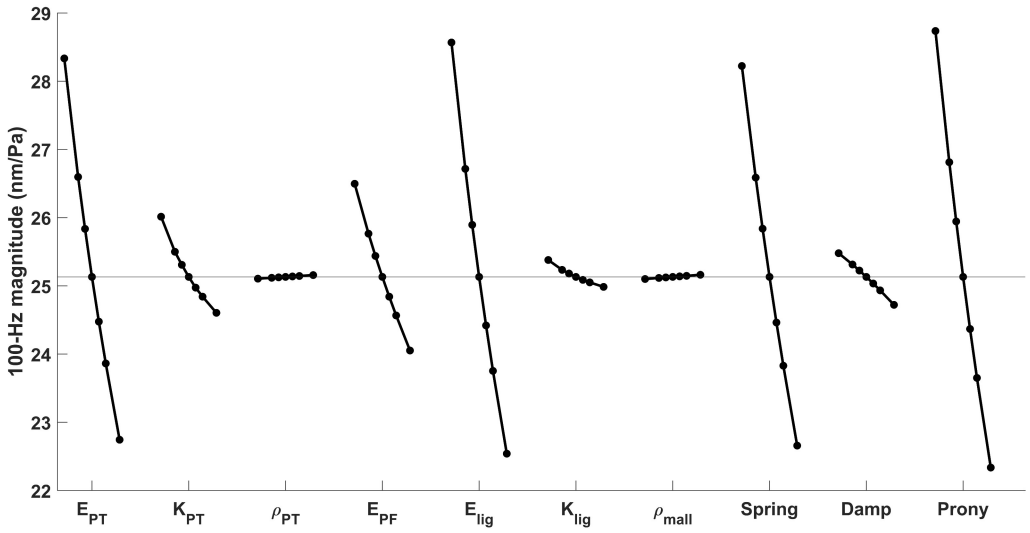

Figure 5.17: Changes in the umbo displacement magnitude at a low frequency (100 Hz) when selected parameters of the model were changed by ±10%, ±20% and ±40%.

Figure 5.18 shows the sensitivity analysis of the ten selected parameters for the resonance frequency of the middle ear. The most influential parameters, from most significant to least significant, are the mass density of PT, Young's modulus of PT, the Prony coefficients, and the bulk modulus of PT. We can see that all the parameters except mass density of the PT and malleus have negative slopes.

For the bulk modulus of the PT and the Prony coefficient, the 40% increase and 40% decrease have almost the same effect on the resonance frequency of the middle ear. Decreasing the mass density of the PT by 40% has almost twice as much effect on the resonance frequency as increasing by the same percentage.

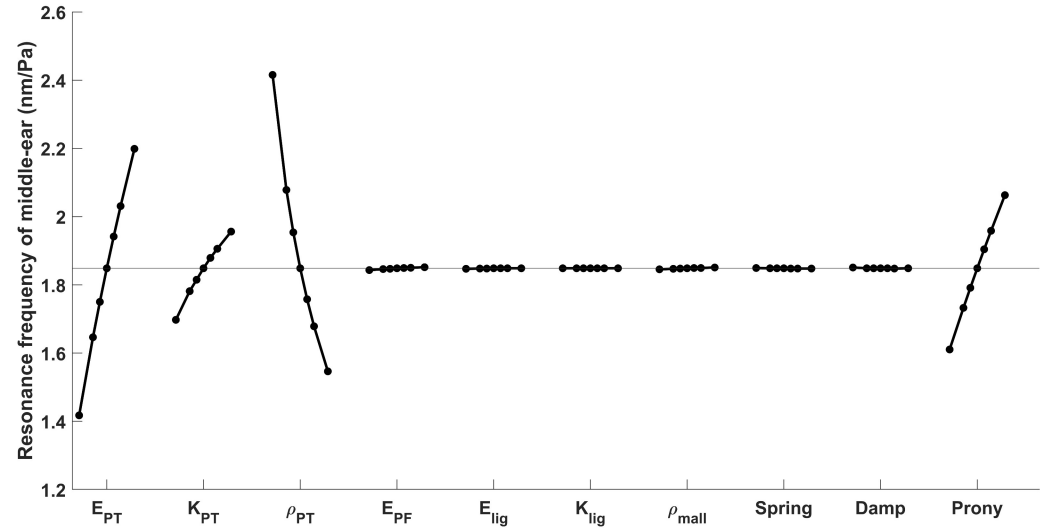

Figure 5.18: Changes in the middle-ear resonance frequency when selected parameters of the model were changed by ±10%, ±20% and ±40%.

Figure 5.19 shows the impact of the ten selected parameters on the resonance magnitude of the TM. From most significant to least significant, the most influential parameters are PT Young's modulus, the Prony coefficients, and PT bulk modulus. Again, reductions by 40% have larger effects than increases by 40%.

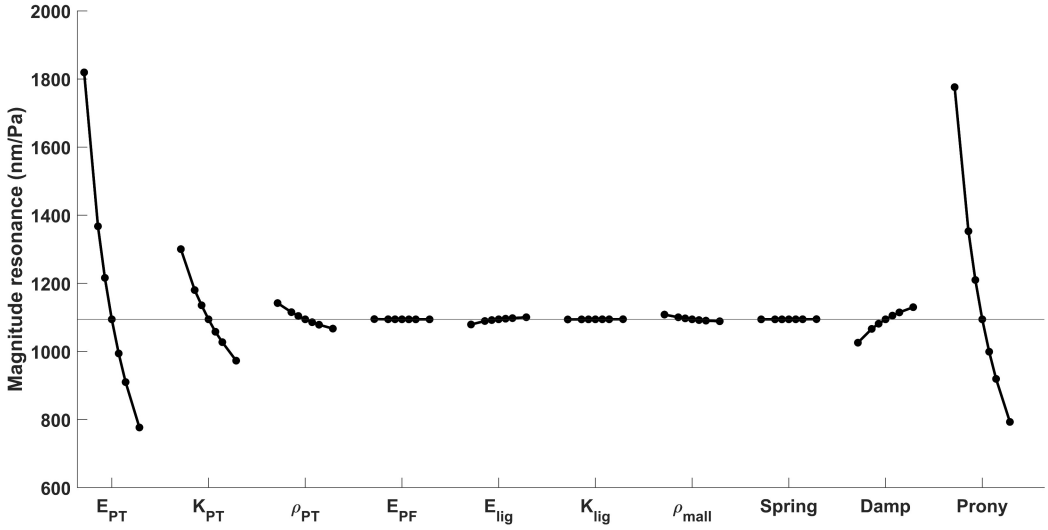

Figure 5.19: Effects of selected parameters on the resonance magnitude of the TM when selected parameters of the model were changed by ±10%, ±20% and ±40%.

Figure 5.20 shows the influence of the ten selected parameters on the umbo resonance magnitude. As mentioned earlier, the most influential parameters in decreasing order of importance are the damper coefficient, the Prony coefficients, Young's modulus, the mass density, the bulk modulus of the PT, and Young's modulus of the ligaments. The curves for the Young's modulus of the ligaments and the mass density of the malleus show particularly strong curvatures.

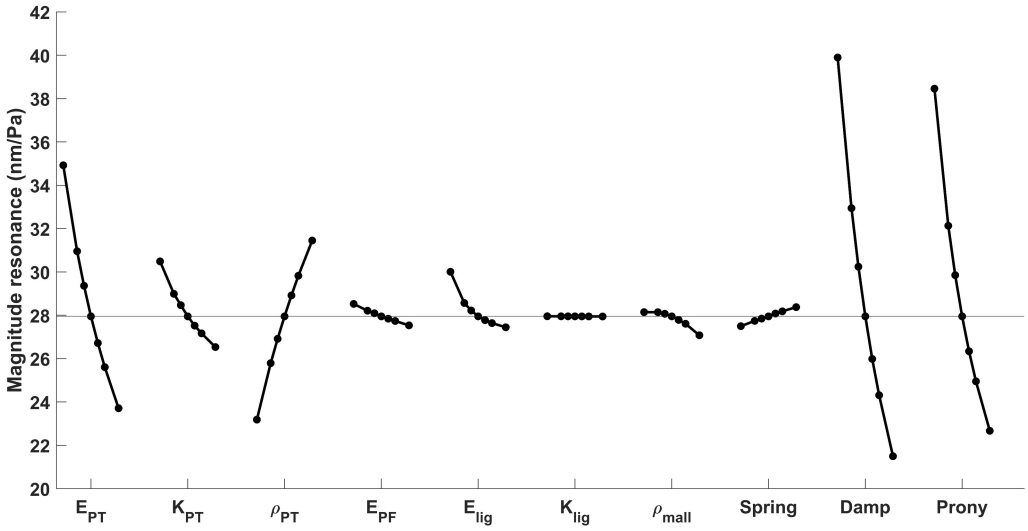

Figure 5.20: Effects of selected parameters on the resonance magnitude of the umbo when selected parameters of the model were changed by ±10%, ±20% and ±40%.

5.8 Sensitivity analysis of individual Prony coefficients

For our baseline model, the five Prony coefficients were all set to 0.5. Each of these Prony coefficients has a different effect on the response of the middle ear, which is discussed in the following sensitivity analysis.

Figure 5.21 shows the effects of the five Prony coefficients on the low-frequency (100 Hz) magnitude for the TM. The g_4 and g_5 Prony coefficient have much greater effects on the low-frequency magnitude of the TM than the other Prony coefficients. This is reasonable since the g_4 and g_5 coefficients are associated with the low-frequency time constants τ_4=0.00159 s and τ_5=0.0159 s, corresponding to 100 Hz and 10 Hz, respectively.

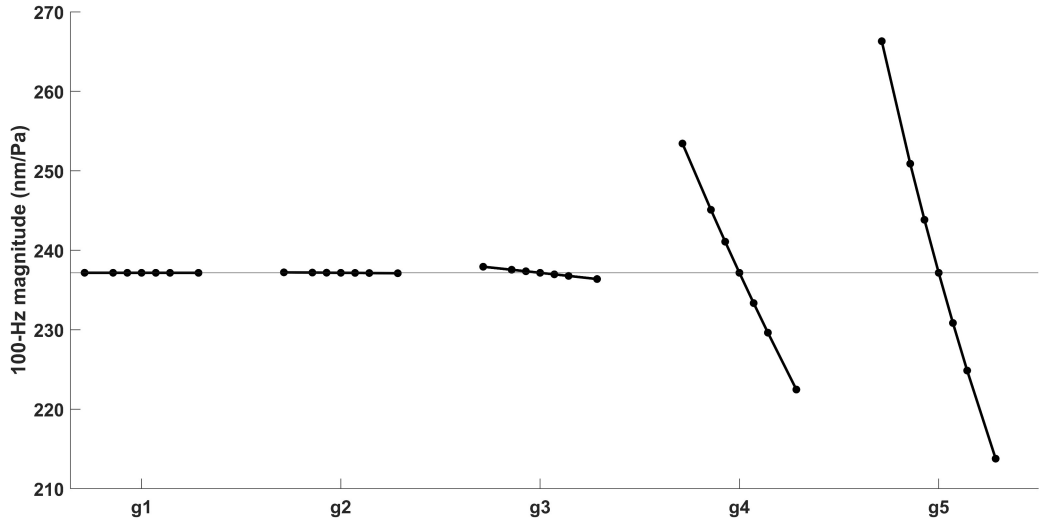

Figure 5.21: Effects of individual Prony coefficients on low-frequency magnitude (100 Hz) of the TM when they were changed by ±10%, ±20% and ±40%.

Figure 5.22 shows the effects of the Prony coefficients on the low-frequency magnitude of the umbo response. The effects are similar to those in Figure 5.21.

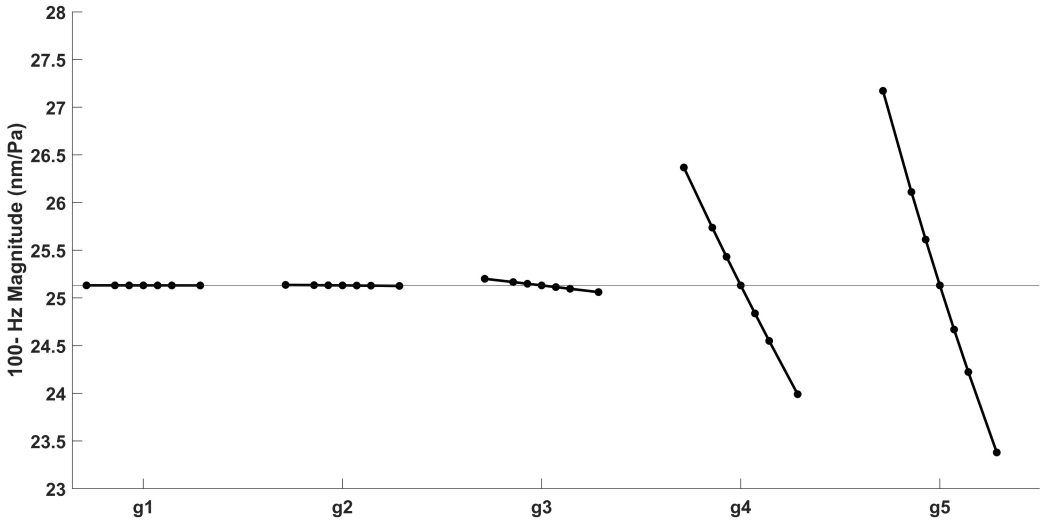

Figure 5.22: Effects of individual Prony coefficients on low-frequency magnitude (100 Hz) of the umbo response when they were changed by ±10%, ±20% and ±40%.

Figure 5.23 shows the effects of variation of the Prony coefficients on the middle-ear resonance frequency. The middle-ear resonance frequencies are affected by g_3 in addition to g_4 and g_5. The g_3 coefficient is related to the time constant τ_4=0.00159 s, corresponding to 1 kHz, not far from the baseline model resonance at around 1.8 kHz.

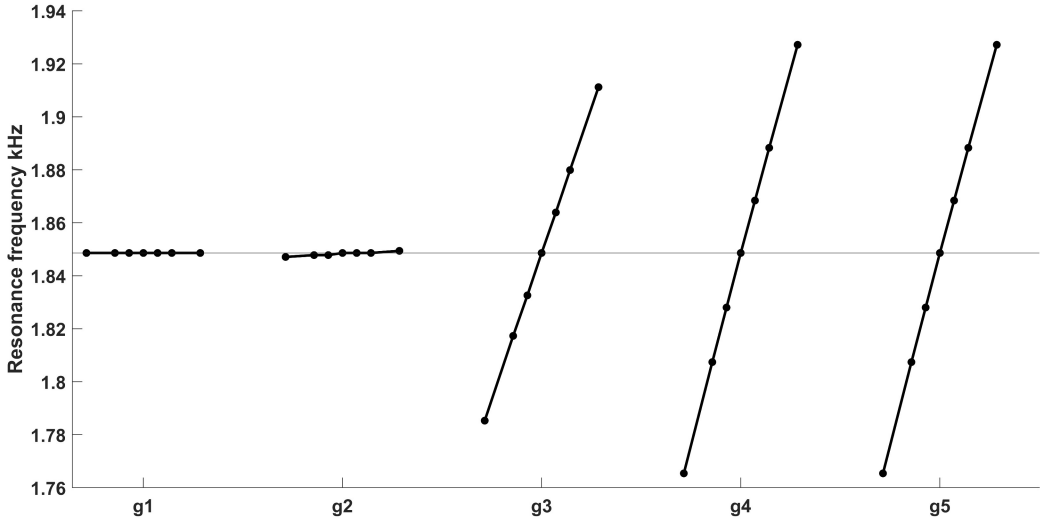

Figure 5.23: Effects of individual Prony coefficients on middle-ear resonance frequency when they were changed by ±10%, ±20% and ±40%.

Figure 5.24 shows the effects of the Prony coefficients on the resonance magnitude of the TM. We can see from the figure that g_3, g_2, and g_4, in decreasing order of significance, have substantial effects on the resonance magnitude. The g_2 Prony coefficient is associated with the frequency of 10 kHz. Reducing g_3 by 40% has more impact than increasing it by 40%.

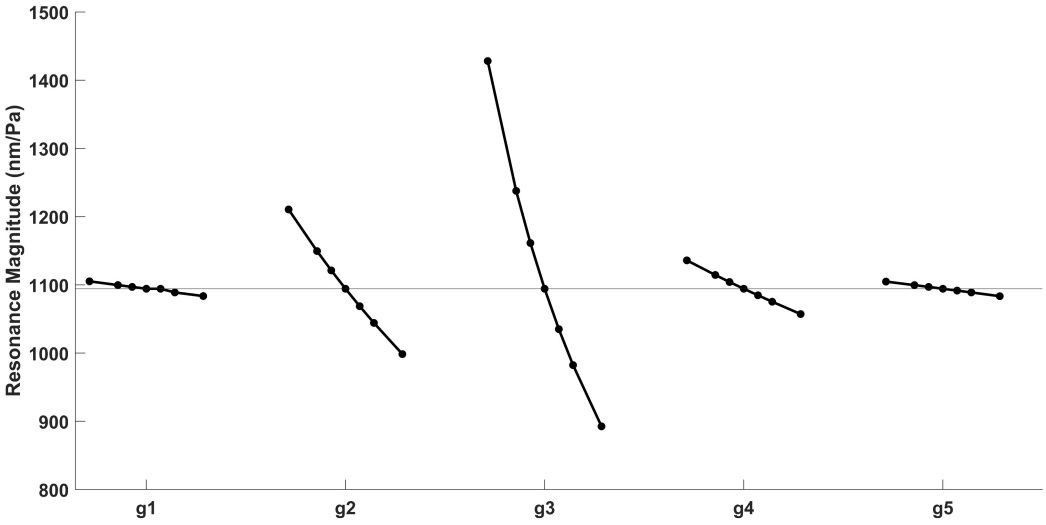

Figure 5.24: Effects of individual Prony coefficients on resonance magnitude of the TM when they were changed by ±10%, ±20% and ±40%.

Figure 5.25 shows the effects of the Prony coefficients on the resonance magnitude of the umbo response. The effects are very similar to those in Figure 5.24.

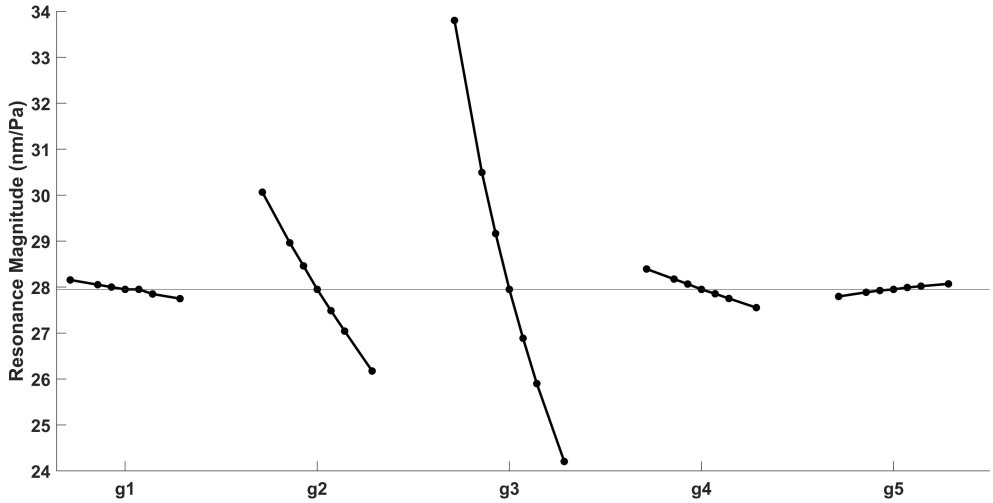

Figure 5.25: Effects of individual Prony coefficients on the resonance magnitude of the umbo when selected parameters of the model were changed by ±10%, ±20% and ±40%.

5.9 Comparison with 22-day-old model

5.9.1 Introduction

In this section, our results are compared with those for the previous 22-day-old model of Motallebzadeh et al. (2017b) and with the experimental data of Keefe & Levi (1996) and Pitaro et al. (2016). All of the mentioned comparison data are in the form of admittances, while our 1-day-old model response is in the form of point displacements. Since admittance is equal to the ratio of volume velocity to sound pressure, we convert the volume velocity to volume displacement for comparison with our model. This involves dividing the admittance magnitudes by $2\pi f$ and subtracting 90° from the admittance phase. The resulting volume displacements (in mm^3/Pa) are still only qualitatively comparable to our point displacements (in nm/Pa).

It is important to note that our model does not include the ear canal or the middle-ear air cavity, while both the 22-day-old model and the experimental data include them. The admittance due to the ear canal consists of two components: one due to the air in the canal and one due to the compliance of the canal wall. As a first stage, we compare the 22-day-old model response with a compliant canal wall and with a rigid canal wall in the frequency range of 100 Hz to 10 kHz in order to judge the effect of the ear-canal wall. We do not take into account the compliance of the air in the canal. In a second stage, we investigate the effect of the middle-ear cavity on the response of the 22-day-old model. In the end, we compare our 1-day-old response with that of the 22-day-old model and with the experimental data.

5.9.2 Effect of ear-canal wall

Figure 5.26 shows the differences in the volume displacement (calculated at the medial surface of the probe tip) with a compliant canal wall and with a rigid canal wall for the 22-day-old model. (Both responses include the middle-ear cavity.) We can see that the model shows almost identical magnitude results in both cases except for frequencies below around 1 kHz, where the compliant-wall magnitude is larger than the rigid-wall magnitude by up to 46.4%. (The difference in the height of the sharp peak at 5.9 kHz may be a numerical artefact.) Additionally, the two responses have almost the same phase, with some small differences below about 1 kHz and between 3.5 and 5.8 kHz.

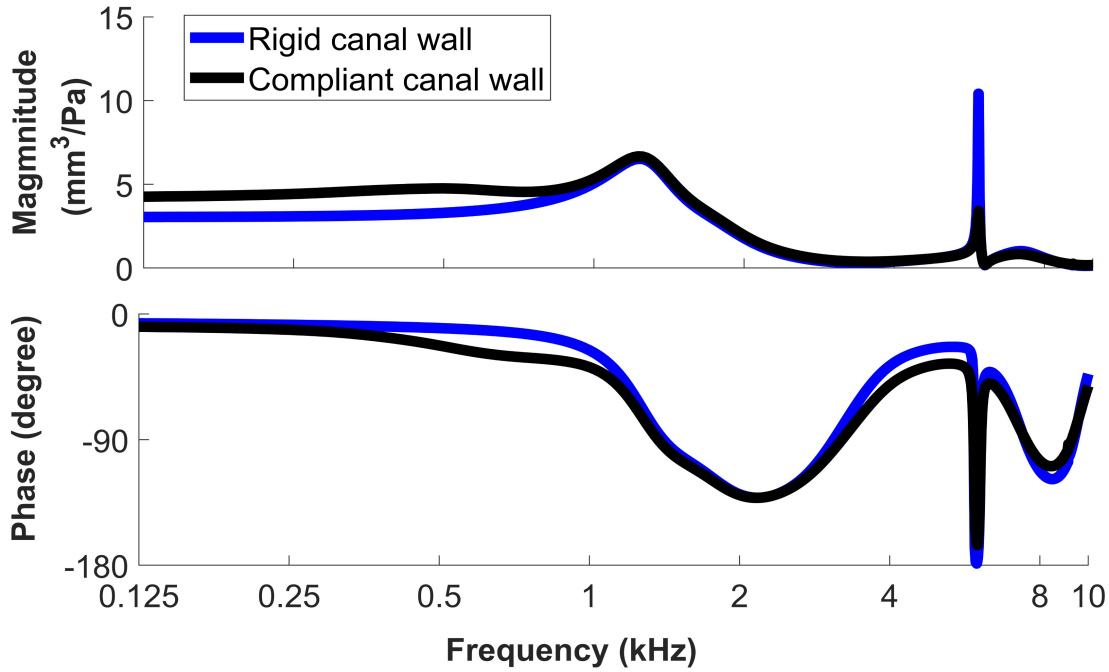

Figure 5.26: Volume displacement of 22-day-old model with ear-canal wall that is either rigid (blue curve) or compliant (black curve).
Volume displacement is computed at the medial surface of the probe tip.
Middle ear and middle-ear cavity are included in both of the model responses (After Motallebzadeh et al., 2017b)

5.9.3 Effect of middle-ear cavity

In Figure 5.27 we can see that the cavity causes significant differences in volume displacement magnitude up to around 2 kHz. The model without a cavity has a low-frequency magnitude that is higher by 46.1%; a higher resonance magnitude; and a resonance frequency that has shifted from 1.2 kHz to 1.05 kHz. An additional peak is also observed at 6.1 kHz for the model with a cavity. Both models show a low peak at around 7 kHz. The two responses have almost the same phase except for the range between 0.6 and 2 kHz, and in the vicinity of the 6.1-kHz peak.

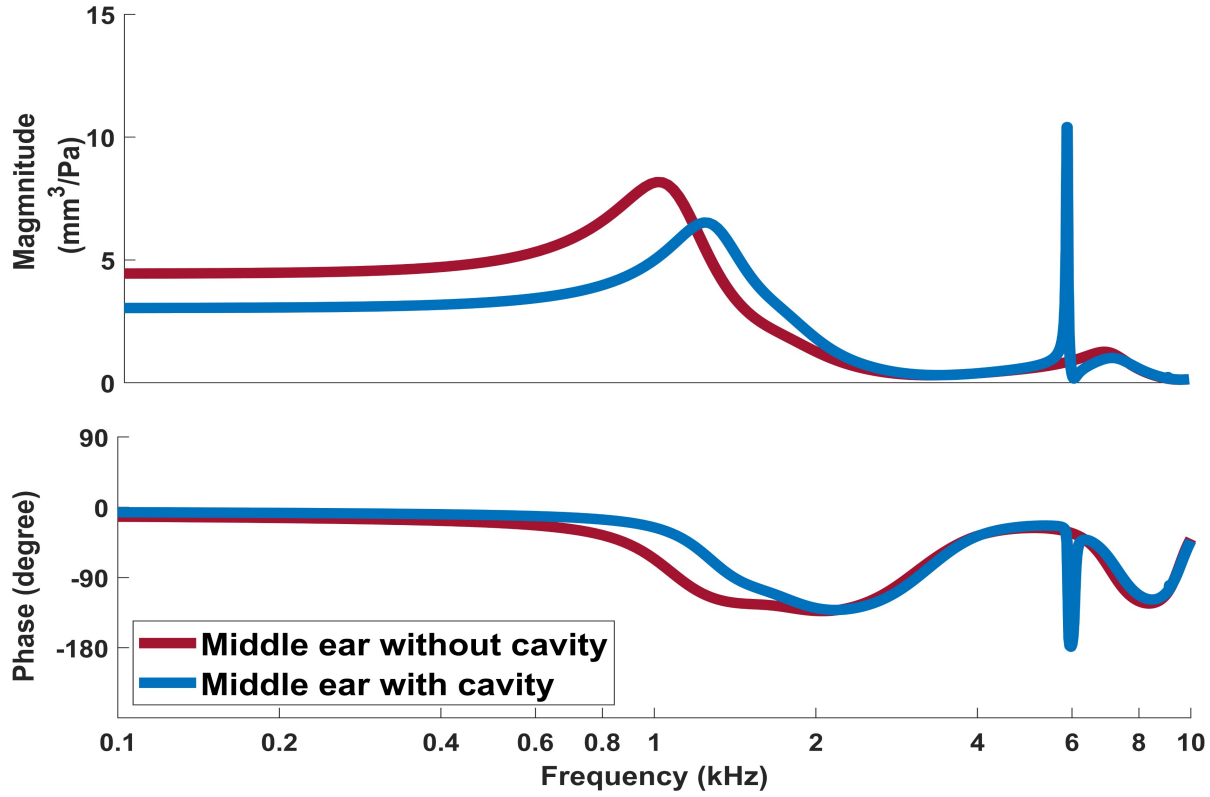

Figure 5.27: Volume displacement of 22-day-old model with and without middle-ear cavity. Volume displacement is computed at the medial surface of the probe tip. (After Motallebzadeh et al., 2017b)

5.9.4 Comparison with 22-day-old model and measured data

Figure 5.28 shows a qualitative comparison of our 1-day-old model response (orange lines, in terms of the maximum PT point displacements, magnitudes in nm/Pa) with the volume displacements (blue lines, magnitudes in mm^3/Pa) for the adjusted 22-day-old model of Motallebzadeh et al. (2017b); the mean measured data (red lines) of Keefe and Levi (1996); and the measured data for individual subjects (grey lines) reported by Motallebzadeh et al. (2017b). Some of the individual magnitude curves have substantially higher and sharper peaks than the mean curves, presumably because averaging smooths out sharp peaks that occur at different frequencies.

The resonance of our 1-day-old model (orange lines) happens at 1.84 kHz, while the middle-ear resonance of the adjusted model of Motallebzadeh et al. (2017b) occurs at 1.55 kHz. A resonance peak happens on the Keefe and Levi (1996) mean curve at about 2 kHz. The resonances of the individual subjects (grey lines) vary from 1 to 2.5 kHz. The average of the individual subjects' curves (red lines) has a broad resonance peak between 1 and 2 kHz with some minor local peaks. This frequency range covers the resonance frequencies of our 1-day-old model and of the adjusted model of Motallebzadeh et al. (2017b).

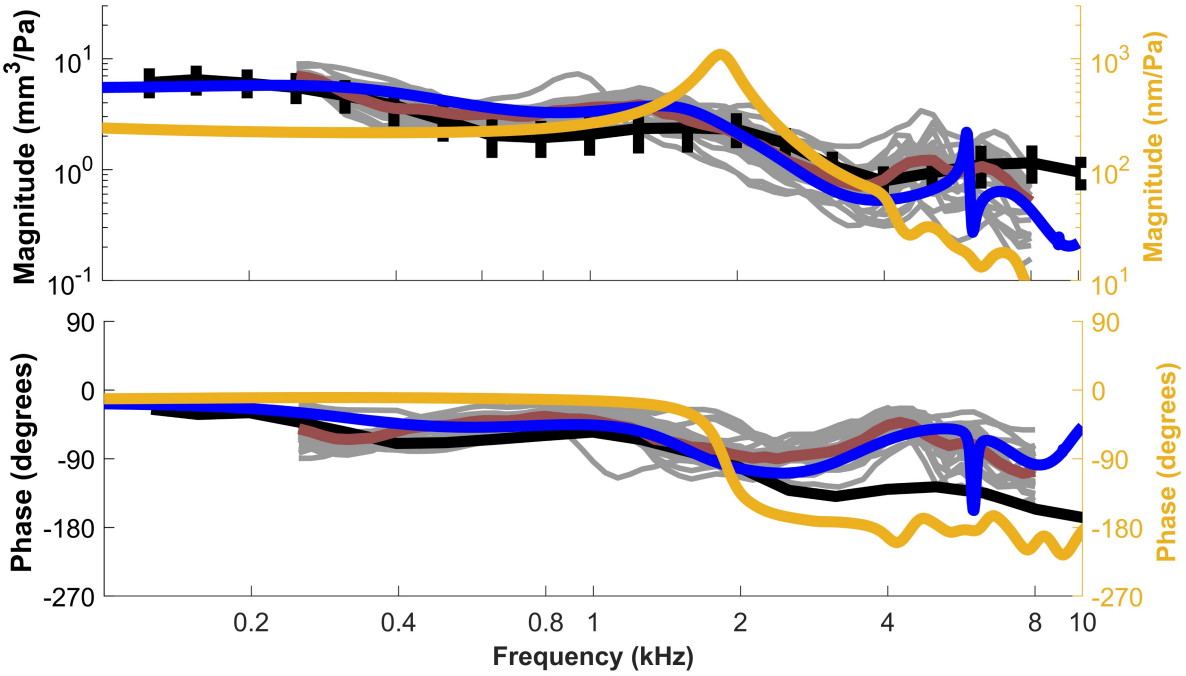

Figure 5.28: Comparison of frequency-response shapes between 1-day-old and 22-day-old model responses.
Orange lines (and axes) show maximum PT point displacement for 1-day-old model. Other lines show volume displacement: adjusted 22-day-old model (blue lines) of Motallebzadeh et al. (2017b); mean measured data (red lines) of Keefe and Levi (1996); and measured data for individual subjects (grey lines) and mean of the measured data (black lines and error bars) reported by Motallebzadeh et al. (2017b).

Above 3 kHz, a decrease in magnitude for our 1-day-old model can be seen. This decrease in magnitude can also be seen in both sets of clinical data and for the model of Motallebzadeh et al. (2017b).

We can see a sharp peak at 6.1 kHz followed by a minimum for the 22-day-old model. This peak is caused by a resonance of the middle-ear cavity. After that, there is a smaller local peak at 7 kHz, caused by the ear canal. The individual subjects' measurements show two local peaks located in the ranges of 4.5 to 5.5 kHz and 5.6 to 7.2 kHz, respectively, which may correspond to the model peaks at 6.1 and 7.2 kHz.

The phase for our 1-day-old model is near zero until around 1.4 kHz. After that, the phase decreases by about 155°, at frequencies similar to where the phase is decreasing for the 22-day-old model. After around 3.5 kHz, some small minima and maxima can be seen for our 1-day-old model. The phase does not increase at higher frequencies the way it does for the 22-day-old-model because the 1-day-old model does not include the ear canal and middle ear.

Chapter 6. Conclusion

6.1 Summary

In this study, a FE model of the 1-day-old newborn middle ear was developed to study its response under small audio-frequency pressures. We updated and modified the previous model of Shaho (2020). For instance, the sizes and shapes of the components were changed and adjusted according to the 1-day-old CT images. In addition, we reduced the length of the long process of the incus and the shape of the incus head. The mesh patterns of the structures were changed using various methods. For the geometry of the 3D model, four locally developed computer programs were used, including Fie, Tr3, Thrup'ny and Fad. Gmsh, an open source program, was used individually for each structure of the model to create a tetrahedral volume mesh from the triangulated surface mesh. We used FEBio as a FE solver. We also used MATLAB for data analysis, signal processing, and data visualization, as well as for calculating the thickness using the ray-triangle intersection algorithm.

The viscoelastic behavior of the 1-day-old middle ear was described using five equally spaced Prony-series time constants corresponding to frequencies from 10 Hz to 100 kHz, covering the acoustical stimulation frequencies of human hearing. The five Prony coefficients were all set to a value of 0.05 and were used for the TM and ligaments. The ossicles were modeled as isotropic elastic, and the elastic response of the TM was modelled as isotropic elastic. We determined the elastic properties of the model components based on the literature. The cochlear load was modelled by a damper almost perpendicular to the long process of the incus. In addition, a spring representing the stapedial annular ligament is at the same location as the damper. The same coefficients were used for the damper and spring as Motallebzadeh (2017a) used for their baseline model.

The thickness distribution for the 1-day-old model was calculated using a ray-triangle intersection algorithm. After that, the thickness distribution was compared with the thickness of the 22-day-old model of Motallebzadeh et al. (2017a) using the CT scan segmentations. In both models the TM was thinner in the central parts than near the borders.

We calculated and compared the static displacements for distinct regions of our middle-ear model under a step-function load and after passing through the transient response. The results were compared with the 22-day-old baseline model of Motallebzadeh et al. (2017a). We observed that the maximum displacements occur in the posterior regions of both models. We found that the PF displacement was negligible compared to that of the PT.

After running our dynamic model with a step time-domain stimulus and computing the FFT of the model response, we compared the responses of different regions of our 1-day-old model in the time domain and frequency domain in terms of resonance frequency, magnitude at resonance, and damping amounts. We concluded that the damping in the posterior and anterior PT is much less than the damping on the umbo, incus, and PF. We found that the middle-ear resonance occurs in the vicinity of 1.8 kHz in our 1-day-old model.

We performed a sensitivity analysis in order to determine how parameter values affect model behaviour. The sensitivity analysis was performed on PT, PF, ligaments, malleus, incus Young's modulus, bulk modulus (instead of Poisson's ratio), and mass density as well as the spring, damper and Prony coefficients, and we investigated their effects on the low-frequency magnitude, resonance frequency, and magnitude at resonance. Our results show that the PT Young's modulus, Prony coefficients, and PT bulk modulus substantially affect all three response features.

We also did a sensitivity analysis of the effects of individual Prony coefficients on the response of the middle ear. Our results show that the g_4 and g_5 Prony coefficients, corresponding to 100 Hz and 10 Hz, have much more significant effects on the low-frequency magnitude of the TM and umbo. Also, the g_3 Prony coefficient, corresponding to 1 kHz, affects the middle-ear resonance frequencies in addition to g_4 and g_5. The frequency corresponding to g_3 is not far from the baseline model resonance at around 1.8 kHz. The Prony coefficients g_3 and g_2, related to 1 and 10 kHz, respectively, have the most effect on the resonance magnitude of the TM and umbo.

Finally, we compared our 1-day-old model response with the response of the 22-day-old adjusted model of Motallebzadeh et al. (2017b), and with clinical data reported by Motallebzadeh et al. (2017b) and Keefe & Levi (1996). As the first stage for the comparison, we converted the admittance (volume velocity) of those results to volume displacement for comparison with our model's point displacements. Since our model does not include the external ear canal or the

middle-ear air cavities, but the 22-day-old model does, we first compared the 22-day-old model responses with a compliant canal wall and with a rigid canal wall in order to judge the effects of the ear-canal wall, and investigated the effect of the middle-ear cavity on the response of the 22-day-old model. In the end, we compared our 1-day-old response with that of the 22-day-old model and with the measured data. We concluded that the resonance frequency of our model was consistent with the adjusted model of Motallebzadeh et al. (2017b), with the data of Keefe and Levi (1996), and with the range of the clinical individual subjects reported by Motallebzadeh et al. (2017b).

6.2 Future work

Although our model was able to give results that matched some aspects of available measured data and of the previous FE model, some discrepancies need to be addressed, and further research can be done on those aspects.

The present model still simplifies the joints between the ossicles (IMJ and ISJ) and the middle-ear ligaments, which needs to be addressed in future studies. For instance, Soleimani et al. (2020) concluded that the ISJ capsule's curvature impacted the joint's reaction to tensile tests. Therefore, to accurately assess the effects of the ISJ and IMJ on the model response, realistic ISJ and IMJ shapes and material properties are required for the model. Additionally, our model does not include the pedicle structure of the incus; adding it would allow future studies to examine the possible effects of pedicle bending (e.g., Funnell et al., 2005).

Further improvement of the model can be achieved by improving the geometry, with a high priority for the TM and ligaments and less priority for the ossicles, in a more realistic and detailed manner. As an example, we could take into account the anisotropy and several layers of the TM in further studies. However, more complicated geometries will introduce more parameters to the system that need to be computed and will need a lot more computation power. Using the supercomputer was beneficial, especially for running multiple jobs in parallel, and decreasing the simulation time compared with the personal computers we used. Therefore, choosing which model components to include in the model has a great deal of importance. In addition, since the geometry of the model components can strongly affect their contribution to

the model response, a sensitivity analysis of the geometry of the model components and an exploration of the effects of anatomical variability is considered essential.

For every FE model, analysis of mesh convergence is considered a crucial step, and a value for mesh resolution should be selected as a trade-off between accuracy and computation time. To assess the adequacy of the mesh resolution for our middle-ear model, we mostly relied on the convergence study conducted by Shaho (2020). That convergence study was done by adjusting the XY-resolution parameter in Fie and then generating a new mesh with Tr3. The problem with that is that it does not do refinement in the Z direction. A better method is to bisect each element until we identify a trade-off between the accuracy of the model response and computational time. The accuracy of the model response can be investigated by calculating the changes in features such as resonance frequency and resonance magnitude. We tried several times to bisect our elements in Fad software but we encountered numerical difficulties, and in the end, for the sake of time, we employed the convergence results of Shaho (2020).

Based on the static maximum displacement calculations of distinct regions of our model under the step function load, we determine the ratio of the maximum TM displacement to umbo displacement to be around 11. This ratio was considerably less than this in some other studies (Mikhael et al., 2005; Golabbakhsh & Funnell, 2021). Further investigation in the literature about the value of this ratio is required as a first step toward adjusting it. It would be necessary to investigate adjustments of the spring coefficient and ligament Young's modulus after a conclusion is reached regarding this ratio for newborn ears.

In our sensitivity analysis results, we found that the malleus Young's modulus had a small effect on the umbo displacement magnitude at low frequency (100 Hz). It will be important to look into what value the Young's modulus should have, and it may be worthwhile to model the mallues bone as viscoleastic even if the effect of the ossicles' stiffness on the ear response is usually consideed to be negligible.

In this study, we investigated the spatial vibration pattern of the TM only at low frequencies. Studying the TM spatial vibration pattern at higher frequencies is important, but we were unable to do so due to the heavy file sizes that could not be opened in our FE postprocessor software. Alternative methods to overcome this technical limitation need to be addressed.

Issues have been reported in the literature concerning admittance measurements in newborns and infants (e.g., Paradise, 1982; Holte et al., 1991) due to the anatomical and mechanical differences between newborn and adult ears, such as the compliant properties of the ear-canal wall. In the comparison of our model response with the adjusted 22-day-old model of Motallebzadeh et al. (2017b) and with measured data, we just compared the resonance frequencies of our model and the overall pattern. We were not able to compare our model in terms of magnitude. Converting the response of our 1-day-old model to admittance will lead to an improvement in comparing and validating our results with clinical data. The results of our model could then be used in investigating the issues related to admittance measurements in newborns and infants.

In future modelling, it will be important to test the range of applicability of the approximations made here, especially in order to model the higher frequencies of wideband tympanometry. Also, the present linear dynamic modelling will need to be combined with previous nonlinear static modelling of the newborn canal wall and middle ear (e.g., Qi et al., 2006b, 2008b), as our lab has done in a preliminary way for the gerbil middle ear (Choukir, 2017; Qian, 2019; Kose et al., 2020).

6.3 Significance

Many acoustic and biomechanical factors affect ear responses, making it challenging to interpret both experimental and clinical results. Understanding the effects of the middle ear on sound transmission will help to improve screening and diagnosis. To assess the middle-ear condition, tympanometry is used, which involves non-linear techniques that use sounds and quasi-static pressure as inputs. However, tympanometry is poorly understood, especially at higher frequencies and especially in newborns. The differences in results between adults and newborns may be attributed to anatomical and physiological changes that occur during maturation.

Mathematical models are used to study the sophisticated systems. FE models, a type of mathematical modelling, have been used as an important tool to study the middle ear (e.g., Funnell & Laszlo, 1978; Motallebzadeh et al., 2017b).

In one approach to studying the condition of the middle ear from experimental data, a model can be fitted to the experimental data. Then, the fitted model parameters can be analyzed to understand the associated pathological conditions. This has primarily been done thus far using

rudimentary circuit models (e.g., Merchant & Neely, 2021). These models are naturally linear and their parameters are only indirectly associated with particular ear structures. However, FE models can easily be non-linear, as required in modelling tympanometry. In addition, the geometry and parameters of FE models are very closely related to the particular structures in the system being modelled. Therefore, the values of fitted parameters in a FE model can potentially offer more accurate clinical information. However, due to the computational complexity, the large number of parameters, and extensive individual variability, fitting a finite-element model to data is challenging.

Another method is to study the middle-ear condition directly from experimental and clinical data using statistical and machine-learning classification methods. These methods have had limited success.

These two methods are combined in simulation-based inference. Mathematical models are used to produce large amounts of simulated data in order to train a neural network. By doing so, computationally expensive models can be converted into fast inference engines. This method has the advantage of generating a probability distribution for each parameter, which includes all the interactions among parameters, rather than fitting a single 'best' set of parameters (e.g., Tejero-Cantero et al., 2020).

Development of a model like the one reported here can provide insight into the features of one aspect of clinical tympanometry applied to the newborn ear, namely, the response to acoustic stimuli. This is the first time, to the best of our knowledge, that the response of a 1-day-old human ear to sound has been modelled. The model takes into account the dynamic and viscoelastic behaviour. The model will improve our understanding of tympanometry by bridging the gap between quasi-static and dynamic acoustic measurements and by clarifying the complex relationships between them. Considering the importance of hearing screening being conducted shortly after birth, modeling the 1-day-old newborn ear is crucial to improve understanding of how clinical tympanometry might lead to better newborn hearing screening.

A number of clinical measurements have been used to study maturation effects, and it has been suggested that because of the outer ear's role in the input-admittance response at low frequencies, for newborns younger than 7 months, admittance measurement at the conventional

226-Hz probe-tone frequency is not advised in determining the health of the middle ear. However, there has not been a quantitative analysis of the fundamental mechanics.

Our numerical modelling of the 1-day-old model provides a quantitative description of the response of a normal 1-day-old human under acoustic stimuli from 100 Hz to 10 kHz. This frequency range is sufficiently broad to permit investigation of traditional low-frequency tympanomtery as well as middle-ear behaviour at the frequencies of more recent high-frequency (e.g., at 1 kHz) and wideband (up to 8 kHz) tympanometry (e.g., Margolis et al., 2003; Shahnaz et al., 2008).

In our current model of a 1-day-old newborn middle ear, the resonance frequency happens around 1.8 kHz, matching the observation of Keefe et al. (1993) that the main middle-ear resonance in newborns and infants happens around 1.8 kHz. There will be a variation in resonance frequency among newborns due to both intersubject variability and maturational effects. The modelling findings suggest that further measurements at frequencies close to the resonance frequency can provide additional information on the middle-ear status.

The development and growth of the newborn middle ear result in differences in geometrical and mechanical properties. Also, debris, mesenchyme and amniotic fluid exist in the newborn middle ear. In this study, we investigated the effects of different material properties on the response of the middle ear in terms of resonance frequencies and magnitudes and low-frequency magnitudes. This provides a basis for further studies to investigate the effects of geometrical variations as well as of residual fluids and debris on the newborn middle-ear response. In this way, the results of tympanometry in newborns can ultimately be better understood.

References

Aernouts, J., Aerts, J. R. M., & Dirckx, J. J. J. (2012). Mechanical properties of human tympanic membrane in the quasi-static regime from in situ point indentation measurements. *Hearing Research*, *290*(1–2), 45–54. https://doi.org/10.1016/j.heares.2012.05.001

Agache, P. G., Monneur, C., Leveque, J. L., & De Rigal, J. (1980). Mechanical properties and Young's modulus of human skin in vivo. *Archives of Dermatological Research*, *269*(3), 221–232. https://doi.org/10.1007/BF00406415

Aibara, R., Welsh, J. T., Puria, S., & Goode, R. L. (2001). Human middle-ear sound transfer function and cochlear input impedance. *Hearing Research*, *152*(1–2), 100–109. https://doi.org/10.1016/s0378-5955(00)00240-9

André, K. D., Sanches, S. G. G., & Carvallo, R. M. M. (2012). Middle ear resonance in infants: Age effects. *International Archives of Otorhinolaryngology*, *16*(3), 353–357. https://doi.org/10.7162/S1809-97772012000300009

Anson, B. J. (1981). *Surgical anatomy of the temporal bone* (3rd edition). Saunders.

Anthwal, N., & Thompson, H. (2016). The development of the mammalian outer and middle ear. *Journal of Anatomy*, *228*(2), 217–232. https://doi.org/10.1111/joa.12344

Antonutti, R., Peyrard, C., Incecik, A., Ingram, D., & Johanning, L. (2018). Dynamic mooring simulation with Code_Aster with application to a floating wind turbine. *Ocean Engineering*, *151*, 366–377. https://doi.org/10.1016/j.oceaneng.2017.11.018

Badouel, D. (1990). An efficient ray-polygon intersection. In *Graphics Gems* (pp. 390–393). Academic Press Professional, Inc.

Bagatto, M. P., & Moodie, S. T. (2016). Relevance of the international classification of functioning, health and disability: Children & youth version in early hearing detection and intervention programs. *Seminars in Hearing*, *37*(3), 257–271. https://doi.org/10.1055/s-0036-1584406

Békésy, G. von. (1960). *Experiments in hearing.* McGraw-Hill; WorldCat.org.

Belytschko, T., Liu, W. K., & Moran, B. (2000). *Nonlinear Finite Elements for Continua and Structures*. John Wiley & Sons, Ltd.

Cancura, W. (1979). [On the elasticity of the ligamentum anulare. Experimental investigations into human temporal bone preparations with the help of an electromagnetic probe (author's transl)]. *Archives of Oto-Rhino-Laryngology*, *225*(1), 27—32. https://doi.org/10.1007/bf00455872

Casale, J., Kandle, P. F., Murray, I., & Murr, N. (2022). Physiology, Cochlear Function. In *StatPearls*. StatPearls Publishing.

Chang, K. W., Vohr, B. R., Norton, S. J., & Lekas, M. D. (1993). External and middle ear status related to evoked otoacoustic emission in neonates. *Archives of Otolaryngology--Head & Neck Surgery*, *119*(3), 276–282. https://doi.org/10.1001/archotol.1993.01880150024004

Charlebois, M., Motallebzadeh, H., & Funnell, W. R. J. (2013). Visco-hyperelastic law for finite deformations: A frequency analysis. *Biomechanics and Modeling in Mechanobiology*, *12*(4), 705–715. https://doi.org/10.1007/s10237-012-0435-2

Cheng, J. T., Aarnisalo, A. A., Harrington, E., Hernandez-Montes, M. D. S., Furlong, C., Merchant, S. N., & Rosowski, J. J. (2010). Motion of the surface of the human tympanic membrane measured with stroboscopic holography. *Hearing Research*, *263*(1–2), 66–77. https://doi.org/10.1016/j.heares.2009.12.024

Cheng, T., Dai, C., & Gan, R. Z. (2007). Viscoelastic properties of human tympanic membrane. *Annals of Biomedical Engineering*, *35*(2), 305–314. https://doi.org/10.1007/s10439-006-9227-0

Cheng, T., & Gan, R. Z. (2007). Mechanical properties of stapedial tendon in human middle ear. *Journal of Biomechanical Engineering*, *129*(6), 913–918. https://doi.org/10.1115/1.2800837

Cheng, T., & Gan, R. Z. (2008a). Experimental measurement and modeling analysis on mechanical properties of tensor tympani tendon. *Medical Engineering & Physics*, *30*(3),

358–366. https://doi.org/10.1016/j.medengphy.2007.04.005

Cheng, T., & Gan, R. Z. (2008b). Mechanical properties of anterior malleolar ligament from experimental measurement and material modeling analysis. *Biomechanics and Modeling in Mechanobiology*, *7*(5), 387–394. https://doi.org/10.1007/s10237-007-0094-x

Choukir, S. (2017). *Finite-element modelling of tympanic-membrane vibrations under quasi-static pressurization* [Thesis]. McGill University.

Christensen, R. M. (1982). Chapter I - Viscoelastic Stress Strain Constitutive Relations. In R. M. Christensen (Ed.), *Theory of Viscoelasticity (Second Edition)* (pp. 1–34). Academic Press. https://doi.org/10.1016/B978-0-12-174252-2.50005-3

Colletti, V. (1975). Methodologic observations on tympanometry with regard to the probe tone frequency. *Acta Oto-Laryngologica*, *80*(1–2), 54–60. https://doi.org/10.3109/00016487509121300

Colletti, V., Fiorino, F. G., Sittoni, V., & Policante, Z. (1993). Mechanics of the Middle Ear in Otosclerosis and Stapedoplasty. *Acta Oto-Laryngologica*, *113*(5), 637–641. https://doi.org/10.3109/00016489309135877

Cook, L. T., Cook, P. N., Rak Lee, K., Batnitzky, S., Wong, B. Y. S., Fritz, S. L., Ophir, J., Dwyer, S. J., Bigongiari, L. R., & Templeton, A. W. (1980). An Algorithm for Volume Estimation Based on Polyhedral Approxi mation. *IEEE Transactions on Biomedical Engineering*, *BME-27*(9), 493–500. https://doi.org/10.1109/TBME.1980.326663

Cowin, S. C. (2001). Bone mechanics handbook, second edition. In *Bone Mechanics Handbook, Second Edition* (p. 980).

Dalmont, J.-P. (2001). Acoustic impedance measurement, part I: a review. *Journal of Sound and Vibration*, *243*(3), 427–439. https://doi.org/10.1006/jsvi.2000.3428

Daniel, S. J., Funnell, W. R. J., Zeitouni, A. G., Schloss, M. D., & Rappaport, J. (2001). Clinical applications of a finite-element model of the human middle ear. *The Journal of Otolaryngology*, *30*(6), 340–346. https://doi.org/10.2310/7070.2001.19393

Daphalapurkar, N. P., Dai, C., Gan, R. Z., & Lu, H. (2009). Characterization of the linearly viscoelastic behavior of human tympanic membrane by nanoindentation. *Journal of the Mechanical Behavior of Biomedical Materials*, *2*(1), 82–92. https://doi.org/10.1016/j.jmbbm.2008.05.008

de la Rochefoucauld, O., Decraemer, W. F., Khanna, S. M., & Olson, E. S. (2008). Simultaneous measurements of ossicular velocity and intracochlear pressure leading to the cochlear input impedance in gerbil. *Journal of the Association for Research in Otolaryngology: JARO*, *9*(2), 161–177. https://doi.org/10.1007/s10162-008-0115-1

de La Rochefoucauld, O., & Olson, E. S. (2010). A sum of simple and complex motions on the eardrum and manubrium in gerbil. *Hearing Research*, *263*(1–2), 9–15. https://doi.org/10.1016/j.heares.2009.10.014

Decraemer, & Khanna, S. m. (2004a). Measurement, visualization and quantitative analysis of complete three-dimensional kinematical data sets of human and cat middle ear. In *Middle Ear Mechanics in Research and Otology* (p. 10). https://doi.org/10.1142/9789812703019_0001

Decraemer, & Khanna, S. m. (2004b). Measurement, visualization and quantitative analysis of complete three-dimensional kinematical data sets of human and cat middle ear. In *Middle Ear Mechanics in Research and Otology* (p. 10). https://doi.org/10.1142/9789812703019_0001

Decraemer, W. F., Creten, W. L., & Van Camp, K. J. (1984). Tympanometric middle-ear pressure determination with two-component admittance meters. *Scandinavian Audiology*, *13*(3), 165–172. WorldCat.org. https://doi.org/10.3109/01050398409043056

Decraemer, W. F., de La Rochefoucauld, O., Dong, W., Khanna, S. M., Dirckx, J. J. J., & Olson, E. S. (2007). Scala vestibuli pressure and three-dimensional stapes velocity measured in direct succession in gerbil. *The Journal of the Acoustical Society of America*, *121*(5 Pt1), 2774–2791. https://doi.org/10.1121/1.2709843

Decraemer, W. F., Dirckx, J. J. J., & Funnell, W. R. J. (2003). Three-dimensional modelling of the middle-ear ossicular chain using a commercial high-resolution X-ray CT scanner. *Journal of the Association for Research in Otolaryngology: JARO*, *4*(2), 250–263. https://doi.org/10.1007/s10162-002-3030-x

Decraemer, W. F., & Funnell, W. R. J. (2008). Anatomical and mechanical properties of the tympanic membrane. In *Chronic Otitis Media Pathogenesis–Oriented Therapeutic Management* (pp. 51–84). Kugler Publications.

Decraemer, W. F., Khanna, S. M., & Funnell, W. R. J. (1989). Interferometric measurement of the amplitude and phase of tympanic membrane vibrations in cat. *Hearing Research*, *38*(1), 1–17. https://doi.org/10.1016/0378-5955(89)90123-8

Decraemer, W. F., Maes, M. A., & Vanhuyse, V. J. (1980). An elastic stress-strain relation for soft biological tissues based on a structural model. *Journal of Biomechanics*, *13*(6), 463–468. https://doi.org/10.1016/0021-9290(80)90338-3

Deltenre, P., & Van Maldergem, L. (2013). Chapter 158 - Hearing loss and deafness in the pediatric population: Causes, diagnosis, and rehabilitation. In O. Dulac, M. Lassonde, & H. B. Sarnat (Eds.), *Handbook of Clinical Neurology* (Vol. 113, pp. 1527–1538). Elsevier. https://doi.org/10.1016/B978-0-444-59565-2.00023-X

Dhondt, G. (2004). Linear Mechanical Applications. In *The Finite Element Method for Three-Dimensional Thermomechanical Applications* (p. 87). https://doi.org/10.1002/0470021217.ch2

Dirckx, J. J., & Decraemer, W. F. (2001a). Effect of middle ear components on eardrum quasi-static deformation. *Hearing Research*, *157*(1–2), 124–137. https://doi.org/10.1016/s0378-5955(01)00290-8

Dirckx, J. J., & Decraemer, W. F. (2001b). Effect of middle ear components on eardrum quasi-static deformation. *Hearing Research*, *157*(1–2), 124–137. https://doi.org/10.1016/s0378-5955(01)00290-8

Dirckx, J. J. J., Buytaert, J. A. N., & Decraemer, W. F. (2006). Quasi-static transfer function of the rabbit middle ear' measured with a heterodyne interferometer with high-resolution position decoder. *Journal of the Association for Research in Otolaryngology: JARO*, *7*(4), 339–351. https://doi.org/10.1007/s10162-006-0048-5

Eiber, A. (1999). Mechanical modeling and dynamical behavior of the human middle ear. *Audiology & Neuro-Otology*, *4*(3–4), 170–177. https://doi.org/10.1159/000013837

Elkhouri, N., Liu, H., & Funnell, W. R. J. (2006). Low-frequency finite-element modeling of the gerbil middle ear. *Journal of the Association for Research in Otolaryngology: JARO*, *7*(4), 399–411. https://doi.org/10.1007/s10162-006-0055-6

Ellaham, N. N., Akarche, F., Funnell, W. R. J., & Daniel, S. J. (2007). Experimental study of the effects of drying on middle-ear vibrations in the gerbil. *CMBES Proceedings*, *30*(1). https://proceedings.cmbes.ca/index.php/proceedings/article/view/141

Elner, A., Ingelstedt, S., & Ivarsson, A. (1971). The elastic properties of the tympanic membrance system. *Acta Oto-Laryngologica*, *72*(6), 397–403. https://doi.org/10.3109/00016487109122499

Fay, J., Puria, S., Decraemer, W. F., & Steele, C. (2005). Three approaches for estimating the elastic modulus of the tympanic membrane. *Journal of Biomechanics*, *38*(9), 1807–1815. https://doi.org/10.1016/j.jbiomech.2004.08.022

Feldman, A. S. (1976). Tympanometry—Procedures, interpretation and variables. In *Acoustic impedance and admittance—The measurement of middle ear function* (pp. 103–155). Baltimore: Williams & Wilkins.

Feldman, R. M., Fria, T. J., Palfrey, C. C., & Dellecker, C. M. (1984). Effects of rate of air pressure change on tympanometry. *Ear and Hearing*, *5*(2), 91–95. https://doi.org/10.1097/00003446-198403000-00006

Ferreira, A., Gentil, F., & Tavares, J. M. R. S. (2014). Segmentation algorithms for ear image data towards biomechanical studies. *Computer Methods in Biomechanics and Biomedical Engineering*, *17*(8), 888–904. https://doi.org/10.1080/10255842.2012.723700

Funasaka, S., Funai, H., & Kumakawa, K. (1984). Sweep-frequency tympanometry: Its development and diagnostic value. *Audiology*, *23*(4), 366–379. https://doi.org/10.3109/00206098409081530

Fung. (1993). Bone and Cartilage. In Y.-C. Fung (Ed.), *Biomechanics: Mechanical Properties of Living Tissues* (pp. 500–544). Springer New York. https://doi.org/10.1007/978-1-4757-2257-4_12

Fung, Y. C. (2013). *Biomechanics: Mechanical Properties of Living Tissues.* /z-wcorg/. https://search.ebscohost.com/login.aspx?direct=true&scope=site&db=nlebk&db=nlabk&AN=2859971

Funnell, W. R. J. (1983). On the undamped natural frequencies and mode shapes of a finite-element model of the cat eardrum. *The Journal of the Acoustical Society of America*, *73*(5), 1657–1661. https://doi.org/10.1121/1.389386

Funnell, W. R. J. (1984). On the choice of a cost function for the reconstruction of surfaces by triangulation between contours. *Computers & Structures*, *18*(1), 23–26. https://doi.org/10.1016/0045-7949(84)90077-4

Funnell, W. R. J., Decraemer, W. F., & Khanna, S. M. (1987). On the damped frequency response of a finite-element model of the cat eardrum. *The Journal of the Acoustical Society of America*, *81*(6), 1851–1859. https://doi.org/10.1121/1.394749

Funnell, W. R. J., Heng Siah, T., McKee, M. D., Daniel, S. J., & Decraemer, W. F. (2005). On the coupling between the incus and the stapes in the cat. *JARO: Journal of the Association for Research in Otolaryngology*, *6*(1), 9–18. https://doi.org/10.1007/s10162-004-5016-3

Funnell, W. R. J., Khanna, S. M., & Decraemer, W. F. (1992). On the degree of rigidity of the manubrium in a finite-element model of the cat eardrum. *The Journal of the Acoustical Society of America*, *91*(4 Pt 1), 2082–2090. https://doi.org/10.1121/1.403694

Funnell, W. R. J., & Laszlo, C. A. (1978). Modeling of the cat eardrum as a thin shell using the finite-element method. *The Journal of the Acoustical Society of America*, *63*(5), 1461–1467. https://doi.org/10.1121/1.381892

Funnell, W. R. J., & Laszlo, C. A. (1982). A critical review of experimental observations on ear-drum structure and function. *ORL; Journal for Oto-Rhino-Laryngology and Its Related Specialties*, *44*(4), 181–205. https://doi.org/10.1159/000275593

Funnell, W. R. J., Maftoon, N., & Decraemer, W. F. (2013). Modeling of middle-ear mechanics. In *The Middle Ear: Science, Otosurgery, and Technology, Springer Handbook of Auditory Research* (In S. Puria, A. N. Popper, R. R. Fay, pp. 171–210). Springer.

Funnell, W. R. J., Maftoon, N., & Decraemer, W. F. (2021). *Mechanics and modelling for the middle ear*. http://audilab.bme.mcgill.ca/mammie/

Gaihede, M. (1996). Tympanometric preconditioning of the tympanic membrane. *Hearing Research*, *102*(1–2), 28–34. https://doi.org/10.1016/s0378-5955(96)00146-3

Gan, R. Z., Feng, B., & Sun, Q. (2004). Three-dimensional finite element modeling of human ear for sound transmission. *Annals of Biomedical Engineering*, *32*(6), 847–859. https://doi.org/10.1023/b:abme.0000030260.22737.53

Gan, R. Z., Reeves, B. P., & Wang, X. (2007). Modeling of sound transmission from ear canal to cochlea. *Annals of Biomedical Engineering*, *35*(12), 2180–2195. https://doi.org/10.1007/s10439-007-9366-y

Gan, R. Z., Sun, Q., Feng, B., & Wood, M. W. (2006). Acoustic-structural coupled finite element analysis for sound transmission in human ear—Pressure distributions. *Medical Engineering & Physics*, *28*(5), 395–404. https://doi.org/10.1016/j.medengphy.2005.07.018

Gan, R. Z., Yang, F., Zhang, X., & Nakmali, D. (2011). Mechanical properties of stapedial annular ligament. *Medical Engineering & Physics*, *33*(3), 330–339. https://doi.org/10.1016/j.medengphy.2010.10.022

Gariepy, B. (2010). *Finite-element modelling of the newborn ear canal and middle ear* [Thesis]. McGill University.

Gea, S. L. R., Decraemer, W. F., Funnell, W. R. J., Dirckx, J. J. J., & Maier, H. (2010). Tympanic membrane boundary deformations derived from static displacements observed with

computerized tomography in human and gerbil. *Journal of the Association for Research in Otolaryngology: JARO*, *11*(1), 1–17. https://doi.org/10.1007/s10162-009-0192-9

Geerligs, M., van Breemen, L., Peters, G., Ackermans, P., Baaijens, F., & Oomens, C. (2011). In vitro indentation to determine the mechanical properties of epidermis. *Journal of Biomechanics*, *44*(6), 1176–1181. https://doi.org/10.1016/j.jbiomech.2011.01.015

Giannini, P., Marciano, E., Saulino, C., Strano, C. G., Alessio, M., Marcelli, V., & Auletta, G. (1997). Middle ear involvement in children with chronic rheumatoid juvenile arthritis. *European Archives of Oto-Rhino-Laryngology: Official Journal of the European Federation of Oto-Rhino-Laryngological Societies (EUFOS): Affiliated with the German Society for Oto-Rhino-Laryngology - Head and Neck Surgery*, *254 Suppl 1*, S30-33. https://doi.org/10.1007/BF02439717

Golabbakhsh, M., & Funnell, W. R. J. (2021). *Finite-element modelling based on imaging and vibration data for human middle ears*. H.B. Williams Pediatric Surgical Research Day, McGill University Health Centre, Montréal.

Golabbakhsh, M., Wang, X., MacDougall, D., Farrell, J., Landry, T., Funnell, W. R. J., & Adamson, R. (2020). *Finite-element modelling based on optical coherence tomography and X-ray microCT data for two human middle ears*. 43rd MidWinter Mtg., Assoc. Res. Otolaryngol., San Diego.

Hato, N., Stenfelt, S., & Goode, R. L. (2003). Three-dimensional stapes footplate motion in human temporal bones. *Audiology & Neuro-Otology*, *8*(3), 140–152. https://doi.org/10.1159/000069475

Holte, L., Cavanaugh, R. M., & Margolis, R. H. (1990). Ear canal wall mobility and tympanometric shape in young infants. *The Journal of Pediatrics*, *117*(1 Pt 1), 77–80. https://doi.org/10.1016/s0022-3476(05)82448-5

Holte, L., Margolish, R. H., & Cavanaugh, R. M. (1991). Developmental changes in multifrequency tympanograms. *International Journal of Audiology*, *30*(1), 1–24. https://doi.org/10.3109/00206099109072866

Homma, K., Shimizu, Y., Kim, N., Du, Y., & Puria, S. (2010). Effects of ear-canal pressurization on middle-ear bone- and air-conduction responses. *Hearing Research*, *263*(1–2), 204–215. https://doi.org/10.1016/j.heares.2009.11.013

Huang, G., Daphalapurkar, N. P., Gan, R. Z., & Lu, H. (2008). A method for measuring linearly viscoelastic properties of human tympanic membrane using nanoindentation. *Journal of Biomechanical Engineering*, *130*(1), 014501. https://doi.org/10.1115/1.2838034

Hunter, L. L., Feeney, M. P., Lapsley Miller, J. A., Jeng, P. S., & Bohning, S. (2010). Wideband reflectance in newborns: Normative regions and relationship to hearing screening results. *Ear and Hearing*, *31*(5), 599–610. https://doi.org/10.1097/AUD.0b013e3181e40ca7

Iacovou, E., Vlastarakos, P. V., Ferekidis, E., & Nikolopoulos, T. P. (2013). Multi-Frequency Tympanometry: Clinical Applications for the Assessment of the Middle Ear Status. *Indian Journal of Otolaryngology and Head & Neck Surgery*, *65*(3), 283–287. https://doi.org/10.1007/s12070-011-0470-9

Joint Committee on Infant Hearing. (1995). Joint Committee on Infant Hearing 1994 Position Statement. American Academy of Pediatrics Joint Committee on Infant Hearing. *Pediatrics*, *95*(1), 152–156.

Joint Committee on Infant Hearing. (2007). Year 2007 position statement: Principles and guidelines for early hearing detection and intervention programs. *Pediatrics*, *120*(4), 898–921. https://doi.org/10.1542/peds.2007-2333

Kabiri, M. (2023). *Meshsmooth-meshthicknessmap*. https://www.mathworks.com/matlabcentral/fileexchange/126510-meshsmooth-meshthicknessmap

Katz, J. (1978). *Handbook of clinical audiology* (second edition). Williams & Wilkins Co.

Keefe, D. H., Bulen, J. C., Arehart, K. H., & Burns, E. M. (1993). Ear-canal impedance and reflection coefficient in human infants and adults. *The Journal of the Acoustical Society of America*, *94*(5), 2617–2638. https://doi.org/10.1121/1.407347

Keefe, D. H., & Levi, E. (1996). Maturation of the middle and external ears: Acoustic power-based responses and reflectance tympanometry. *Ear and Hearing*, *17*(5), 361–373. https://doi.org/10.1097/00003446-199610000-00002

Keefe, D. H., & Simmons, J. L. (2003). Energy transmittance predicts conductive hearing loss in older children and adults. *The Journal of the Acoustical Society of America*, *114*(6 Pt 1), 3217–3238. https://doi.org/10.1121/1.1625931

Kelly, K. E., & Mohs, D. C. (1996). The external auditory canal. Anatomy and physiology. *Otolaryngologic Clinics of North America*, *29*(5), 725–739.

Khanna, S. M., & Tonndorf, J. (1972). Tympanic membrane vibrations in cats studied by time-averaged holography. *The Journal of the Acoustical Society of America*, *51*(6B), 1904–1920. https://doi.org/10.1121/1.1913050

Kim, N., Homma, K., & Puria, S. (2011). Inertial bone conduction: Symmetric and anti-symmetric components. *Journal of the Association for Research in Otolaryngology: JARO*, *12*(3), 261–279. https://doi.org/10.1007/s10162-011-0258-3

Kirikae, I., ,. (1960). *The structure and function of the middle ear*. Tokyo : Univ. of Tokyo Press; /z-wcorg/.

Knauss, W. G., & Zhao, J. (2007). Improved relaxation time coverage in ramp-strain histories. *Mechanics of Time-Dependent Materials*, *11*(3), 199–216. https://doi.org/10.1007/s11043-007-9035-4

Kobayashi, T., Okitsu, T., Endo, S., & Kawamoto, K. (1985). Forward-backward tracing tympanometry in the diagnosis of middle ear pressure. *Auris, Nasus, Larynx*, *12 Suppl 1*, S219-221. https://doi.org/10.1016/s0385-8146(85)80155-3

Koike, T., Wada, H., & Kobayashi, T. (2002). Modeling of the human middle ear using the finite-element method. *The Journal of the Acoustical Society of America*, *111*(3), 1306–1317. https://doi.org/10.1121/1.1451073

Konrádsson, K. S., Ivarsson, A., & Bank, G. (1987). Computerized laser Doppler interferometric scanning of the vibrating tympanic membrane. *Scandinavian Audiology*, *16*(3), 159–166.

https://doi.org/10.3109/01050398709042171

Kose, O., Funnell, W. R. J., & Daniel, S. J. (2017). In vivo experimental study of gerbil eardrum vibrations under static pressures. *40th MidWinter Mtg., Assoc. Res. Otolaryngol., Baltimore*.

Kose, O., Funnell, W. R. J., & Daniel, S. J. (2020). Vibration measurements of the gerbil eardrum under quasi-static pressure steps. *Journal of the Association for Research in Otolaryngology: JARO*, *21*(4), 287–302. https://doi.org/10.1007/s10162-020-00763-2

Kose, O., Funnell, W. R. J., & Daniel, S. J. (2022). Vibration measurements of the gerbil eardrum under quasi-static pressure sweeps. *Journal of the Association for Research in Otolaryngology: JARO*. https://doi.org/10.1007/s10162-022-00867-x

Kose, O., Shapiro, R., Funnell, W. R. J., & Daniel, S. J. (2016). An experimental study of vibrations in the gerbil middle ear under static pressure. *39th Midwinter Res. Mtg., Assoc. Res.*

Kuypers, L. C., Decraemer, W. F., & Dirckx, J. J. J. (2006). Thickness distribution of fresh and preserved human eardrums measured with confocal microscopy. *Otology & Neurotology: Official Publication of the American Otological Society, American Neurotology Society [and] European Academy of Otology and Neurotology*, *27*(2), 256–264. https://doi.org/10.1097/01.mao.0000187044.73791.92

Kuypers, L. C., Dirckx, J. J. J., Decraemer, W. F., & Timmermans, J.-P. (2005). Thickness of the gerbil tympanic membrane measured with confocal microscopy. *Hearing Research*, *209*(1–2), 42–52. https://doi.org/10.1016/j.heares.2005.06.003

Kwacz, M., Rymuza, Z., Michałowski, M., & Wysocki, J. (2015). Elastic properties of the annular ligament of the human stapes—AFM measurement. *Journal of the Association for Research in Otolaryngology: JARO*, *16*(4), 433–446. https://doi.org/10.1007/s10162-015-0525-9

Ladak, H. M., Decraemer, W. F., Dirckx, J. J. J., & Funnell, W. R. J. (2004). Response of the cat eardrum to static pressures: Mobile versus immobile malleus. *The Journal of the*

Acoustical Society of America, *116*(5), 3008–3021. https://doi.org/10.1121/1.1802673

Ladak, H. M., & Funnell, W. R. J. (1996). Finite-element modeling of the normal and surgically repaired cat middle ear. *The Journal of the Acoustical Society of America*, *100*(2 Pt 1), 933–944. https://doi.org/10.1121/1.416205

Ladak, H. M., Funnell, W. R. J., Decraemer, W. F., & Dirckx, J. J. J. (2006). A geometrically nonlinear finite-element model of the cat eardrum. *The Journal of the Acoustical Society of America*, *119*(5 Pt 1), 2859–2868. https://doi.org/10.1121/1.2188370

Lambourne, J., Djuric, Z., Brujic, D., & Ristic, M. (2005). Calculation and visualisation of the thickness of 3D CAD models. In *Proceedings—International Conference on Shape Modeling and Applications, SMI'05* (Vol. 2005, p. 342). https://doi.org/10.1109/SMI.2005.7

Lanterne, C., Gueorguieva, S., & Desbarats, P. (2016, July). *Local thickness computation in 3D meshes and 3D printability assessment*. MCCSIS International Conference on Computer Graphics, Visualization, Computer Vision and Image Processing, Madeira, Portugal.

Lauxmann, M., Eiber, A., Haag, F., & Ihrle, S. (2014). Nonlinear stiffness characteristics of the annular ligament. *The Journal of the Acoustical Society of America*, *136*(4), 1756–1767. https://doi.org/10.1121/1.4895696

Lee, C. Y., & Rosowski, J. J. (2001). Effects of middle-ear static pressure on pars tensa and pars flaccida of gerbil ears. *Hearing Research*, *153*(1–2), 146–163. https://doi.org/10.1016/s0378-5955(00)00269-0

Lidén, G., Björkman, G., Nyman, H., & Kunov, H. (1977). Tympanometry and acoustic impedance. *Acta Oto-Laryngologica*, *83*(1–6), 140–145. https://doi.org/10.3109/00016487709128824

Lilly, D. J. (1984). Multiple frequency, multiple component tympanometry: New approaches to an old diagnostic problem. *Ear and Hearing*, *5*(5), 300–308.

Lim, D. J. (1968). Tympanic membrane part II.: Pars flaccida. *Acta Oto-Laryngologica*, *66*(1–6), 515–532. https://doi.org/10.3109/00016486809126316

Lim, D. J. (1970). Human tympanic membrane. An ultrastructural observation. *Acta Oto-Laryngologica*, *70*(3), 176–186. https://doi.org/10.3109/00016487009181875

Luo, H., Dai, C., Gan, R. Z., & Lu, H. (2009a). Measurement of young's modulus of human tympanic membrane at high strain rates. *Journal of Biomechanical Engineering*, *131*(6), 064501. https://doi.org/10.1115/1.3118770

Luo, H., Lu, H., Dai, C., & Gan, R. (2009b). A comparison of Young's modulus for normal and diseased human eardrums at high strain rates. *International Journal of Experimental and Computational Biomechanics*, *1*. https://doi.org/10.1504/IJECB.2009.022856

Luo, H., Wang, F., Cheng, C., Nakmali, D. U., Gan, R. Z., & Lu, H. (2019). Mapping the Young's modulus distribution of the human tympanic membrane by microindentation. *Hearing Research*, *378*, 75–91. https://doi.org/10.1016/j.heares.2019.02.009

Maas, S. A., Ellis, B. J., Ateshian, G. A., & Weiss, J. A. (2012). FEBio: Finite elements for biomechanics. *Journal of Biomechanical Engineering*, *134*(1), 011005. https://doi.org/10.1115/1.4005694

Maftoon, N., Funnell, W. R. J., Daniel, S. J., & Decraemer, W. F. (2013). Experimental study of vibrations of gerbil tympanic membrane with closed middle ear cavity. *JARO: Journal of the Association for Research in Otolaryngology*, *14*(4), 467–481. https://doi.org/10.1007/s10162-013-0389-9

Maftoon, N., Funnell, W. R. J., Daniel, S. J., & Decraemer, W. F. (2014a). Effect of opening middle-ear cavity on vibrations of gerbil tympanic membrane. *Journal of the Association for Research in Otolaryngology: JARO*, *15*(3), 319–334. https://doi.org/10.1007/s10162-014-0442-3

Maftoon, N., Funnell, W. R. J., Daniel, S. J., & Decraemer, W. F. (2014b). Effect of opening middle-ear cavity on vibrations of gerbil tympanic membrane. *Journal of the Association for Research in Otolaryngology: JARO*, *15*(3), 319–334. https://doi.org/10.1007/s10162-014-0442-3

Maftoon, N., Funnell, W. R. J., Daniel, S. J., & Decraemer, W. F. (2015). Finite-element modelling of the response of the gerbil middle ear to sound. *Journal of the Association for Research in Otolaryngology: JARO*, *16*(5), 547–567. https://doi.org/10.1007/s10162-015-0531-y

Marazita, M. L., Ploughman, L. M., Rawlings, B., Remington, E., Arnos, K. S., & Nance, W. E. (1993). Genetic epidemiological studies of early-onset deafness in the U.S. school-age population. *American Journal of Medical Genetics*, *46*(5), 486–491. https://doi.org/10.1002/ajmg.1320460504

Margolis, R. H., Bass-Ringdahl, S., Hanks, W. D., Holte, L., & Zapala, D. A. (2003). Tympanometry in newborn infants—1 kHz norms. *Journal of the American Academy of Audiology*, *14*(7), 383–392.

McKinley, A. M., Grose, J. H., & Roush, J. (1997). Multifrequency tympanometry and evoked otoacoustic emissions in neonates during the first 24 hours of life. *Journal of the American Academy of Audiology*, *8*(3), 218–223.

McLellan, M. S., & Webb, C. H. (1957). Ear studies in the newborn infant: Natural appearance and incidence of obscuring by vernix, cleansing of vernix, and description of drum and canal after cleansing. *The Journal of Pediatrics*, *51*(6), 672–677. https://doi.org/10.1016/s0022-3476(57)80102-4

Merchant, & Neely, S. T. (2021). The influence of otitis media with effusion on middle-ear impedance estimated from wideband acoustic immittance measurements. *The Journal of the Acoustical Society of America*, *150*(2), 969. https://doi.org/10.1121/10.0005822

Merchant, S. N., Ravicz, M. E., & Rosowski, J. J. (1996). Acoustic input impedance of the stapes and cochlea in human temporal bones. *Hearing Research*, *97*(1–2), 30–45.

Meyer, S. E., Jardine, C. A., & Deverson, W. (1997). Developmental changes in tympanometry: A case study. *British Journal of Audiology*, *31*(3), 189–195. https://doi.org/10.3109/03005364000000021

Mikhael, C. S., Funnell, W. R. J., & Bance, M. (2005). Middle-ear finite-element modelling with realistic geometry and a priori material-property estimates. *CMBES Proceedings*, *28*. https://proceedings.cmbes.ca/index.php/proceedings/article/view/464

Møller, A. R. (1974). The Acoustic Middle Ear Muscle Reflex. In H. W. Ades, A. Axelsson, I. L. Baird, G. v. Békésy, R. L. Boord, C. B. G. Campbell, O. Densert, D. H. Eldredge, H. Engström, J. Fex, J. M. Harrison, O. W. Henson, M. E. Howe, S. Iurato, A. Michelsen, A. R. Møller, R. R. Pfeiffer, S. Rauch, I. Rauch, … W. D. Neff (Eds.), *Auditory System: Anatomy Physiology (Ear)* (pp. 519–548). Springer. https://doi.org/10.1007/978-3-642-65829-7_16

Möller, T., & Trumbore, B. (1997). Fast, minimum storage ray-triangle intersection. *J. Graph. Tools*, *2*(1), 21–28. https://doi.org/10.1080/10867651.1997.10487468

Motallebzadeh, H., Charlebois, M., & Funnell, W. R. J. (2013). A non-linear viscoelastic model for the tympanic membrane. *The Journal of the Acoustical Society of America*, *134*(6), 4427. https://doi.org/10.1121/1.4828831

Motallebzadeh, H., Maftoon, N., Pitaro, J., Funnell, W. R. J., & Daniel, S. J. (2017a). Finite-element modelling of the acoustic input admittance of the newborn ear canal and middle ear. *Journal of the Association for Research in Otolaryngology: JARO*, *18*(1), 25–48. https://doi.org/10.1007/s10162-016-0587-3

Motallebzadeh, H., Maftoon, N., Pitaro, J., Funnell, W. R. J., & Daniel, S. J. (2017b). Fluid-structure finite-element modelling and clinical measurement of the wideband acoustic input admittance of the newborn ear canal and middle ear. *JARO: Journal of the Association for Research in Otolaryngology*, *18*(5), 671. https://doi.org/10.1007/s10162-017-0630-z

Motallebzadeh, H., & Puria, S. (2021). Mouse middle-ear forward and reverse acoustics. *The Journal of the Acoustical Society of America*, *149*(4), 2711–2731. https://doi.org/10.1121/10.0004218

Motallebzadeh, H., & Puria, S. (2022). Stimulus-frequency otoacoustic emissions and middle-ear pressure gains in a finite-element mouse model. *The Journal of the Acoustical Society of America*, *152*(5), 2769. https://doi.org/10.1121/10.0014901

Mozaffari, M., Nash, R., & Tucker, A. S. (2021). Anatomy and development of the mammalian external auditory canal: Implications for understanding canal disease and deformity. *Frontiers in Cell and Developmental Biology*, *8*, 617354. https://doi.org/10.3389/fcell.2020.617354

Musiek, F. E., & Chermak, G. D. (2015). Chapter 18—Psychophysical and behavioral peripheral and central auditory tests. In M. J. Aminoff, F. Boller, & D. F. Swaab (Eds.), *Handbook of Clinical Neurology* (Vol. 129, pp. 313–332). Elsevier. https://doi.org/10.1016/B978-0-444-62630-1.00018-4

Nambiar, S. (2010). *An experimental study of middle-ear vibrations in gerbils (Master's)*.

Nelson, H. D., Bougatsos, C., & Nygren, P. (2008). *Universal Newborn Hearing Screening: Systematic Review to Update the 2001 U.S. Preventive Services Task Force Recommendation*. Agency for Healthcare Research and Quality (US). http://www.ncbi.nlm.nih.gov/books/NBK33992/

Noussios, G., Chouridis, P., Kostretzis, L., & Natsis, K. (2016). Morphological and morphometrical study of the human ossicular chain: A review of the literature and a meta-analysis of experience over 50 years. *Journal of Clinical Medicine Research*, *8*(2), 76–83. https://doi.org/10.14740/jocmr2369w

Olszewski, J. (1990). [The morphometry of the ear ossicles in humans during development]. *Anatomischer Anzeiger*, *171*(3), 187–191.

Paradise, J. L. (1982). Editorial retrospective: Tympanometry. *The New England Journal of Medicine*, *307*(17), 1074–1076. https://doi.org/10.1056/NEJM198210213071709

Park, M. K. (2017). Clinical applications of wideband tympanometry. *Korean Journal of Otorhinolaryngology-Head and Neck Surgery*, *60*(8), 375–380. https://doi.org/10.3342/kjorl-hns.2017.00605

Pitaro, J., Al Masaoudi, L., Motallebzadeh, H., Funnell, W. R. J., & Daniel, S. J. (2016). Wideband reflectance measurements in newborns: Relationship to otoscopic findings. *International Journal of Pediatric Otorhinolaryngology*, *86*, 156–160. https://doi.org/10.1016/j.ijporl.2016.04.036

Qi, L., Funnell, W. R. J., & Daniel, S. J. (2008a). A nonlinear finite-element model of the newborn middle ear. *The Journal of the Acoustical Society of America*, *124*(1), 337–347. https://doi.org/10.1121/1.2920956

Qi, L., Funnell, W. R. J., & Daniel, S. J. (2008b). A nonlinear finite-element model of the newborn middle ear. *The Journal of the Acoustical Society of America*, *124*(1), 337–347. https://doi.org/10.1121/1.2920956

Qi, L., Liu, H., Lutfy, J., Funnell, W. R. J., & Daniel, S. J. (2006a). A non-linear finite-element model of the newborn ear canal. *The Journal of the Acoustical Society of America*, *120*(6), 3789–3798.

Qi, L., Liu, H., Lutfy, J., Funnell, W. R. J., & Daniel, S. J. (2006b). A nonlinear finite-element model of the newborn ear canal. *The Journal of the Acoustical Society of America*, *120*(6), 3789–3798. https://doi.org/10.1121/1.2363944

Qian, T. (2019). *Finite-element modelling of middle-ear vibrations under quasi-static pressurization* [Thesis]. McGill University.

Rabbitt, R. D., & Holmes, M. H. (1986). A fibrous dynamic continuum model of the tympanic membrane. *The Journal of the Acoustical Society of America*, *80*(6), 1716–1728. https://doi.org/10.1121/1.394284

Ravicz, M. E., Cooper, N. P., & Rosowski, J. J. (2008). Gerbil middle-ear sound transmission from 100 Hz to 60 kHz. *The Journal of the Acoustical Society of America*, *124*(1), 363–380. https://doi.org/10.1121/1.2932061

Ravicz, M. E., & Rosowski, J. J. (1997). Sound-power collection by the auditory periphery of the Mongolian gerbil Meriones unguiculatus: III. Effect of variations in middle-ear volume.

The Journal of the Acoustical Society of America, *101*(4), 2135–2147. https://doi.org/10.1121/1.418275

Ravicz, M. E., Rosowski, J. J., & Voigt, H. F. (1992). Sound-power collection by the auditory periphery of the Mongolian gerbil Meriones unguiculatus. I: Middle-ear input impedance. *The Journal of the Acoustical Society of America*, *92*(1), 157–177. https://doi.org/10.1121/1.404280

Rollhäuser, H. (1950). Die zugfestigkeit der menschlichen haut. *Gegenbaurs Morph Jb*, *90*, 249–261.

Roosa, D. B. S. J. (1891). *A Practical treatise on the diseases of the ear*. W. Wood.

Rosenwasser, H. (1964). Otitic problems in the aged. *Geriatrics*, *19*, 11–17.

Rosowski, J. J., Cheng, J. T., Ravicz, M. E., Hulli, N., Hernandez-Montes, M., Harrington, E., & Furlong, C. (2009). Computer-assisted time-averaged holograms of the motion of the surface of the mammalian tympanic membrane with sound stimuli of 0.4 to 25 kHz. *Hearing Research*, *253*(1–2), 83–96. https://doi.org/10.1016/j.heares.2009.03.010

Rosowski, J. J., & Wilber, L. A. (2015). Acoustic immittance, absorbance, and reflectance in the human ear canal. *Seminars in Hearing*, *36*(1), 11–28. PubMed. https://doi.org/10.1055/s-0034-1396924

Ruah, C. B., Schachern, P. A., Zelterman, D., Paparella, M. M., & Yoon, T. H. (1991). Age-related morphologic changes in the human tympanic membrane. A light and electron microscopic study. *Archives of Otolaryngology--Head & Neck Surgery*, *117*(6), 627–634. https://doi.org/10.1001/archotol.1991.01870180063013

Salih, W. H. M., Soons, J. A. M., & Dirckx, J. J. J. (2016). 3D displacement of the middle ear ossicles in the quasi-static pressure regime using new X-ray stereoscopy technique. *Hearing Research*, *340*, 60–68. https://doi.org/10.1016/j.heares.2015.12.003

Sanford, C. A., & Feeney, M. P. (2008). Effects of maturation on tympanometric wideband acoustic transfer functions in human infants. *The Journal of the Acoustical Society of America*, *124*(4), 2106–2122. https://doi.org/10.1121/1.2967864

Saunders, J. C., Kaltenbach, J. A., & Relkin, E. M. (1983). Development of Auditory and Vestibular Systems. In *The structural and functional development of the outer and middle ear.*

Schofield, B. R., & Beebe, N. L. (2020). 2.26 - The Efferent Auditory System: Central Pathways That Modulate Peripheral Input. In B. Fritzsch (Ed.), *The Senses: A Comprehensive Reference (Second Edition)* (pp. 501–516). Elsevier. https://doi.org/10.1016/B978-0-12-809324-5.23826-1

Shahnaz, N., Miranda, T., & Polka, L. (2008). Multifrequency tympanometry in neonatal intensive care unit and well babies. *Journal of the American Academy of Audiology*, *19*(5), 392–418. https://doi.org/10.3766/jaaa.19.5.3

Shaho, S. (2020). *Finite-element modelling of the newborn middle ear at two different ages* [Thesis]. McGill University and Eberhard Karls Universit¨at T¨ubingen.

Shanks, J. E., & Lilly, D. J. (1981). An evaluation of tympanometric estimates of ear canal volume. *Journal of Speech and Hearing Research*, *24*(4), 557–566. https://doi.org/10.1044/jshr.2404.557

Shanks, J. E., & Shohet, J. A. (2008). Tympanometry in Clinical Practice. In *Handbook of Clinical Audiology*.

Shanks, J. E., & Wilson, R. H. (1986). Effects of direction and rate of ear-canal pressure changes on tympanometric measures. *Journal of Speech and Hearing Research*, *29*(1), 11–19. https://doi.org/10.1044/jshr.2901.11

Soleimani, M., Funnell, W. R. J., & Decraemer, W. F. (2020). A non-linear viscoelastic model of the incudostapedial joint. *JARO: Journal of the Association for Research in Otolaryngology*, *21*(1), 21–32. https://doi.org/10.1007/s10162-019-00736-0

Soons, J. A. M., Aernouts, J., & Dirckx, J. J. J. (2010). Elasticity modulus of rabbit middle ear ossicles determined by a novel micro-indentation technique. *Hearing Research*, *263*(1–2), 33–37. https://doi.org/10.1016/j.heares.2009.10.001

Stach, B. A., & Ramachandran, Virginia. (2017). *Clinical Audiology An Introduction.* (3rd ed., Vol. 1–1 online resource (664 p.)). Plural Publishing, Incorporated; WorldCat.org. http://public.eblib.com/choice/PublicFullRecord.aspx?p=6499978

Standring, S. (2021). Chapater 16. In *Gray's Anatomy E-Book: The Anatomical Basis of Clinical Practice*. Elsevier Health Sciences.

Sun, Q., Gan, R. Z., Chang, K.-H., & Dormer, K. J. (2002). Computer-integrated finite element modeling of human middle ear. *Biomechanics and Modeling in Mechanobiology*, *1*(2), 109–122. https://doi.org/10.1007/s10237-002-0014-z

Tejero-Cantero, A., Boelts, J., Deistler, M., Lueckmann, J.-M., Durkan, C., Gonçalves, P. J., Greenberg, D. S., & Macke, J. H. (2020). sbi: A toolkit for simulation-based inference. *Journal of Open Source Software*, *5*(52), 2505. https://doi.org/10.21105/joss.02505

Teoh, S. W., Flandermeyer, D. T., & Rosowski, J. J. (1997). Effects of pars flaccida on sound conduction in ears of Mongolian gerbil: Acoustic and anatomical measurements. *Hearing Research*, *106*(1–2), 39–65. https://doi.org/10.1016/s0378-5955(97)00002-6

Terkildsen, K., & Thomsen, K. A. (1959). The influence of pressure variations on the impedance of the human ear drum: A method for objective determination of the middle-ear pressure. *The Journal of Laryngology & Otology*, *73*(7), 409–418. Cambridge Core. https://doi.org/10.1017/S002221510005550X

Therkildsen, A. G., & Gaihede, M. (2005). Accuracy of tympanometric middle ear pressure determination: The role of direction and rate of pressure change with a fast, modern tympanometer. *Otology & Neurotology: Official Publication of the American Otological Society, American Neurotology Society [and] European Academy of Otology and Neurotology*, *26*(2), 252–256. https://doi.org/10.1097/00129492-200503000-00021

Tonndorf, J., & Khanna, S. M. (1968). Submicroscopic displacement amplitudes of the tympanic membrane (cat) measured by a laser interferometer. *The Journal of the Acoustical Society of America*, *44*(6), 1546–1554. https://doi.org/10.1121/1.1911295

Tonndorf, J., & Khanna, S. M. (1972). Tympanic-membrane vibrations in human cadaver ears studied by time-averaged holography. *The Journal of the Acoustical Society of America*, *52*(4), 1221–1233. https://doi.org/10.1121/1.1913236

Tuck-Lee, J. P., Pinsky, P. M., Steele, C. R., & Puria, S. (2008). Finite element modeling of acousto-mechanical coupling in the cat middle ear. *The Journal of the Acoustical Society of America*, *124*(1), 348–362. https://doi.org/10.1121/1.2912438

Van Camp, K. J., Margolis, R. H., Wilson, R. H., Creten, W. L., & Shanks, J. E. (1986). Principles of tympanometry. *ASHA Monographs*, *24*, 1–88.

Van Camp, K. J., & Vogeleer, M. (1986). Normative multifrequency tympanometric data on otosclerosis. *Scandinavian Audiology*, *15*(4), 187–190. https://doi.org/10.3109/01050398609042142

Van der Jeught, S., Dirckx, J. J. J., Aerts, J. R. M., Bradu, A., Podoleanu, A. G. H., & Buytaert, J. A. N. (2013). Full-field thickness distribution of human tympanic membrane obtained with optical coherence tomography. *Journal of the Association for Research in Otolaryngology: JARO*, *14*(4), 483–494. https://doi.org/10.1007/s10162-013-0394-z

Vanhuyse, V. J., Creten, W. L., & Van Camp, K. J. (1975). On the W-notching of tympanograms. *Scandinavian Audiology*, *4*(1), 45–50. https://doi.org/10.3109/01050397509075014

von Békésy, G. (1941). *Über die Messung der Schwingungsamplitude der Gehörknöcheln mittels einer kapazitiven Sonde*.

Wada, H., Ando, M., Takeuchi, M., Sugawara, H., Koike, T., Kobayashi, T., Hozawa, K., Gemma, T., & Nara, M. (2002). Vibration measurement of the tympanic membrane of guinea pig temporal bones using time-averaged speckle pattern interferometry. *The Journal of the Acoustical Society of America*, *111*(5 Pt 1), 2189–2199. https://doi.org/10.1121/1.1467671

Wada, H., & Kobayashi, T. (1990). Dynamical behavior of middle ear: Theoretical study corresponding to measurement results obtained by a newly developed measuring

apparatus. *The Journal of the Acoustical Society of America*, *87*(1), 237–245. https://doi.org/10.1121/1.399290

Wada, H., Metoki, T., & Kobayashi, T. (1992). Analysis of dynamic behavior of human middle ear using a finite-element method. *The Journal of the Acoustical Society of America*, *92*(6), 3157–3168. https://doi.org/10.1121/1.404211

Wang, X. (2019). *Finite-element modelling of the human middle ear based on X-ray micro-computed tomography and Doppler optical coherence tomography in the same ear* [Thesis]. McGill University.

Wang, X., Cheng, T., & Gan, R. Z. (2007). Finite-element analysis of middle-ear pressure effects on static and dynamic behavior of human ear. *The Journal of the Acoustical Society of America*, *122*(2), 906–917. https://doi.org/10.1121/1.2749417

Wang, Y. C., & Lakes, R. S. (2005). Composites with inclusions of negative bulk modulus: Extreme damping and negative Poisson's ratio. *Journal of Composite Materials*, *39*(18), 1645–1657. https://doi.org/10.1177/0021998305051112

Wever, E. G., & Lawrence, M. (1954). In *Physiological Acoustics* (pp. xi–xii). Princeton University Press.

Willi, U. B., Ferrazzini, M. A., & Huber, A. M. (2002). The incudo-malleolar joint and sound transmission losses. *Hearing Research*, *174*(1–2), 32–44. https://doi.org/10.1016/s0378-5955(02)00632-9

Wolff, D., & Bellucci, R. J. (1956). The human ossicular ligaments. *Annals of Otology, Rhinology & Laryngology*, *65*(4), 895–910. https://doi.org/10.1177/000348945606500401

Yamada, H. (1970). *Strength of Biological Materials*. Williams & Wilkins.

Yokoyama, T., Iino, Y., Kakizaki, K., & Murakami, Y. (1999). Human temporal bone study on the postnatal ossification process of auditory ossicles. *The Laryngoscope*, *109*(6), 927–930. https://doi.org/10.1097/00005537-199906000-00016

Zhang, X., & Gan, R. Z. (2010). Dynamic properties of human tympanic membrane – experimental measurement and modelling analysis. *International Journal of Experimental and Computational Biomechanics*, *1*(3), 252–270. https://doi.org/10.1504/IJECB.2010.03526

Zhang, X., & Gan, R. Z. (2011). Experimental measurement and modeling analysis on mechanical properties of incudostapedial joint. *Biomechanics and Modeling in Mechanobiology*, *10*(5), 713–726. https://doi.org/10.1007/s10237-010-0268-9

Zhang, X., & Gan, R. Z. (2013). Dynamic properties of human tympanic membrane based on frequency-temperature superposition. *Annals of Biomedical Engineering*, *41*(1), 205–214. https://doi.org/10.1007/s10439-012-0624-2

Zienkiewicz, O. C., Taylor, R. L., & Zhu, J. Z. (2013). Chapter 1—The Standard Discrete System and Origins of the Finite Element Method. In O. C. Zienkiewicz, R. L. Taylor, & J. Z. Zhu (Eds.), *The Finite Element Method: Its Basis and Fundamentals (Seventh Edition)* (pp. 1–20). Butterworth-Heinemann. https://doi.org/10.1016/B978-1-85617-633-0.00001-0

Zwislocki, J. (1957). Some impedance measurements on normal and pathological ears. *The Journal of the Acoustical Society of America*, *29*(12), 1312–1317. https://doi.org/10.1121/1.1908776